

1 **Mutation and cell state compatibility is required and targetable in Ph+ acute**

2 **lymphoblastic leukemia minimal residual disease**

3

4 Peter S. Winter^{1,2,3,4,5,*,#}, Michelle L. Ramseier^{1,2,3,4,6,*}, Andrew W. Navia^{1,2,3,4,6,*}, Sachit
5 Saksena^{7,8}, Haley Strouf¹, Nezha Senhaji⁵, Alan DenAdel^{9,10}, Mahnoor Mirza¹, Hyun Hwan An⁵,
6 Laura Bilal¹, Peter Dennis⁵, Catharine S. Leahy⁵, Kay Shigemori⁵, Jennyfer Galves-Reyes^{1,2,3,4,6},
7 Ye Zhang^{1,11}, Foster Powers⁵, Nolawit Mulugeta^{1,2,3,4,6}, Alejandro J. Gupta¹, Nicholas Calistri¹,
8 Alex Van Scoky⁵, Kristen Jones⁵, Huiyun Liu⁵, Kristen E. Stevenson¹², Siyang Ren¹², Marlise R.
9 Luskin^{5,13}, Charles P. Couturier^{1,2,3,4,6}, Ava P. Amini¹⁴, Srivatsan Raghavan^{4,5,13}, Robert J.
10 Kimmerling¹, Mark M. Stevens¹, Lorin Crawford^{9,10,14}, David M. Weinstock^{5,13,15}, Scott R.
11 Manalis^{1,4,11±}, Alex K. Shalek^{1,2,3,4,6,±#}, and Mark A. Murakami^{5,13,±#}

12

13 ¹Koch Institute for Integrative Cancer Research, MIT, Cambridge, MA, USA

14 ²Institute for Medical Engineering & Science, MIT, Cambridge, MA, USA

15 ³Department of Chemistry, MIT, Cambridge, MA, USA

16 ⁴Broad Institute of MIT and Harvard, Cambridge, MA, USA

17 ⁵Department of Medical Oncology, Dana-Farber Cancer Institute, Boston, MA, USA

18 ⁶Ragon Institute of MGH, MIT and Harvard, Cambridge, MA, USA

19 ⁷Computer Science and Artificial Intelligence Laboratory, MIT, Cambridge, MA, USA

20 ⁸Computational and Systems Biology Program, MIT, Cambridge, MA, USA

21 ⁹Center for Computational Molecular Biology, Brown University, Providence, RI, USA

22 ¹⁰Department of Biostatistics, Brown University, Providence, RI, USA

23 ¹¹Department of Biological Engineering, MIT, Cambridge, MA, USA

24 ¹²Department of Data Sciences, Dana-Farber Cancer Institute, Boston, MA USA

25 ¹³Harvard Medical School, Boston, MA, USA

26 ¹⁴Microsoft Research, Cambridge, MA, USA

27 ¹⁵Current Address: Merck and Co., Rahway, NJ, USA

28 *Co-first authors

29 ±Co-senior Authors

30 #To whom correspondence should be addressed:

31 Peter S. Winter Ph.D., pwinter@broadinstitute.org

32 Alex K. Shalek, Ph.D., shalek@mit.edu

33 Mark A. Murakami, M.D., mark_murakami@dfci.harvard.edu

34 **SUMMARY**

35 Efforts to cure BCR::ABL1 B cell acute lymphoblastic leukemia (Ph+ ALL) solely through
36 inhibition of ABL1 kinase activity have thus far been insufficient despite the availability of tyrosine
37 kinase inhibitors (TKIs) with broad activity against resistance mutants. The mechanisms that
38 drive persistence within minimal residual disease (MRD) remain poorly understood and therefore
39 untargeted. Utilizing 13 patient-derived xenograft (PDX) models and clinical trial specimens of
40 Ph+ ALL, we examined how genetic and transcriptional features co-evolve to drive progression
41 during prolonged TKI response. Our work reveals a landscape of cooperative mutational and
42 transcriptional escape mechanisms that differ from those causing resistance to first generation
43 TKIs. By analyzing MRD during remission, we show that the same resistance mutation can either
44 increase or decrease cellular fitness depending on transcriptional state. We further demonstrate
45 that directly targeting transcriptional state-associated vulnerabilities at MRD can overcome
46 BCR::ABL1 independence, suggesting a new paradigm for rationally eradicating MRD prior to
47 relapse. Finally, we illustrate how cell mass measurements of leukemia cells can be used to
48 rapidly monitor dominant transcriptional features of Ph+ ALL to help rationally guide therapeutic
49 selection from low-input samples.

50

51 **KEYWORDS:**

52 Cell State, Mutations, Ph+ B cell acute lymphoblastic leukemia, Minimal Residual Disease,
53 Biophysical Measurements

54

55 **HIGHLIGHTS:**

- 56 • Relapse after remission on TKI can harbor mutations in ABL1, RAS, or neither
- 57 • Mutations and development-like cell state dictate fitness in residual disease
- 58 • Co-targeting cell state and ABL1 markedly reduces MRD
- 59 • Biophysical measurements provide an integrative, rapid measurement of cell state

60 INTRODUCTION

61 A large fraction of patients with cancer achieve complete remission at some point during their
62 course of therapy, either through surgery, chemotherapy, radiation, or a combination thereof.
63 Nevertheless, many of these patients relapse or progress owing to a small pool of remaining
64 cancer cells commonly referred to as minimal residual disease (MRD). This is even true for
65 cancers with clear, targetable oncogene dependencies such as BCR::ABL1-rearranged B cell
66 acute lymphoblastic leukemia (Ph+ ALL). Despite highly effective tyrosine kinase inhibitors (TKI)
67 with potent activity against multiple resistance-conferring point mutations in BCR::ABL1, relapse
68 during single-agent treatment is nearly universal.^{1,2,3} Unfortunately, accumulating evidence casts
69 doubt on the potential for up-front combinations of next-generation TKIs to fully overcome
70 subclonal heterogeneity and thereby eradicate MRD.⁴

71 While most patients with BCR::ABL1-driven disease relapse with kinase domain
72 mutations, 30-40% of patients progress with BCR::ABL1-independent mechanisms that are
73 poorly understood.⁵ Previous studies have identified developmental heterogeneity across ALL,^{6,7}
74 as well as in Ph+ ALL specifically.^{8,9} This developmental heterogeneity has also been linked to
75 treatment response for multiple classes of inhibitors.^{6,7,10} Recent work specifically in Ph+ ALL
76 examined developmental subtypes that align with earlier (Early-Pro) and later developmental
77 (Late-Pro) B cell features, finding that the former was associated with poor overall survival upon
78 treatment with the first-generation TKI imatinib.⁸ Commitment to earlier or later stages of
79 development has been associated with cooperating alterations in lineage-defining transcription
80 factors (*EBF1* deletion or deletions in *IKZF1*, *PAX5*, and *CDKN2A*, respectively), suggesting that
81 developmental state adherence – and its associated therapeutic response – may be mutationally
82 driven and static upon leukemic transformation.^{8,9} However, other studies have nominated the
83 potential for a leukemia’s dominant developmental states to shift in response to therapeutic
84 pressure. Illustratively, non-mutational mechanisms of chemotherapy resistance have been
85 observed in ALL patient-derived xenografts (PDXs), whereby leukemia cells transiently adopt a
86 dormant, stem-like state at MRD;¹¹ others have demonstrated post-treatment shifts in the
87 abundance of dormant subpopulations mimicking earlier developmental stages.⁷ It has also been
88 suggested that TKI-resistant Ph+ ALL cells in a later developmental state proliferate by activating
89 signaling that typically occurs downstream of the pre-B cell receptor (pre-BCR), despite the
90 absence of a functionally expressed pre-BCR in Ph+ ALL.^{10,12} It remains unclear which attributes
91 allow for persistence during remission and if mutational or developmental phenotypes are the
92 dominant drivers of resistance.

93 Accordingly, resistance to ABL1 TKIs is multifactorial and extends beyond ABL1
94 resistance mutations, suggesting that informed strategies to convert deep remissions into cures
95 may require incorporating orthogonal measurements of the non-genetic determinants of cellular
96 state (e.g. via single-cell transcriptomics).^{13,14,15} However, there are limited studies describing
97 how mutations participate (or clash) with these additional cellular features to drive persistence
98 and clonal expansion under TKI pressure. Though recent evidence from our group and others
99 indicates that some mutations are enriched in specific transcriptional backgrounds,^{10,16,17,18,19} the
100 relative importance of mutational and transcriptional drivers to MRD persistence and relapse is
101 not known. Furthermore, there are significant technical challenges associated with isolating and
102 profiling rare residual cells that have limited their characterization largely to mutational profiling
103 – a problem affecting essentially all cancer types.^{13,20,21} While MRD enumeration and mutational
104 monitoring have been used to some clinical benefit,^{22,23,24} the translational utility of understanding
105 non-mutational attributes from these rare cells has yet to be demonstrated.²¹ These constraints,
106 coupled with the heterogeneity among MRD phenotypes both within and between patients, have
107 historically made it difficult to nominate specific therapeutic strategies to combat MRD. We and
108 others previously proposed that direct interrogation of MRD cells to identify dependencies for
109 individual patients could offer clinical benefit if approaches existed to define those dependences
110 in “real-time”.^{21,25} This would require a rapid strategy applicable to individual cells that could
111 distinguish patients most likely to respond to one of several available therapeutic options.

112 Here, to better understand how both mutational and transcriptional variation coordinate
113 to drive relapse within MRD, we defined the biology of Ph+ ALL cells at different stages of
114 treatment and across a diversity of models and human patients. We reveal unique and targetable
115 characteristics of Ph+ ALL MRD and nominate combination strategies to eradicate residual
116 disease.

117

118 RESULTS

119 Modeling disease kinetics in response to combination TKI in Ph+ ALL PDX models

120 Although treatment with allosteric BCR::ABL1 inhibitors drives deep remissions in patients,
121 nearly all will relapse if not consolidated with allogeneic stem cell transplantation. The recent
122 development of asciminib (ABL001), an allosteric inhibitor of BCR::ABL1,²⁶ created the first
123 opportunity to address whether dual inhibition of BCR::ABL1 could eradicate Ph+ leukemias
124 (**Figure 1A**). We combined orthosteric (ponatinib; 40 mg/kg/day) and allosteric (asciminib; 30
125 mg/kg/day) inhibitors in a diverse cohort of Ph+ ALL PDX models (n=13 models;²⁷ 190 mice
126 total) to assess how pre-existing clinical and molecular features would dictate response to

127 sustained oncogene withdrawal within a statistically powered, phase II-like preclinical trial
128 (**Figures 1A & 1B**; see **Methods** and **Tables S1 & S2**). All mice receiving ponatinib or
129 combination therapy, and 92% of subjects receiving asciminib monotherapy who survived
130 beyond one week achieved complete remission (CR), corroborating the dependence of these
131 leukemias on BCR::ABL1 (**Figures S1A & S1B**). The durations of remission with ponatinib-
132 based regimens exceeded those of asciminib monotherapy, but we observed no difference
133 between the combination and ponatinib monotherapy arms ($p=0.70$; **Figures 1C & S1C**).
134 Notably, survival outcomes between mice on each treatment arm did not correlate with PDX line
135 characteristics associated with inferior treatment response in other contexts, such as increased
136 prior lines of therapy,²⁸ *IKZF1* deletion,²⁹ and pre-existing *ABL1* resistance mutations (**Figure**
137 **S1D**).^{2,30} All mice were ultimately euthanized, either for disease progression or clinical toxicity.
138 Even the 7 mice euthanized for clinical toxicity after achieving a durable response – three of
139 whom maintained CR for >12 months on study (**Figure S1B**) – harbored residual ALL in the
140 bone marrow and/or spleen when sacrificed. These data demonstrate that while single-agent
141 ponatinib and combination therapy confer deep and prolonged clinical remissions, BCR::ABL1
142 inhibition alone was insufficient to fully eradicate human leukemias *in vivo*.

143

144 **Divergent mutational patterns upon oncogene inhibition in Ph+ B-ALL**

145 To chart landscapes of genetic resistance to single agent and combination TKI in Ph+ ALL, we
146 sequenced 142 PDX samples (74 trial and 68 other TKI-treated leukemias) and examined
147 patterns of acquisition within known driver mutations in ALL across multiple phases of treatment
148 (**Figure S2A**; **Table S3**; see **Methods**). In general, alterations in *ABL1* or RAS pathway genes
149 consistently emerged upon therapeutic pressure compared to mutations affecting B cell survival,
150 lineage commitment, or cell cycle control (**Figures S2A & S2B**). Of relapsed leukemias, 35%
151 harbored mutations in BCR::ABL1, frequently compound mutations involving T315I plus at least
152 one other high-level resistance mutation (e.g., Y253H, F311L, F359V) or an activating mutation
153 in *STAT5A* (collectively termed ‘ABL pathway’ mutations). A separate 24% relapsed with
154 activating mutations in RAS pathway genes – specifically *KRAS*, *NRAS*, *BRAF*, and/or *PTPN11*
155 – representing emergent alternate pathway utilization in these oncogene-addicted leukemias
156 (**Figures 1D & S2C**). Acquisition of driver pathway mutations was influenced by treatment arm
157 – mice treated with asciminib predominantly acquired ABL pathway mutations at relapse, mice
158 treated with ponatinib predominantly acquired RAS pathway mutations, and mice on the dual-
159 treatment arm acquired mutations on either ABL or RAS pathways (**Figure S2B**). Samples
160 harboring RAS pathway mutations were mutually exclusive with those involving ABL pathway

161 mutations within each PDX line at both pretreatment and progression time points (**Figure 1E**).
162 The remaining tumors (41%) harbored no driver mutations in either ABL or RAS pathway genes,
163 and the majority of these (74%) had no apparent genetic lesions explaining phenotypic
164 resistance by whole exome sequencing (**Figures 1D, S2A, & S2C**). These data suggest three
165 recurrent patterns for resistance whereby leukemias progress on therapy with either ABL
166 pathway, RAS pathway, or no discernible gain-of-function mutations.
167

168 **Ph+ ALL leukemic cells are defined by hybrid developmental states**

169 Given the lack of discernible mutation-driven resistance in a substantial fraction of our cohort
170 (**Figures 1D & S2A**), we hypothesized that resistance to single-agent or combination TKI in Ph+
171 ALL may be understood best by characterizing both mutational and transcriptional state
172 heterogeneity. To this end, we applied single-cell RNA-sequencing (scRNA-seq) to define
173 transcriptional states in Ph+ ALL and identify leukemic phenotypes associated with progression.
174 Using Seq-Well S^{3,31} we generated a dataset of 42,667 single-cell transcriptomes from 52
175 samples spanning 11 PDX lines from our phase II-like pre-clinical trial and 5 patients on a clinical
176 trial testing dasatinib (a second-generation orthosteric BCR::ABL1 inhibitor) plus asciminib for
177 previously untreated Ph+ ALL (**Figure 2A**; NCT02081378; see **Methods**). We then performed
178 consensus non-negative matrix factorization (cNMF) over each leukemia in this dataset to
179 identify intratumoral gene expression programs (GEPs; **Methods**). Hierarchical clustering of the
180 126 GEPs defined across individual leukemias revealed 7 shared patterns (meta-GEPs, or
181 “mGEPs”) of covarying gene programming that were present in at least 8 samples (**Figures 2B,**
182 **2C & S3A; Table S4**). Two mGEPs were defined by genes associated with active stages of the
183 cell cycle (e.g., *CENPF*, *MKI67*, *MCM6*, *E2F2*) and another mGEP specifically associated with
184 MYC activity (e.g., *HSP90AB1*, *NME1*). The remaining four mGEPs associated with various
185 stages of B cell development, either containing Pro-B cell genes (e.g., *DNTT*, *CSGALNACT1*),
186 genes associated with later stages of B cell development — i.e., Pre-BII (e.g., *CD38*, *IRF4*), and
187 Immature B (e.g., *CD79A*, *HLA-DPB1*) — or progenitor-associated genes co-expressed with
188 Immature B genes (e.g., *CD44*, *CSF1R* and *HLA-DQA1*, *IRF8*). These data suggest that aspects
189 of normal B cell development are captured as major axes of intratumoral transcriptional variation
190 in Ph+ ALL.

191 In several cases, genes defining multiple B lineage developmental stages were enriched
192 in the same GEP and co-expressed within individual leukemia cells (**Figures S3A & S3B**).^{7,32}
193 We next sought to better understand these stage-specific “hybrid” expression patterns by
194 utilizing a supervised machine learning approach to resolve the relationship between leukemia

195 cells and nonmalignant B cell development. To enable this comparison, we first generated a
196 reference dataset of human hematopoiesis from the bone marrow aspirates of healthy donors
197 (n=7), profiling both sorted and unsorted fractions to ensure the proper B cell developmental
198 populations were captured (**Figures S4A & S4B**; see **Methods**). By performing iterative
199 clustering, we identified 13 cell types spanning the HSC progenitor, myeloid, erythroid, and
200 lymphoid lineages (n = 13,643 cells; **Figures S4C & S4D**); each cell type population contained
201 cells from at least 6 of 7 donors (**Figures S4E & S4F**). To enable leukemic cell reference
202 mapping and comparison, we trained a random-forest (RF) classifier on the cell type-labeled
203 reference scRNA-seq dataset using 10-fold cross-validation (**Figures 2D & S5A**; see **Methods**).
204 We ensured this model was cueing on biologically-relevant expression patterns by using
205 permutation tests to identify the top 200 features needed to accurately classify single-cell
206 transcriptomes, as well as testing its accuracy on an external scRNA-seq dataset (**Figures S5B**
207 & **S5C**).¹⁶ We then assigned individual B-ALL cells to their most likely developmental state using
208 our RF classifier (**Figure 2D**). Across all malignant cells, the RF model assigned highest
209 classification probabilities for the Pro-B cell type, followed by Pre-BI, Pre-BII, HSC, and
210 Immature B cell types (**Figures 2E & 2F**); 1% of leukemia cells that classified into non-B lineage
211 cell types, such as T cells, were poor quality and removed from downstream analyses (**Figure**
212 **S5D**).

213 Corroborating our observations with NMF, marker genes that were restricted to individual
214 stages of B cell development in healthy cells were routinely co-expressed in leukemia cells
215 (**Figure 2G**). For example, within leukemic cells classified as Pro-B, we observed a dominant
216 secondary RF classification probability for an earlier (HSC) or later (Pre-BI, Pre-BII, Immature
217 B) stage of B cell development. We therefore characterized the transcriptional heterogeneity in
218 Ph+ ALL as a continuum of hybrid states according to their non-Pro-B RF classification
219 probability (**Figure 2H**). This revealed transcriptionally hybrid populations with underlying ProB-
220 like gene-expression, co-expressed with either progenitor-like genes (HSC-hyb) or genes
221 implicated in later developmental phenotypes (PreB-hyb or ImmatureB-hyb) (**Figures S6A-C**).
222 Genes correlated with these prediction probabilities reflected markers of earlier and later stages
223 of B cell development (**Figures S5E & S6A**; **Table S5**), and largely agreed with our unbiased
224 NMF results (**Figures S3A & S3C**). All three hybrid populations were characterized by predicted
225 utilization of canonical transcription factors (TFs) active in the healthy reference cell subsets
226 (e.g., CREB1, MYC in HSC-hyb; E2F2, FOXM1 in PreB-hyb; IRF4, FOXO3, CIITA in ImmatureB-
227 hyb), as well as aberrant TF activity (e.g., IRF1, STAT1 in ImmatureB-hyb; **Figure S6D**; see
228 **Methods**). Thus, anomalous co-expression of stage-associated genes in both primary patient

229 samples and PDX models defines a hybrid development-like continuum in Ph+ ALL and
230 implicates promiscuous, but still coherent, developmental transcriptional states.
231

232 **Hybrid development states are associated with treatment response and restricted**
233 **mutation acquisition**

234 We next asked whether shifts in this hybrid development-like continuum associated with
235 resistance to combination TKI. Overall, progression samples were characterized by decreased
236 hybrid population diversity, suggesting a restriction toward a single hybrid state (**Figure 3A**).
237 Differential expression analysis across all PDX tumors revealed genes included in the ProB-like
238 (e.g., *SOCS2*, *DNTT*) and HSC-hyb (e.g., *CD34*, *ID2*, *CD99*) signatures enriched at pre-
239 treatment while genes implicated in the more mature PreB-hyb (e.g., *TCL1A*, *VPREB3*, *IGLL1*)
240 and ImmatureB-hyb (e.g., *MS4A1*, *CD74*, *HLA-DRB1*) signatures were up-regulated at
241 progression, implicating a shift into later developmental stages (**Figure 3B**). However, not all
242 PDX models shifted toward more mature hybrid transcriptional states at progression. DFAB-
243 25157, which progressed with mutations in *ABL1* (**Figure S2C**; **Table S3**), remained dominated
244 by ProB-like and HSC-hyb states at both pretreatment and progression compared to other PDX
245 lines (**Figures 3C & S7A**). Leukemias that progressed with RAS pathway mutations either
246 contained a majority of cells expressing PreB-hyb and ImmatureB-hyb signatures at both pre-
247 treatment and progression (CBAB-30198, DFAB-54880), or increased proportions of malignant
248 cells with high PreB- and ImmatureB-hyb gene expression at progression (DFAB-62208; **Figure**
249 **S2C**; **Table S3**). Notably, the two PDX lines that progressed with neither ABL nor RAS pathway
250 mutations (CBAB-75914, CBAB-12402; **Figure S2C**; **Table S3**) demonstrated the strongest
251 shifts toward more mature hybrid developmental bins.

252 This enrichment for more mature phenotypes at progression was a strong departure from
253 patterns seen in Ph+ ALL treated with chemotherapy¹¹ or imatinib,⁸ where progression on
254 therapy was driven by less mature or stem-like cells. We sought corroborating evidence for this
255 observation in our PDX trial samples using standard immunophenotyping approaches (**Figure**
256 **S7B**; see **Methods**). Mirroring the transcriptional data, most pre-treatment leukemias harbored
257 multiple subpopulations across the B cell developmental trajectory and showed a similar
258 restriction in developmental state diversity at progression (**Figures 3D & S7C**). These
259 immunophenotyping data also corroborated the overall enrichment of more developmentally
260 mature phenotypes at progression (**Figure S7C**), specifically the predominance of more mature
261 CD34-negative developmental phenotypes in leukemias that progressed with RAS pathway

262 mutations or no mutations ($p<0.001$ from Dirichlet regression for both mutation group
263 comparisons to ABL pathway-mutated leukemias; **Figures 3E, 3F & S7D**).

264 We next sought direct clinical evidence for the relevance of developmentally-hybrid
265 programs in resistance to combination TKI. We prospectively collected serial single-cell
266 measurements from the bone marrow of 2 patients (n=5 individual samples, n=7,649 cells;
267 **Figure 3G; Table S6**) enrolled on a phase 1 trial testing dasatinib in combination with asciminib
268 and prednisone. Clinical activity was assessed by the reduction in bone marrow *BCR::ABL1*
269 mRNA transcript levels after three cycles of treatment (day 85; NCT02081378). Samples from
270 patient BIAB-16768 maintained a predominant population of ProB-like malignant cells over the
271 course of treatment and entered remission before 85 days of treatment (3-log reduction in bone
272 marrow *BCR::ABL1* detected by qRT-PCR). By contrast, samples from patient DFAB-71417
273 rapidly shifted toward later developmental hybrid states (PreB-hyb and ImmatureB-hyb) by day
274 28 on therapy and failed to respond by day 85 (1-log reduction in bone marrow *BCR::ABL1*
275 detected by qRT-PCR; **Figures 3G & 3H**). Combined with our PDX analysis, these results
276 provide preliminary evidence that more mature developmentally-hybrid expression programs
277 can drive resistance to dual ABL1 inhibition.

278

279 **Longitudinal monitoring of cell state and mutational co-evolution**

280 Collectively, our data nominate 3 potential routes of resistance to ABL1 inhibition in Ph+ ALL: 1)
281 mutational reactivation of ABL signaling in progenitor-like states, 2) mutational activation of RAS
282 signaling in later-stage hybrid states, or 3) transcriptional shifts toward later developmental
283 hybrid states without accompanying mutational alterations. To directly explore whether these
284 routes are recoverable at multiple timepoints during ABL1 inhibition, we next examined
285 genotype-phenotype co-evolution by profiling single cells from pre-treatment, MRD (21 days on
286 therapy), and progression in our PDX models, selecting individual leukemias that represent each
287 putative mechanism of resistance (**Figure 4A**; DFAB-25157, ABL1 reactivation; DFAB-62208,
288 RAS activation; CBAB-12402, no mutations). At each stage of therapy, we profiled leukemia
289 cells using SMART-Seq2 (SS2)-based scRNA-seq to increase information capture from low cell
290 numbers at remission and to facilitate matched single nucleotide variant (SNV) detection in the
291 same single cells. For these longitudinal studies, we treated mice with single agent ponatinib
292 (see **Methods**) since it performed equivalently to combination TKI therapy (**Figure 1C**) and is
293 directly relevant to treatment being used in patients.

294 First, we ensured the robustness of our RF hematopoietic developmental classifier on
295 full-length, SS2 transcriptomes from both healthy (n = 421; same donors as **Figure S4**) and

296 leukemic cells (n = 3,641; **Figure S8A**; see **Methods**). Using our RF framework, we
297 independently derived the leukemic cellular states in our SS2 dataset (**Figures S8B-D; Table**
298 **S7**), finding they highly correlated with our Seq-Well-derived hybrid phenotypes – specifically in
299 early progenitor (Progenitor-like vs. HSC-hyb) and more mature (PreB-like vs. PreB-hyb and
300 ImmatureB-hyb) leukemic cell states (**Figure S8E**). Given this coherence, hereafter we refer to
301 Progenitor-like and PreB-like SS2 programs as HSC-hyb and PreB-hyb respectively for
302 simplicity. We next detected mutated transcripts identified from bulk DNA sequencing within
303 individual cells from our SS2 data (**Figure S9A; Table S3**; see **Methods**). The number of
304 detected mutant transcripts in SS2 libraries was limited by the average expression of the
305 corresponding gene, with higher rates of detection for RAS pathway single-nucleotide variants
306 (SNVs; *GNB1*, *NRAS*, *KRAS*, *PTPN11*) compared to ABL pathway SNVs (*ABL1*, *STAT5A*)
307 (**Figure S9B**). For highly expressed target genes, however, the proportion of single cells
308 harboring mutations corresponded with the variant allele frequency measured in bulk
309 sequencing of the same tumor (**Figure S9C; Table S3**), highlighting that SS2 provides sufficient
310 SNV detection to capture the kinetics of RAS pathway mutations in our dataset. Furthermore,
311 single-cell profiling enabled highly sensitive detection of rare malignant cells harboring mutations
312 with less than 3% VAF from bulk sequencing, allowing comparisons of dominant and rare
313 subclones (**Figure S9C**). Finally, we identified copy number variations (CNVs) in the SS2 profiles
314 using inferCNV (see **Methods**). In combination with transcriptional state information, these data
315 provided a detailed, high-resolution picture of the co-evolution of mutational and transcriptional
316 heterogeneity in B-ALL single cells over the course of ponatinib treatment (**Figures 4B & S9D-F**).
317

318

319 **Cell state dictates fitness and restricts growth of RAS-mutant cells in remission**

320 Using this high-resolution dataset, we first evaluated changes in hybrid developmental state
321 frequency between pre-treatment and residual cells in each model during treatment with
322 ponatinib (**Figure 4C**). CBAB-12402 was transcriptionally dynamic and demonstrated a
323 significant shift towards a dominant PreB-hyb phenotype among MRD cells that was conserved
324 at progression, mirroring patterns seen in the larger PDX trial for this model (**Figures 3C & S9F**).
325 Transcriptional states in MRD and progression leukemia cells from DFAB-62208 displayed a
326 minor shift forward to stronger PreB-hyb expression compared to pre-treatment. DFAB-25157
327 was variable along the progenitor to mature phenotype continuum at both pretreatment and
328 progression, driven by dominant HSC-hyb gene expression. A subset of cells from this model

329 co-expressed HSC-hyb and PreB-hyb states in MRD, albeit at much lower levels than PreB-hyb
330 scores in the other two models (**Figures S9E-G**).

331 Point mutations in *NRAS* and *KRAS* from the same leukemia cells revealed surprising
332 dynamics across PDX models and stages of therapy (**Figure 4D**). We detected very low
333 frequency RAS mutations in CBAB-12402 at pre-treatment that were not enriched at
334 progression, in agreement with bulk DNA sequencing data that did not identify actionable driver
335 mutations (**Figure S2C; Table S3**), thus implicating a “state-shift” only mechanism enabling
336 progression. DFAB-62208 also harbored low-frequency *KRAS* and *NRAS* point mutations at
337 pretreatment; a single *NRAS*-mutant, cycling cell was observed in remission and both *KRAS*-
338 and *NRAS*-mutant clones expanded at progression (mirroring bulk sequencing data; **Figure**
339 **S2C; Table S3**), suggesting the preexisting PreB-hyb transcriptional state was permissive for
340 expansion of RAS-mutant clones. In DFAB-25157, we observed a significant increase in the
341 proportion of *KRAS* mutant malignant cells in MRD (3 of 6 mice at MRD harbored identifiable
342 RAS-mutant cells) compared to pretreatment leukemic cells, a finding we confirmed using bulk
343 DNA sequencing from a separate sample (**Table S3**; Mouse 4H0, *KRAS* AF 0.75). This was
344 surprising given that this model does not progress on therapy with emergent RAS mutations
345 (**Figures 4D & S2C**). Indeed, considering both single-cell CNV and SNV clones (**Figures S9D**
346 & **S9E**), we found no evidence of outright genetically-driven clonal selection in DFAB-25157
347 despite the enrichment of RAS-mutant cells in remission (**Figure 4E**). In this case, our data
348 suggest that RAS-family mutations in cells with a discordant developmental cell state permit
349 survival (or persistence) in the context of ABL inhibition but confer a fitness disadvantage that
350 suppresses their expansion.¹⁰

351 We next interrogated the single-cell transcriptomes of remission DFAB-25157 cells to
352 define mechanisms for this apparent state-genotype incompatibility. *KRAS*-mutant leukemic
353 cells from DFAB-25157 at MRD upregulated genes that positively regulate senescence (e.g.,
354 *CCL2*, *TOB1*) and negatively regulate cell cycle (e.g., *CDKN2A*) compared to *KRAS*-mutant
355 leukemia cells from all other time points and PDX lines (**Figure 4F**). To evaluate how this
356 signature evolves over the course of therapy, we scored individual cells for these upregulated
357 senescence-associated genes (Senescence-like score; **Table S8**). *KRAS*-mutant clones with
358 similar senescence-like signatures were present at pretreatment in cells with co-incident HSC-
359 hyb phenotypes, whereas PreB-hyb *KRAS*-mutant leukemia cells across other treatment stages
360 and PDX lines had low senescence-like scores (**Figure S9G**). These data suggest the fitness of
361 RAS mutant clones is influenced by the compatibility of transcriptional state and genotype: the
362 expression of senescence-implicated genes is restricted to HSC-hyb cells harboring RAS

363 mutations, whereas RAS-mutant PreB-hyb cells remain capable of entering the cell cycle
364 (**Figure 4G**). Therefore, despite activation of a mitogenic oncogene that contributes to resistance
365 to TKI in multiple contexts, developmental states restrict the expansion of these genotypes,
366 including during deep remissions.

367 As MRD genotypes alone could not predict clonal expansion driving progression, we
368 sought to identify what phenotypes persist in MRD and actively contribute to progression. We
369 binned each cell from MRD and progression into four fitness phenotypes based on their
370 expression of senescence-like and cell cycle scores (**Figure 4H**). To our surprise, progression
371 contained a significant accumulation of putatively cell cycle-arrested cells with higher
372 senescence-like scores compared to MRD ($p<0.001$, KS statistic). Notably, we also observed
373 CNV subclonal fitness plasticity in DFAB-25157, whose cells at MRD were characterized by high
374 senescence-like scores. A cycling population of RAS-wildtype cells from one subclone emerged
375 at progression (**Figures 4I & S9H**; $p<0.01$, Fisher's exact test), associated with an increased
376 abundance of that subclone at progression (**Figure 4E**). In contrast, RAS-mutant cells from
377 DFAB-62208, characterized by later developmental phenotypes, were highly proliferative at
378 progression (**Figure S9H**). Collectively, these data suggest that diverse Ph+ ALL genetic
379 subclones can persist to progression and even clones with senescence-like phenotypes at MRD
380 may expand with enhanced fitness to seed progression. Given the possibility of plasticity and
381 the restrictions imposed by cell states on certain genotypes, these data suggest it may be difficult
382 to predict from genetics alone the subclones that will ultimately seed relapse.

383

384 **Direct targeting of transcriptional programs in residual disease deepens remission**

385 In light of this complexity, we hypothesized that directly targeting transcriptional programs that
386 enable persistence at MRD could overcome the diversity of subclones identified at remission.
387 Using differential expression and gene-gene correlation (see **Methods**), we identified three
388 expression programs in remission that persisted to progression – a Pre-BCR Signaling program,
389 closely aligned with the PreB-hyb state (e.g., *IGLL1*, *VPREB3*), a Stress/Autophagy program
390 (e.g., *HSPA1A*, *UBC*), and an inflammatory program (e.g., *EGR1*, *JUN*, *TNF*; **Figure 5A**; **Table**
391 **S9**). The inflammatory program was evenly expressed across all leukemic cells in remission, a
392 phenotype seen in other hematological diseases (28504724, 35618837; **Figure S10A**). The
393 remaining expression programs were variable across MRD cells stratifying those high for the
394 Stress/Autophagy cell state and those expressing the Pre-BCR Signaling program (**Figures**
395 **S10A & S10B**). We considered these variable programs to test the hypothesis that targeting
396 specific expression programs could deepen remissions. These two variable gene expression

397 programs split along fitness subpopulations, with leukemic cells harboring high Pre-BCR
398 Signaling scores also scoring high for cell cycle, and leukemic cells with high Stress/Autophagy
399 program scores enriched for senescence-like expression (**Figure 5B**).

400 We next evaluated whether these two gene expression programs could be therapeutically
401 targeted. We paired ponatinib with either the FDA-approved SYK inhibitor, fostamatinib, to inhibit
402 pre-BCR signaling in leukemic cells scoring highly for the Pre-BCR program, or the FDA-
403 approved p38a MAPK inhibitor losmapimod, to target leukemic cells scoring highly for the
404 Stress/Autophagy program given the co-enrichment of p38a MAPK activation with the
405 Stress/Autophagy program and previous work supporting crosstalk between p38 signaling and
406 autophagy/leukemic stem cell-related phenotypes (**Figure S10C**).^{33,34,35} As a combination
407 control, we compared transcriptional-state-directed combination therapy to dual oncogene
408 targeting using ponatinib and asciminib (**Figure 5C**). We selected two PDX lines that were
409 enriched for either variable MRD expression program: DFAB-25157, which scored highly for the
410 Stress/Autophagy program, and DFAB-62208, which scored highly for the Pre-BCR signaling
411 program and sat along the poised/cell cycle spectrum (**Figures 5D, 5F & S10D**). DFAB-25157
412 mice treated with combination losmapimod plus ponatinib showed a significant reduction in
413 residual disease burden compared to dual oncogene suppression, a striking comparison as
414 DFAB-25157 tumors consistently progressed with acquired mutations in ABL1 (**Figures 5E &**
415 **S2C**). Analogously, DFAB-62208 mice responded to ponatinib plus fostamatinib and had
416 significantly reduced residual disease compared to dual oncogene suppression (**Figure 5G**).
417 These data suggest that residual leukemia cells can be effectively targeted according to the
418 specific transcriptional state governing persistence in remission.

419

420 **A biophysical workflow for low-cost, rapid coupling of genotype to developmental state**
421 **in leukemia cells**

422 Our data support the importance of both mutations and overall cell state in determining leukemic
423 cell fitness and therapeutic susceptibility at MRD. While mutations can be monitored in clinical
424 workflows from residual leukemic cells, single-cell transcriptomics is currently difficult to scale
425 due to the overall cost and time required for sample collection and analysis. We sought a metric
426 that would integrate complex transcriptional information from low-input MRD samples to enable
427 rapid determination of leukemic cell state, compatible with downstream mutational profiling.

428 Immunophenotyping strategies of developmental cell states, especially given the very low
429 cell numbers at MRD, is likely to be highly challenging. Alternatively, cell size characteristically
430 decreases as healthy progenitor cells progress from HSCs to pro-B to pre-B cells, putatively

431 providing a label-free attribute with which to phenotype ALL cells.³⁶ We have previously shown
432 that measurements of buoyant mass, as measured by the suspended microchannel resonator
433 (SMR),³⁷ can reveal changes in cell state.^{38,39,40,41,42} Buoyant mass (referred to hereafter simply
434 as mass) can be measured from live single cells with a resolution near 50 fg, which is highly
435 precise given that the average buoyant mass of a hematopoietic cell is ~75 pg.⁴³ Further, we
436 have shown that coupling mass measurements to scRNA-seq from the same cell enables the
437 determination of expression-dependent changes in cellular mass.⁴¹ Thus, we hypothesized that
438 underlying biophysical development-like phenotypes may be conserved and sufficient to rapidly
439 capture the developmental state of a leukemia cell.

440 We first determined whether mass can distinguish B cell developmental states in healthy
441 donors. By performing paired SMR-SS2⁴¹ on cells flow-sorted from healthy donors into
442 Progenitor (CFU-L; 155 cells), Pro-B (122 cells), and Immature B (105 cells) gates, we found
443 that each stage of B cell development was characterized by distinct mass distributions, with
444 decreasing cell mass along the B cell developmental trajectory (**Figures 6A, 6B, S11A & S11B**).
445 Within each B cell developmental stage, healthy cells with higher mass also scored highly for S
446 phase or G2/M phase cell cycle, a pattern seen across studies using SMRs within a specific cell
447 type (**Figure S11A**).^{41,43,44} We found a strong relationship between each gene's dependence on
448 RF prediction scores and matched cellular mass ($r = 0.88$ from Pearson correlation), indicating
449 that genes highly associated with cell mass are also most correlated to healthy B cell
450 developmental states (**Figure S11C**). Consistently, in leukemic cells, genes defining the HSC-
451 hyb signature were most positively correlated with leukemic cell mass, and genes defining the
452 PreB-hyb signature were most negatively correlated with cell mass ($r = 0.90$) (**Figure 6C**). We
453 validated this observation across 17 additional PDX samples at the bulk level showing that the
454 average leukemic cell mass reflects the average RF predicted state ($r = 0.66$) and tracks with
455 the progression-emergent mutations for each PDX (**Figure 6D**). Taken together, these data
456 support mass as a meaningful surrogate for development-associated transcriptional state in
457 leukemia cells.

458 Finally, we evaluated how single-cell mass could pair with genotyping to further define
459 developmental state and mutation compatibility (**Figure 6E**). We compared mass distributions
460 between RAS-mutant PDX lines with higher HSC-hyb and high senescence-like gene
461 expression (DFAB-25157) and PDX lines with higher PreB-hyb gene expression (DFAB-62208
462 and DFAB-54880). State-genotype discordant HSC-hyb DFAB-25157 cells were enriched for
463 senescent-like scores and significantly higher mass than the more developmentally-mature and
464 non-senescent DFAB-62208 and DFAB-54880, mirroring mass differences between healthy

465 progenitor and immature B cells (**Figure 6F**). Furthermore, we found a significant difference
466 between the mass distributions of DFAB-25157 MRD cells compared to DFAB-62208 cells at
467 MRD (**Figure 6G**), implicating that mass measurements reflect developmentally-relevant and
468 therapeutically actionable heterogeneity in MRD for these leukemias (**Figures 5D-G**).
469 Consequently, mass measurements appear to be sufficiently sensitive to distinguish differences
470 in developmental state for leukemic cells, and, when assessed simultaneously with genotypic
471 data from the same sample, may predict therapeutic susceptibility for targeting states in MRD.
472

473 DISCUSSION

474 Oncogene-directed therapy provides clear benefits to certain patient populations, yet it is equally
475 clear that targeting cancers solely based on their mutational heterogeneity has an upper
476 limit.^{45,46,47} Indeed, our phase II-like preclinical trial results reveal that even combinations of highly
477 potent TKIs aimed at the same oncogene do not cure Ph+ ALL. While much of the preclinical
478 and clinical data in CML and ALL have identified pathway reactivation through alterations in
479 ABL1 as a primary mechanism of escape,^{1,2,3,4} our data suggest alternative pathway activation
480 through RAS alterations also drives resistance in a significant fraction of cases. Mirroring
481 patterns seen in patients,⁵ our trial also shows that a large fraction of mice engrafted with patient-
482 derived leukemias (up to 40%) progress without a clear genetic driver, warranting the exploration
483 of alternate therapeutic strategies for these cases.

484 Transcriptional phenotypes have been described in AML,¹⁶ CML,¹³ and ALL,⁸ and recent
485 studies suggest that patients with more progenitor-like leukemia cells have a worse overall
486 prognosis and tend to respond poorly to therapy. In ALL specifically, a recent study showed that
487 leukemias enriched for progenitor-like states have worse outcomes on imatinib.⁸ Our data
488 suggest that lineage plasticity is relatively common in response to 3rd generation and
489 combination TKI therapy, with resistant leukemia cells most frequently mimicking later stages of
490 B cell development. This contrasts with most settings where, even in solid cancers, a canonical
491 response to therapy is the enrichment of less differentiated cell states.^{48,49} Moreover, we
492 demonstrate the importance of defining cell state and mutational associations – despite myriad
493 mutational routes that might be predicted to confer resistance, our data suggest that specific
494 transcriptional backgrounds may restrict leukemias to distinct subsets of escape mutations.
495 Though these associations will need to be learned in larger cohorts and for each specific
496 disease, this framework may represent a strategy for prioritizing the permissible transcriptional
497 state/mutational convergences within oligo/polyclonal populations that can drive progression.

498 While there is agreement on the clinical and therapeutic importance of understanding
499 MRD, the phenotypes of the residual cells responsible for seeding progression and how to best
500 target them remains an outstanding question in the field owing to several technical
501 challenges.^{21,25} In this regard, Ph+ ALL is a tractable system, as it is feasible to isolate MRD
502 from either blood or bone marrow of patients or xenografted mice in adequate numbers to allow
503 for single-cell transcriptomics in addition to DNA sequencing. We found that matched genotypic
504 and phenotypic profiling of rare MRD cells was critical for identifying three key insights about the
505 biology of MRD and the translational potential of targeting it prior to relapse. First, the
506 conventional wisdom proposes that not all cells at MRD can seed relapse, especially those that
507 have exited the cell cycle or are otherwise classified as “unfit”.^{21,25} In contrast, we find that some
508 CNV-defined clones expressing senescence-like genes at MRD can re-enter the cell cycle and
509 contribute to progression. Of note, a similar phenotype has also been observed in AML treated
510 with chemotherapy.⁵⁰ Second, our discovery that senescent clones harboring RAS mutations
511 were enriched in residual disease but did not contribute to relapse highlights the importance of
512 understanding the cell state of mutant cells. This observation complicates current MRD
513 evaluation strategies, as information about genotype alone will likely be insufficient to predict
514 relapse for specific leukemias. Third, we show that co-targeting tumor-specific transcriptional
515 programs in remission out-performs additional targeting of the same oncogene, at least with
516 current therapeutics. This finding provides a translational rationale for identifying transcriptional
517 phenotypes in residual disease to inform the rational selection of combination strategies. The
518 importance of targeting cell state likely extends to other cancers where a central oncogene can
519 be deeply inhibited, resulting in relapses that have acquired an alternate histology, including
520 small cell relapse after androgen receptor inhibition in prostate cancer,⁵¹ squamous cell and
521 small cell transitions after EGFR inhibition in lung adenocarcinoma,^{52,53} and estrogen receptor
522 positive relapse after HER2 blockade.⁵⁴

523 We note that the influence of an intact immune system on the developmental dynamics
524 of Ph+ ALL is not well defined and represents a liability of our approach interrogating PDX
525 models of leukemia in NSG hosts. We mitigated this by confirming our PDX results in serial
526 measurements from patient bone marrow, but future efforts should include the use of humanized
527 xenograft models and additional evaluation of primary patient specimens. Nevertheless, our
528 identification of a central role for developmental state in Ph+ ALL has had immediate clinical
529 implications. Our phase 1 clinical trial of dual oncogene targeting (NCT03595917) completed
530 accrual⁵⁵ and reopened as a phase 2 trial incorporating early introduction of the CD3xCD10
531 bispecific antibody blinatumomab (anti-CD3xCD19 bispecific antibody), which should maintain

532 activity across the developmental states we have defined in MRD and relapse. Importantly,
533 blinatumomab has demonstrated promising clinical activity in clearing residual disease in
534 patients intended for consolidative allogeneic hematopoietic stem cell transplantation.^{56,57}

535 Evaluating complex, non-mutational biomarkers may have significant clinical challenges.
536 scRNA-seq is not yet a clinically-scalable assay, nor is it readily interpretable on a short time-
537 scale. For translation to clinical workflows, it will be critical to develop diagnostics that are able
538 to assess a sample's genotype and relevant phenotype with reasonable throughput and
539 interpretability. For remission profiling specifically, this is further complicated by the requirement
540 for use with low-input samples. Owing to the low-input and non-destructive nature of the SS2-
541 SMR measurement,⁴¹ we were able to acquire a unique dataset that directly links cellular mass
542 to leukemic developmental state. These data establish that assessing complex, non-mutational
543 biomarkers may be possible using mass as a relatively simple integrative cellular property. Our
544 matched SMR/scRNA-seq data from normal bone marrow hints that mass variation may extend
545 to other hematopoietic lineages as well so this approach may be applicable in diseases with
546 significant developmental heterogeneity such as AML.¹⁶ We speculate that additional features
547 of clinical utility in different disease contexts could come from other integrative single-cell
548 properties such as morphology.⁵⁸

549 In sum, we find transcriptional state controls the fitness of individual clones in MRD and
550 dictates the landscape of progression on TKI in Ph+ ALL. We highlight the need to understand
551 and monitor both mutational and transcriptional features in clinical pipelines to properly evaluate
552 individual clones for their potential to drive relapse. We functionally establish the paramount
553 importance of cell state in this context and suggest it should be prioritized for targeting in
554 conjunction with driver oncogenes. In agreement with recent studies in solid cancers,^{59,60,61} our
555 work in leukemia makes it apparent that therapies intended to convert remissions to cures should
556 consider monitoring and targeting features outside of traditional mutational biomarkers.⁶²

557 **ACKNOWLEDGEMENTS**

558 This work was funded by the NIH-NCI U54 CA217377 (S.R.M., D.M.W., A.K.S.), K08 CA212252
559 (M.A.M.), K12 HL141953-05 (M.A.M.), P30 CA14051 (A.K.S., S.R.M.), 1U2C CA23319501
560 (A.K.S.), R35 CA231958 (D.M.W.); the Paul G. Allen Frontiers Group Distinguished Investigator
561 Award (S.R.M., D.M.W.); the Sloan Research Fellowship in Chemistry (A.K.S.); and the Pew-
562 Stewart Scholars Program for Cancer Research (A.K.S.). The authors acknowledge assistance
563 with targeted panel and whole exome sequencing of PDX specimens from Dr. Aaron Thorner,
564 Dr. Anwesha Nag, and Neil Patel of the Dana-Farber Cancer Institute Center for Cancer
565 Genomics.

566

567 **AUTHOR CONTRIBUTIONS**

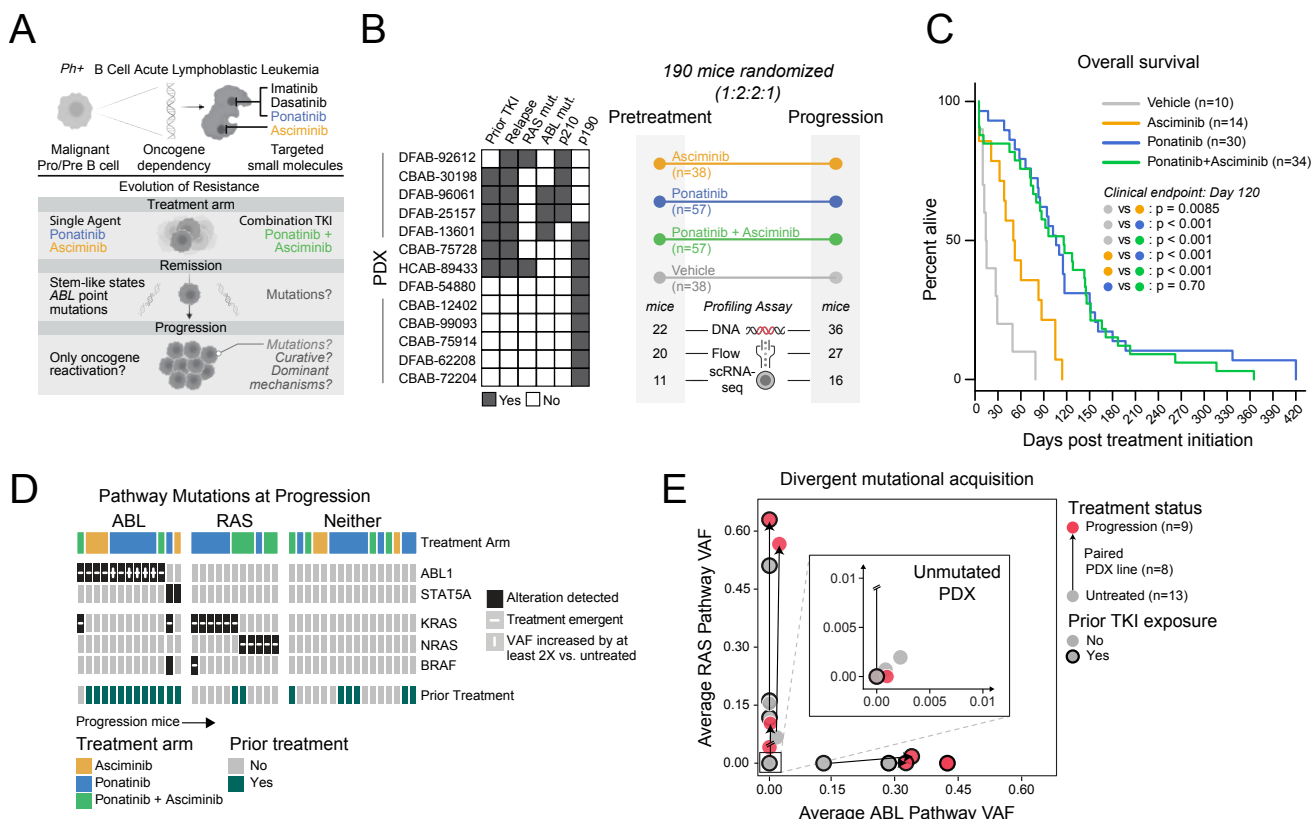
568 Conceptualization, P.S.W., S.R.M., D.M.W., A.K.S. and M.A.M.; Methodology, P.S.W., M.L.R.,
569 A.W.N., S.S., C.P.C., L.C., S.R.M., D.M.W., A.K.S., and M.A.M; Validation, P.S.W., M.L.R.,
570 A.W.N., and M.A.M.; Formal Analysis, P.S.W., M.L.R., K.E.S., S.R., A.D., S.S., and M.A.M.;
571 Investigation, P.S.W., M.L.R., A.W.N., A.D., S.S., H.S., N.S., M.M., H.H.A., L.B., P.D., C.S.L.,
572 K.S., J.G.R., Y.Z., F.P., N.M., L.C., A.P.A, S.V.R., A.J.G., N.C., A.V.S., K.J., H.L., R.J.K., M.M.S.,
573 M.A.M.; Resources, S.R.M., D.M.W., A.K.S., and M.A.M.; Data Curation, P.S.W., A.W.N and
574 M.A.M.; Writing – Original Draft, P.S.W., M.L.R., A.W.N, A.K.S., and M.A.M; Writing – Review &
575 Editing, P.S.W, M.L.R., A.W.N, L.C., A.P.A., S.S., S.V.R., M.R.L., S.R.M., D.M.W., A.K.S., and
576 M.A.M.; Visualization, P.S.W., M.L.R., A.W.N., A.K.S., and M.A.M.; Supervision, M.A.M.,
577 P.S.W., S.R.M., D.M.W., and A.K.S.; Project Administration, P.S.W., S.R.M., D.M.W., A.K.S.,
578 and M.A.M.; Funding Acquisition, S.R.M., D.M.W., A.K.S., and M.A.M.

579

580 **DECLARATION OF INTERESTS**

581 S.R.M., R.J.K., M.M.S., and D.M.W. disclose equity ownership in Traversa. A.K.S. reports
582 compensation for consulting and/or SAB membership from Honeycomb Biotechnologies,
583 Cellarity, Bio-Rad Laboratories, Fog Pharma, Passkey Therapeutics, Ochre Bio, Relation
584 Therapeutics, IntrECate biotherapeutics, and Dahlia Biosciences unrelated to this work. P.S.W
585 receives research funding from Microsoft. S.R. holds equity in Amgen and receives research
586 funding from Microsoft. D.M.W. is an employee of Merck and Co., owns equity in Merck and Co.,
587 Bantam, Ajax, and Traversa, received consulting fees from Astra Zeneca, Secura, Novartis, and
588 Roche/Genentech, and received research support from Daiichi Sankyo, Astra Zeneca,
589 Verastem, Abbvie, Novartis, Abcura, and Surface Oncology. P.S.W., A.K.S., M.A.M., S.R.M.,
590 and D.M.W. have filed a patent related to this work.
591 Other authors – none.

Figure 1



593 **Figure 1. Genetic mechanisms of resistance to oncogene inhibition in Ph+ ALL.**

594 **(A)** Motivation for evaluating efficacy and mechanisms of resistance to combination TKI therapy
595 in Ph+ ALL.

596 **(B)** Patient characteristics of the 13 PDX models used in the study and Phase II-like randomized
597 *in vivo* trial design. Number of mice examined by genetic profiling, immunophenotyping
598 (“Flow”), or scRNA-seq at pre-treatment and progression time points. For characteristics of
599 patients from whom PDX lines were derived (**Table S2**): “TKI”=prior patient exposure to
600 tyrosine kinase inhibitor; “relapse”=patient tumor at progression; “mut”=mutant (non-
601 BCR::ABL1); “p210” and “p190”=p210 and p190 BCR::ABL1 isoforms, respectively.

602 **(C)** Overall survival across treatment arms in Phase II-like study; p-values from Cox regression
603 analysis at clinical end-point (day 120) are indicated for each pairwise comparison between
604 treatment arms.

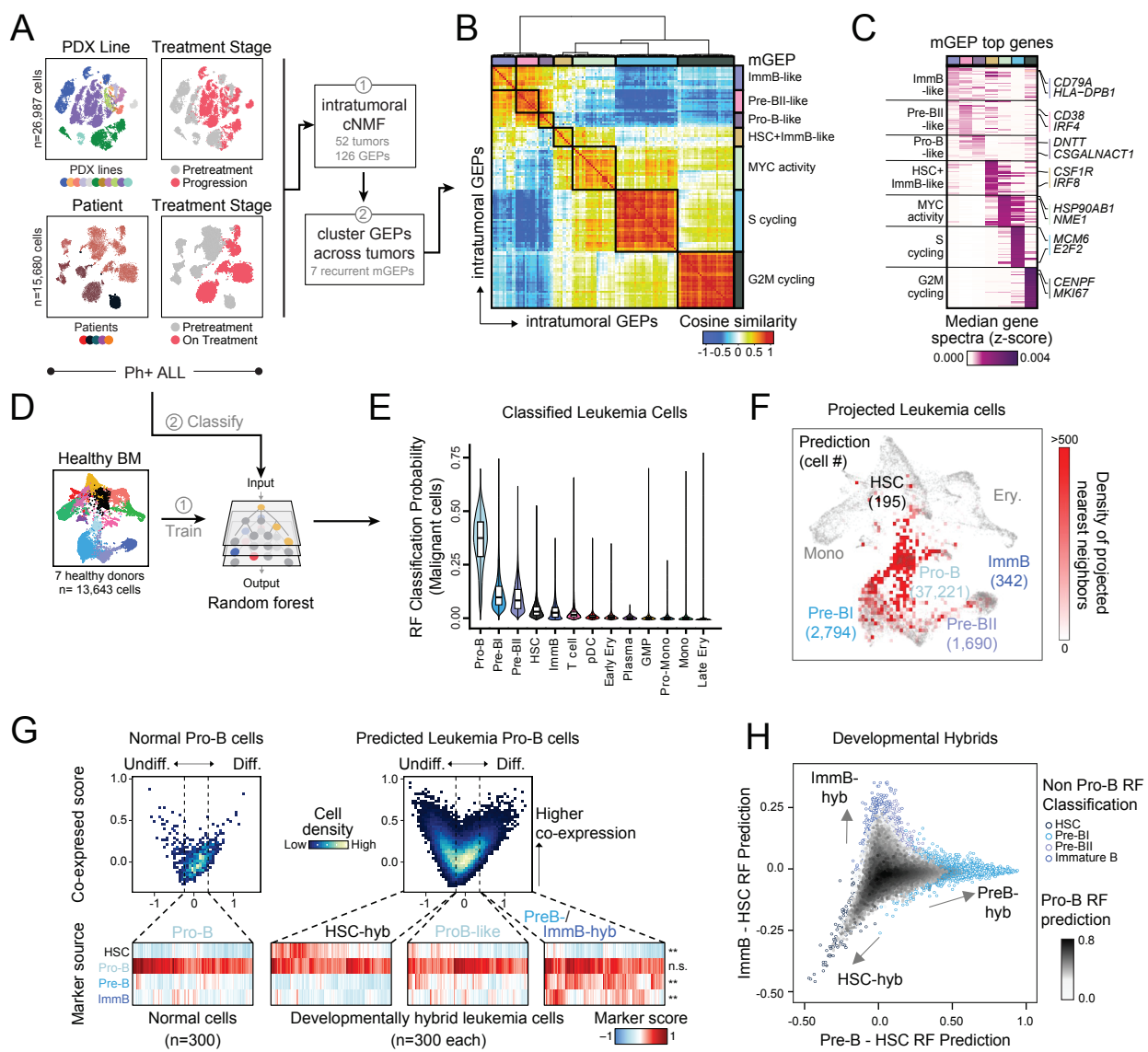
605 **(D)** ABL and RAS pathway detected alterations in Phase II-like study tumors at progression
606 (n=40). Treatment emergent mutations indicated when mice from the same PDX line were
607 profiled at pretreatment (see full alteration details in **Figure S2A** and **Table S3**). Prior
608 treatment indicates mice whose PDX lines were derived from patients with prior TKI and
609 chemotherapy exposure. “VAF”=variant allele frequency.

610 **(E)** Average VAF for mutations along RAS (y-axis) or ABL (x-axis) pathways, averaged across
611 mice in each PDX line at pretreatment or progression. Arrows link pretreatment and
612 progression average VAFs from the same PDX line. PDX lines derived from patients with
613 prior TKI exposure are outlined in black. Inset highlights a subset of PDX model timepoints
614 where no (n=4 pretreatment, n=1 progression) or few mutations were detected in either
615 pathway.

616

617 See also *Figures S1 & S2; Tables S1, S2 & S3*.

Figure 2



619 **Figure 2. Hybrid developmental transcriptional states define B-ALL.**

620 **(A)** Overview of Ph+ ALL scRNA-seq data collected from PDX lines (n=26,987 cells across 11
621 PDX lines inclusive of 38 pretreatment and progression tumors) and patient biopsies
622 (n=15,680 cells across 5 patients inclusive of 14 pretreatment and on-treatment tumors).

623 **(B)** Unbiased factorization of leukemic scRNA-seq data with consensus non-negative matrix
624 factorization (cNMF). Each row and column is an individual GEP and clustering is based on
625 cosine similarity to find meta-programs (mGEPs; see **Methods**). “HSC”=hematopoietic stem
626 cell; “ImmB”=Immature B.

627 **(C)** Each mGEP annotated by the top 30 genes with the highest median cNMF gene spectra
628 score across clustered intratumoral GEPs (**Table S4**).

629 **(D)** Approach for supervised classification using a random forest (RF) classifier trained on
630 healthy bone marrow (BM) scRNA-seq data.

631 **(E)** Distribution (box plot and violin plot) of leukemia single-cell RF classification probabilities for
632 each healthy BM cell type, ordered by median RF classification probability.
633 “pDC”=plasmacytoid dendritic cell; “Ery”=erythroid; “Plasma”=plasma cell;
634 “GMP”=granulocyte-monocyte progenitor; “Mono”=monocyte.

635 **(F)** K-nearest neighbor (kNN) projection of all leukemia cells onto reference normal hierarchy,
636 annotated by number of classified leukemic cells for each reference B cell lineage population.

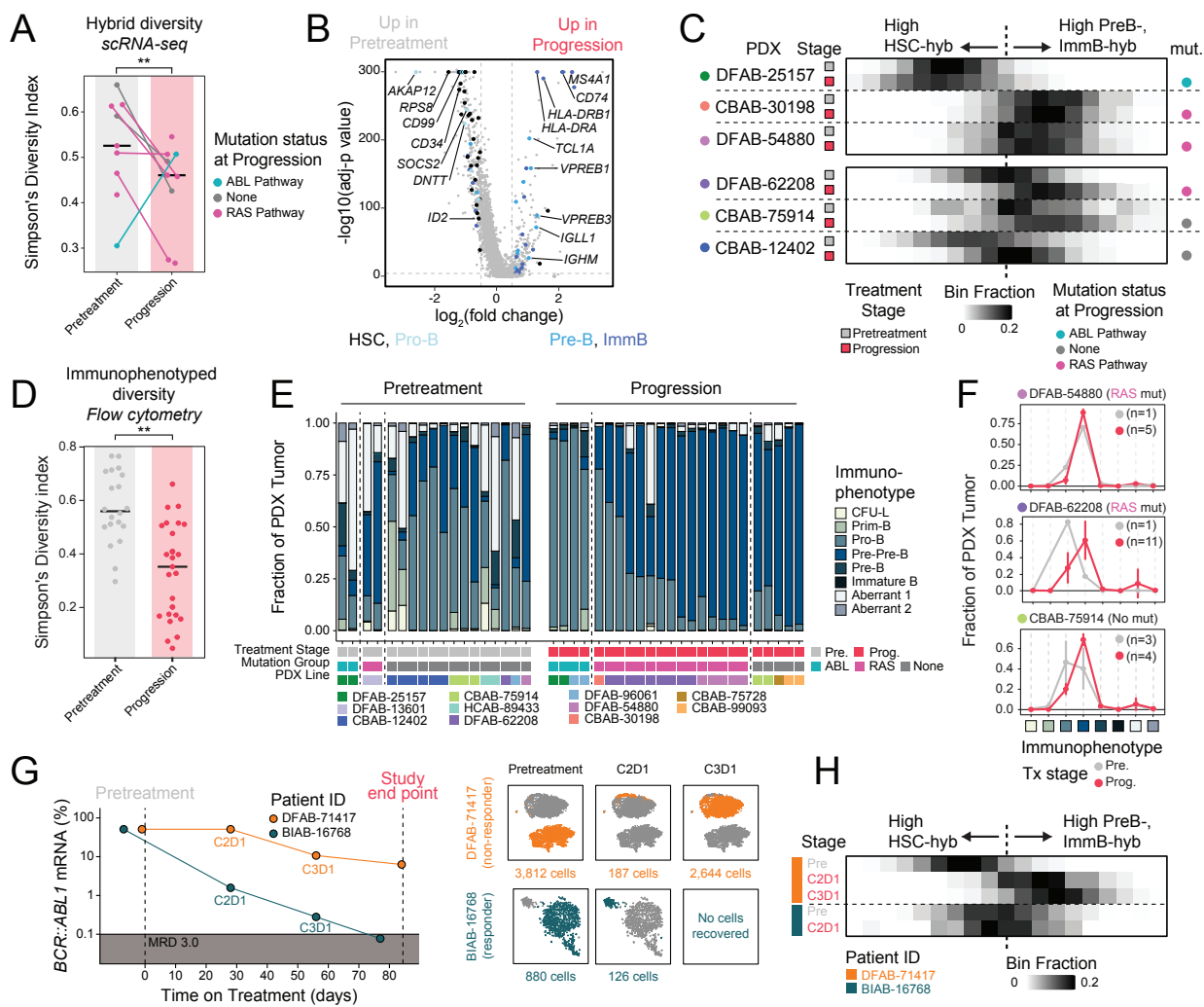
637 **(G)** Developmental marker gene co-expression in normal Pro-B cells (left) vs. leukemia cells
638 classified as Pro-B cells (right). X-axis represents gene expression score difference between
639 healthy HSC differentially expressed genes (undifferentiated) and the union of Pre-B and
640 Immature B differentially expressed genes (more differentiated); y-axis represents each cell’s
641 second highest healthy cell type marker expression score. 300 randomly-sampled single
642 cells from each bin are shown below. P-values from ANOVA (**p<0.001) compare expression
643 distribution in normal vs leukemic Pro-B cells for each normal cell type marker expression
644 score (rows).

645 **(H)** Leukemia cells plotted according to non Pro-B RF classification probabilities. Cells are
646 colored by RF Pro-B classification probability (greyscale, fill) and cells are outlined by their
647 classified cell type.

648

649 See also *Figures S3-S6; Tables S4 & S5*.

Figure 3



651 **Figure 3. Oncogene withdrawal drives convergence onto developmental hybrids.**

652 (A) Simpson's Diversity Index (SDI) of non ProB-like hybrid population proportions in each PDX
653 line, colored by mutation status at progression. Tied points represent paired PDX treatment
654 stages. Median SDI for pretreatment and progression across PDX lines plotted as a line.
655 Wilcoxon rank sum p-value (** $p<0.01$) reported, excluding ABL pathway mutated PDX line
656 (outlier DFAB-25157).

657 (B) Differentially expressed genes between PDX pretreatment and progression single-cells.
658 Marker genes for HSC, Pro-B, Pre-B, and Immature B cell types are annotated.

659 (C) Density of cells across the spectrum of hybrid developmental gene expression space,
660 calculated by the difference between later-stage hybrid scores (PreB-hyb, ImmatureB-hyb)
661 and progenitor hybrid scores (HSC-hyb). Rows are annotated by PDX line, time point, and
662 mutation ("mut.") status at progression.

663 (D) SDI of flow cytometry immunophenotyped B cell lineage populations within individual PDX
664 tumors at pretreatment and progression; median SDI indicated for pretreatment and
665 progression tumors. ** $p<0.01$ (Wilcoxon rank sum test).

666 (E) Fractional representation of immunophenotyped B cell lineage populations for 42 leukemia
667 samples from 11 PDX lines at pretreatment and progression time points. "Pre." =
668 pretreatment; "Prog." = progression. Immunophenotyped population flow cytometry markers
669 defined in **Figures S7B & S7C**.

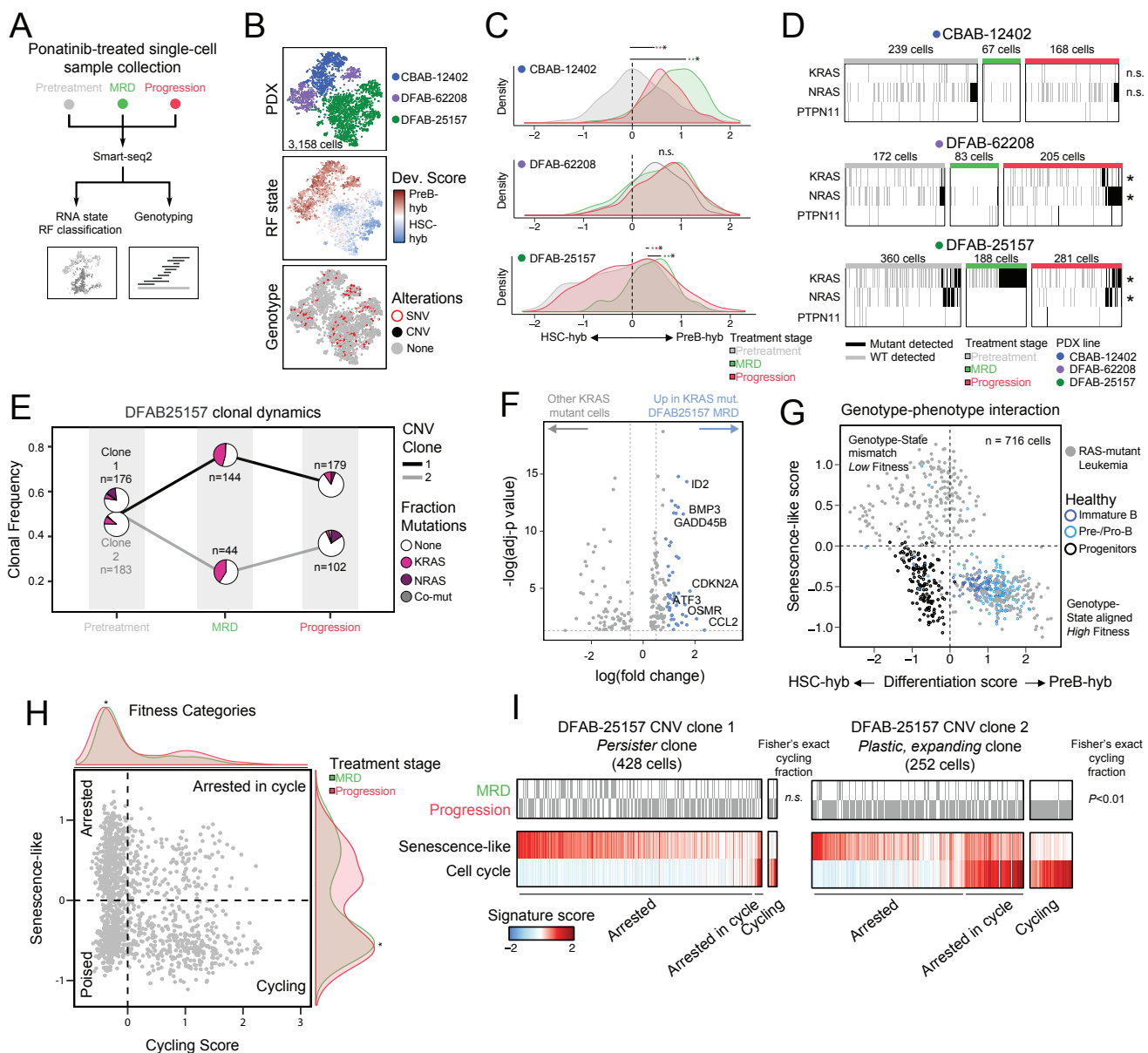
670 (F) Pretreatment and progression average immunophenotyped population proportions (as
671 plotted in (E)) for three representative PDX lines corroborate transcriptional trends in (C);
672 error bars indicate ± 1 standard deviation when at least 3 mice were profiled. Number of mice
673 profiled at each time point indicated for each PDX line. PDX lines are labeled based on
674 mutation group at progression.

675 (G) *BCR::ABL1* percent mRNA qRT-PCR traces ($\log_{10}(\text{BCR::ABL}/\beta\text{-Actin mRNA})$) from bone marrow
676 aspirates of two patients on combination ABL1 inhibition, including one representative responder
677 (BIAB-16768) and one non-responder (DFAB-71417), from a Phase I clinical trial (**Table S6**). MRD
678 3.0 indicates trial definition of remission tumor burden (3-log reduction in bone marrow *BCR::ABL1*
679 mRNA detected by qRT-PCR). Right: scRNA-seq data collected from patients at each treatment
680 cycle time point shown on t-SNE projections.

681 (H) Density of cells across the spectrum of hybrid developmental space, as defined in (C),
682 compared across paired patient pre-treatment and on-treatment time point bone marrow
683 aspirates.

684 See also *Figure S7; Table S6*.

Figure 4



686 **Figure 4. Developmental phenotypes restrict genotype fitness in remission.**

687 **(A)** Strategy for profiling three representative PDX models at pretreatment, MRD, and
688 progression with Smart-Seq2 (SS2).

689 **(B)** t-SNE visualizations for the leukemic cells collected with SS2 and labeled by PDX line (top),
690 developmental state (middle; “dev.”=development), and detected genetic alterations (bottom;
691 “SNV”=single nucleotide variant; “CNV”=copy number variant).

692 **(C)** Density distributions of leukemia cells at pretreatment, MRD, and progression time points
693 across HSC-hyb to PreB-hyb gene expression scores. * $p<0.001$ from KS test for each
694 pairwise comparison between treatment stages.

695 **(D)** Mutant or wild-type (WT) transcript detection for *KRAS*, *NRAS*, and *PTPN11* within single-
696 cells. Significant mutant transcript abundance between time points are annotated; * $p<0.05$
697 by Fisher exact test.

698 **(E)** Dynamics of CNV sub-clonal proportions at pretreatment, MRD, and progression in DFAB-
699 25157. Pie charts represent *KRAS* or *NRAS* fraction of each sub-clone at the indicated time
700 points. Number of cells sampled within each CNV sub-clone are reported.

701 **(F)** Differentially expressed genes between DFAB-25157 *KRAS*-mutant cells at MRD versus all
702 other *KRAS*-mutant cells, highlighting increased expression of genes implicated in
703 senescence (**Table S8**).

704 **(G)** RAS-pathway mutant leukemic cells plotted according to their differentiation gene expression
705 score on the x-axis, and senescence-like gene expression score on the y-axis. Overlaid
706 healthy progenitor, Pre-B, and Immature B cells colored by cell type.

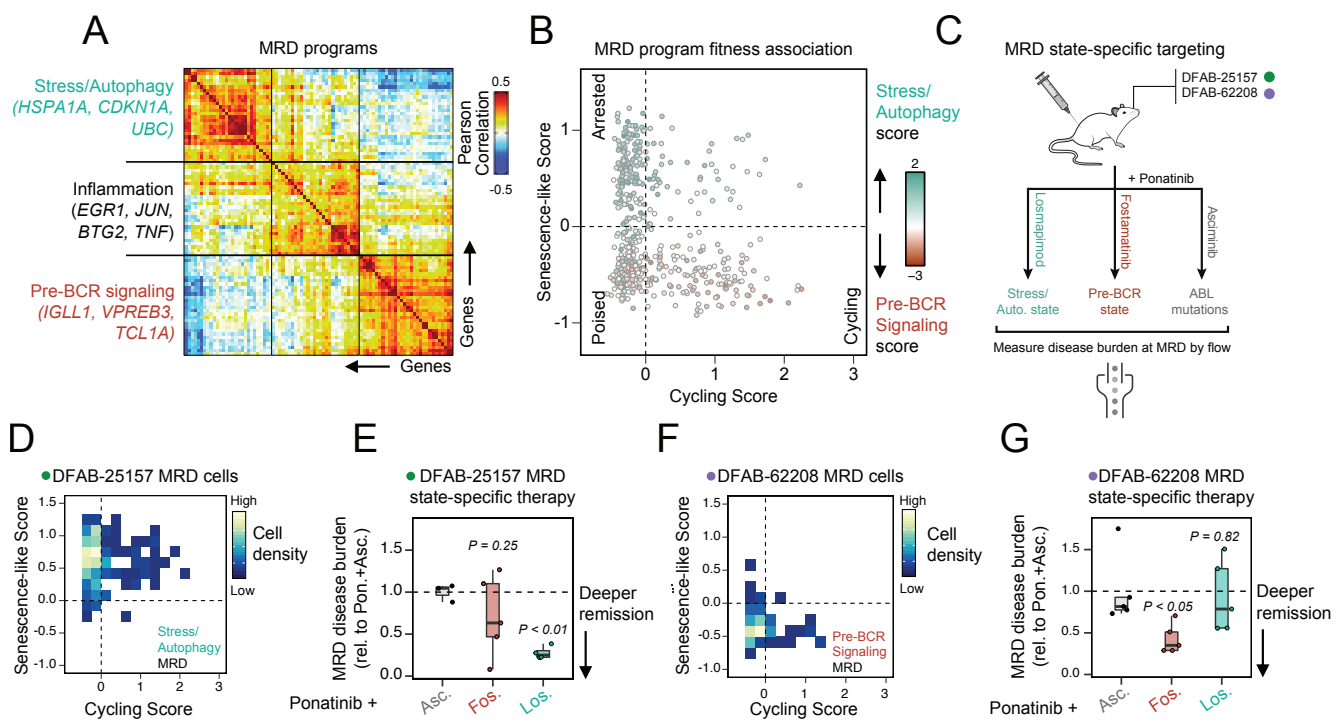
707 **(H)** Fitness landscape of cell-cycle arrested, poised, and actively cycling leukemic cells in
708 remission. Single-cells plotted by cycling (x-axis) and senescence (y-axis) signature scores.
709 Distributions for cells in each fitness quadrant shown (green=MRD, red=Progression;
710 * $p<0.001$ reported from KS test).

711 **(I)** DFAB-25157 leukemic cells from each CNV subclone ranked along senescence-like and cell
712 cycle signature scores. Fisher’s exact test p-value reported for the origin of cycling cells
713 (MRD vs. Progression). No cells belonged to the “poised” fitness category from either CNV
714 subclone.

715

716 See also *Figures S8 & S9; Tables S7 & S8*.

Figure 5



718 **Figure 5. Targeting integrative cell states enhances remission.**

719 **(A)** Pairwise Pearson correlation of genes defining MRD states (**Table S9**).

720 **(B)** Module scores for the Stress-Autophagy (turquoise) and Pre-BCR Signaling (dark red) states
721 projected over single-cells at MRD. Cells are plotted along fitness quadrants as in **Figure 4H**
722 by their cycling (x-axis) and senescence-like (y-axis) gene signature scores.

723 **(C)** Study design for testing MRD cell-state targeting.

724 **(D)** Cell fitness distribution for DFAB-25157 MRD cells.

725 **(E)** DFAB-25157 MRD bone marrow disease burden assessed by flow cytometry (y-axis, relative
726 to Ponatinib+Asciminib) in the respective treatment arms (“Asc.”=Asciminib;
727 “Fos.”=Fostamatinib; “Los.”=Losmapimod). T-test p-values reported, comparing losmapimod
728 and fostamatinib arms to asciminib reference.

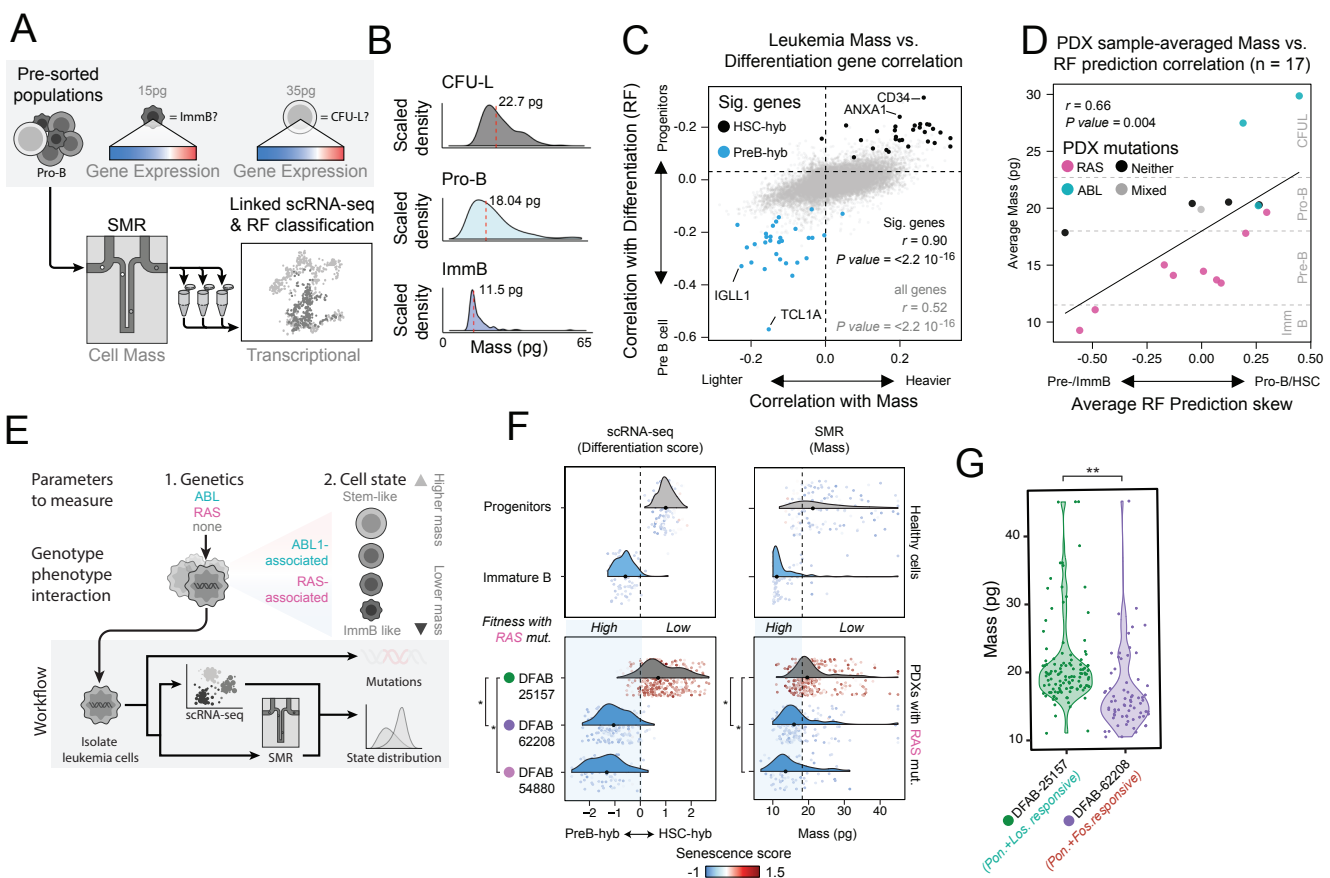
729 **(F)** Cell fitness distribution for DFAB-62208 MRD cells.

730 **(G)** DFAB-62208 MRD disease burden assessed by flow cytometry as in **(E)**. Reported t-test p-
731 values compare losmapimod and fostamatinib arms to asciminib reference.

732

733 See also *Figure S10; Table S9*.

Figure 6



735 **Figure 6. Biophysical measurements can be used as a surrogate for complex**
736 **transcriptional states.**

737 **(A)** Schematic for evaluating the relationship between complex transcriptional state and
738 integrative biophysical features.

739 **(B)** Mass distributions from the sorted populations in **(A)** measured using the SMR; median mass
740 reported.

741 **(C)** Leukemia cell mass-correlated genes (x-axis) are plotted against each gene's correlation to
742 developmental phenotypes (RF probability for progenitor and Pre-B cell types; y-axis).
743 Colored points mark genes included in the Progenitor and Pre-B SS2 signatures; "Sig.
744 genes"=Leukemia developmental marker genes.

745 **(D)** Average difference in RF prediction score between early and late stages of B cell
746 development (x-axis) versus average mass for each mouse (n=17), binned by distributions
747 in **(B)** and **Figure S11A**, and annotated by progression mutation status.

748 **(E)** Proposed workflow for comparing sequencing to biophysical measurements for diagnostics.

749 **(F)** Example application for pairing mutation and mass information to predict development and
750 fitness-integrated transcriptomic state. Density spectra of (left) developmental score and
751 (right) mass for (top) healthy progenitor cells and immature B cells, and (bottom) RAS-mutant
752 leukemic cells in three representative PDX lines. Dotted line for mass distribution represents
753 mean+1 standard deviation of healthy Immature B mass. Median differentiation scores or
754 mass for each PDX line are denoted as a dot; PDX lines are colored based on their median
755 similarity to Immature B or Progenitor differentiation scores or mass. * indicates significant
756 difference between DFAB-25157 differentiation score or mass distributions compared to
757 those of DFAB-62208 and DFAB-54880 (KS test, $p<0.001$). Individual cells are colored
758 according to their senescence signature score. Blue shaded region is the putative zone of
759 compatibility for RAS mutations and developmental state.

760 **(G)** Mass distributions for leukemia cells at MRD from DFAB-25157 (sensitive to combination
761 losmapimod) and DFAB-62208 (sensitive to combination fostamatinib). ** $p<0.001$ from
762 paired Wilcoxon test.

763

764 See also *Figure S11*.

765 **METHODS**

766 **RESOURCE AVAILABILITY**

767 **Lead Contact**

768 Further information and requests for resources and reagents should be sent to and will be fulfilled
769 by Dr. Peter Winter (pwinter@broadinstitute.org).

770 **Data Availability**

771 The scRNA-seq data and SMR data reported in this paper will be deposited in a central data
772 sharing repository (Genomic Data Commons) under the NCBI Database of Genotypes and
773 Phenotypes (dbGaP). scRNA-seq digital gene expression matrices, metadata, and interactive
774 visualization tools will additionally be available through the Alexandria Project, a Bill & Melinda
775 Gates Foundation-funded portal (part of the Single Cell Portal hosted by the Broad Institute of
776 MIT and Harvard). Code used for analysis will be available upon request.

777

778 **EXPERIMENTAL MODEL AND SUBJECT DETAILS**

779 **Generation and Use of PDXs**

780 Primary bone marrow and peripheral blood specimens were collected from patients with
781 leukemia at the Dana-Farber Cancer Institute, Brigham and Women's Hospital, and Boston
782 Children's Hospital for xenotransplantation. Additional PDXs that had already been established
783 through the Public Repository of Xenografts (PRoXe) were utilized.²⁷ De-identified patient
784 samples were obtained with informed consent and xenografted under Dana-Farber/Harvard
785 Cancer Center Institutional Review Board (IRB)-approved protocols. Nod.Cg-
786 *Prkdc*^{scid}/*IL2rg*^{tm1Wjl}/*SzJ* (NSG) mice were purchased from Jackson Laboratories and handled
787 according to Dana-Farber Cancer Institute Institutional Animal Care and Use Committee-
788 approved protocols. Salient PDX line metadata are provided in **Tables S1 & S2**.

789 ***In vivo* therapeutic studies**

790 Viable frozen Ph+ ALL xenograft cells were thawed and changed into 1X PBS before tail-vein
791 injection at 0.5-2.0*10⁶ cells per mouse. Engraftment was monitored by weekly peripheral blood
792 flow cytometry beginning three weeks after injection. Blood was processed with Red Blood Cell
793 Lysis Buffer (Qiagen #158904; Hilden, Germany) and stained with antibodies against human
794 CD45 (APC-conjugated, eBioscience #17-0459-42; San Diego, CA, USA) and human CD19
795 (PE-conjugated, eBioscience #12-0193-82) in 1X PBS with EDTA (2mM). Flow cytometry data
796 were analyzed using FlowJo software (BD Biosciences; Ashland, OR, USA). Upon engraftment

797 – when at least 10% of cells were positive for CD45 and CD19 – mice within each PDX line
798 underwent 1:2:2:4:1 randomization to the following arms and initiated treatment within two days:
799 (1) sacrifice for baseline tissue interrogation; (2) ponatinib (Selleckchem #S1490; Houston, TX,
800 USA; constituted in 25mM citrate buffer, pH 2.75) 40mg/kg via oral gavage (OG) daily; (3)
801 asciminib (NVP-ABL001, Novartis Pharmaceuticals; Basel, Switzerland; constituted in HCl 0.1M,
802 PEG300 30%, Solutrol HS15 6%, NaOH 0.1M, sodium acetate buffer pH 4.7 10mM) 30mg/kg
803 OG twice daily; (4) ponatinib 40mg/kg OG twice daily plus asciminib 30mg/kg OG BID; and (5)
804 vehicle (alternating doses of vehicle used for ponatinib and asciminib, at equivalent volumes).
805 One mouse per active treatment arm per PDX line was sacrificed on day 7 of treatment for
806 pharmacodynamic assessment. The remaining mice continued daily treatment under monitoring
807 with biweekly peripheral blood flow cytometry until progression (defined as peripheral blood
808 involvement of at least 10% on two consecutive assessments at least one week apart), weight
809 loss of greater than 20% from pre-treatment baseline, or clinical manifestations of advanced
810 disease, including but not limited to ruffled fur, hunched posture, hind limb paralysis, or lethargy.
811 Progression or toxicity as defined above triggered humane euthanasia by CO₂ asphyxiation,
812 necropsy to ascertain cause of death, and post-mortem harvest of peripheral blood, bone
813 marrow, and any soft tissue masses. Additional *in vivo* studies involved treatment with nilotinib
814 (Selleckchem #S1033), which was constituted in N-methyl-2-pyrrolidone (10%) in polyethylene
815 glycol (PEG)-300 (90%) and dosed at 50mg/kg OG twice daily.

816 Studies to define the *in vivo* activity of combination therapies targeting the biology of MRD
817 within individual PDX lines DFAB-62208 and DFAB-25157 utilized the same xenotransplantation
818 and engraftment monitoring scheme as previously described and the following drugs: ponatinib
819 (as above), asciminib (as above), fostamatinib (Selleckchem #S2206-50mg), constituted in 0.1%
820 carboxymethylcellulose sodium, 0.1% methylparaben, and 0.02% propylparaben (pH 6.5) and
821 dosed at 25mg/kg OG thrice daily, and losmapimod (Selleckchem #S7215-50mg), constituted in
822 1% DMSO in methylcellulose and dosed at 20mg/kg via the intraperitoneal (IP) route daily. Upon
823 engraftment (>10% leukemia involvement of peripheral blood), individual mice underwent live
824 femoral bone marrow aspirates under anesthesia with inhaled isoflurane delivered via precision
825 vaporizer and underwent 1:1:1 randomization to the combination of ponatinib and asciminib,
826 ponatinib and fostamatinib, or ponatinib and losmapimod. Animals initiated treatment within 48
827 hours of engraftment and continued treatment for 21 days ± 3 days, at which point they
828 underwent humane euthanasia, necropsy, and immediate post-mortem recovery of peripheral
829 blood and bone marrow from the femur contralateral to that which was aspirated upon
830 engraftment.

831 **Human donors for reference**

832 Normal human bone marrow aspirates were obtained from donors who provided informed
833 consent for tissue banking and research under Dana-Farber/Harvard Cancer Center IRB
834 protocols and were undergoing bone marrow harvest for unrelated hematopoietic stem cell
835 transplantation recipients. Briefly, bone marrow was collected into a Baxter bone marrow harvest
836 collection system with diluent consisting of sodium heparin in lactated Ringers solution. Bone
837 marrow was heparinized at a final concentration of 15-20 units/mL and filtered inline using
838 200 μ m and 500 μ m filters. Bone marrow mononuclear cells from the heparinized, filtered product
839 were isolated via density gradient centrifugation (Ficoll-Paque, ThermoFisher Scientific #45-001-
840 749) and subsequently underwent fluorescence-activated cell sorting (FACS) to isolate
841 hematopoietic developmental subpopulations for Seq-Well S³ and SS2 single-cell transcriptomic
842 profiling (see Methods Details).

843 **Phase I clinical trial**

844 Serial primary blood and bone marrow specimens were obtained from appropriately consented
845 patients treated on a phase I, investigator-initiated clinical trial (NCT03595917) of asciminib
846 (ABL001) in combination with dasatinib plus prednisone for adults with newly diagnosed Ph+
847 ALL or chronic myelogenous leukemia in lymphoid blast phase (CML-LBP). Some patients
848 cross-consented to a Dana-Farber Cancer Institute tissue banking protocol permitting additional
849 evaluation of primary specimens. Bone marrow was obtained at screening and after each 21-
850 day cycle through the first four cycles. Peripheral blood was obtained at screening and on days
851 2, 4, 8, 11, 15, and 22 (\pm 2 days) of cycle 1. Both bone marrow and peripheral blood were
852 collected into EDTA vacutainer tubes prior to mononuclear cell isolation per standard protocols.
853 Bone marrow and peripheral blood underwent clinical quantitative real time PCR for *BCR::ABL1*
854 mRNA according to the *BCR::ABL1* isoform detected at screening (p190 or p210). Curated sets
855 of Ph+ ALL clinically annotated specimens underwent evaluation by scRNA-seq (Seq-Well S³;
856 salient donor metadata provided in **Table S6**).

857

858 **METHOD DETAILS**

859 **Quantifying *BCR::ABL1* mRNA in PDX peripheral blood with qRT-PCR**

860 *BCR::ABL1* mRNA levels were measured via quantitative real-time PCR (qRT-PCR) of serial
861 peripheral blood specimens from PDX models to track kinetics of response and progression.
862 Briefly, xenografted mice were phlebotomized for 100 μ L by submandibular vein laceration every
863 two weeks. Blood was stored in RNAProtect tubes (Qiagen #76544). mRNA was isolated using

864 the RNeasy Protect Animal Blood Kit (Qiagen #73224) and quantified using the iScript One-Step
865 RT-PCR Kit with SYBR Green (Bio-Rad #170-8893) on a Bio-Rad CFX96 Thermal Cycler.
866 Synthesis of cDNAs was performed with random hexamers. Amplification of cDNAs was
867 performed using iTaq Universal SYBR Green Supermix (Bio-Rad #172-5125) and the following
868 oligomers:

869 *BCR::ABL1* isoform p190 forward: CAACAGTCCTTCGACAGCAG
870 *BCR::ABL1* isoform p190 reverse: CCCTGAGGCTCAAAGTCAGA
871 *BCR::ABL1* isoform p210 forward: TCCGCTGACCATCAATAAGGA
872 *BCR::ABL1* isoform p210 reverse: CACTCAGACCCTGAGGCTCAA

873 Positive control reagents for each isoform were p190 clonal control RNA (Invivofscribe #4-
874 089-2800) and mRNA isolated from the *BCR::ABL1* p210-positive cell line K562.

875 **Quantifying *BCR::ABL1* mRNA in primary patient peripheral blood with qRT-PCR**

876 *BCR::ABL1* mRNA was quantified in the peripheral blood of patients treated on clinical trial
877 NCT03595917 via CAP/CLIA-approved clinical *BCR::ABL1* qRT-PCR performed in the clinical
878 molecular laboratory of Brigham and Women's Hospital (Boston, MA).

879 **Targeted DNA Sequencing**

880 PDX models underwent mutational profiling with targeted panels. Leukemia cells were enriched
881 from fresh primary PDX bone marrow or peripheral blood via immunomagnetic enrichment for
882 human B cells using human CD19 MicroBeads (Miltenyi Biotec #130-050-301; Gaithersburg,
883 MD, USA). DNA was extracted using the DNeasy Blood & Tissue kit (QIAGEN #69504) and
884 fluorometrically quantitated using the Qubit dsDNA HS assay kit (Invitrogen #Q32854; Waltham,
885 MA, USA) prior to use in next-generation sequencing library preparation.

886 A hybrid-capture target enrichment panel targeting the full coding sequences of 183
887 genes selected based on the presence of recurrent mutations in hematologic malignancies was
888 utilized to profile most PDX models at baseline, on-treatment, and at end of study (as previously
889 described).⁶³ An amplicon-based clinical sequencing panel targeting hotspot regions of the
890 oncogenes and most of the coding regions of tumor suppressor genes recurrently implicated in
891 hematologic malignancies (total 93 genes) was employed for a subset of PDX models.⁶⁴ A
892 custom amplicon-based deep sequencing panel targeting 23 genes implicated in B-ALL
893 treatment resistance (ArcherDX; Boulder, CO, USA) was employed to profile PDXs progressing
894 after *BCR::ABL1* inhibition.

895
896

897 **Whole Exome Sequencing (WES) sample preparation**

898 PDXs that progressed in absence of treatment-emergent driver alterations detected by targeted
899 sequencing underwent whole exome sequencing using the SureSelect Human All Exon v5 kit
900 (Agilent Life Sciences; Santa Clara, CA, USA). Briefly, 100ng of genomic DNA from each
901 leukemia specimen as well as a control cell line (CEPH 1408) and a tail clipping from a non-
902 xenografted NSG mouse were fragmented to 250bp on a Covaris Ultrasonicator (Woburn, MA,
903 USA). Size-selected DNA fragments were ligated to xGen v1 UDI-UMI9 adaptors (Integrated
904 DNA Technologies; Coralville, IA, USA) during automated library preparation with a Biomek FX^p
905 liquid handling robot (Beckman Coulter; Indianapolis, IN, USA). Libraries (250ng per sample)
906 were pooled to 750ng and captured with the SureSelect Human All Exon v5 bait set. Captures
907 were pooled and sequenced on a HiSeq 3000 (Illumina; San Diego, CA, USA).

908 **Flow sorting of from healthy human bone marrow aspirates and PDX tumors**

909 Approximately 10⁶ cells per sample were resuspended in PBS with 4,6-diamidino-2-phenylindole
910 (DAPI; 0.75µg/mL) as a dead cell marker. For cell surface staining, PBS-washed cells were
911 blocked with Fc blocker for 10 min on ice and then stained with the antibodies listed in **Table S10**
912 at the manufacturers' recommended concentrations or with an isotype control for 25 min on ice.
913 Cells were then washed and resuspended in chilled PBS containing 0.75µg/mL of DAPI to
914 exclude dead cells. For annexin V staining, annexin V binding buffer (BD Biosciences) was used
915 instead of PBS, and 7-aminoactinomycin D (7-AAD; BD Biosciences) instead of DAPI.
916 Phycoerythrin (PE)-labelled annexin V was purchased from BD Biosciences. Acquisition was
917 performed on a LSR Fortessa flow cytometer (BD Biosciences). Fluorescence-based cell sorting
918 was performed on a FACS Aria II (BD Biosciences). FACS data were analyzed with FlowJo
919 software (FlowJo).

920 Cells expressing B cell lineage-defining surface proteins were enriched by FACS on a BD
921 FACS Aria II cell sorter (BD Biosciences; Franklin Lakes, New Jersey, USA) based on staining
922 with antibodies targeting the following markers: Annexin V, CD45, CD34, CD10, CD19, CD20,
923 and CD22. Healthy and immunophenotyped subpopulations were defined as in **Figures S4A &**
924 **S7B**. Lymphoid progenitor sub-populations then underwent scRNA-seq via Seq-Well S³ and
925 SS2.

926 **Sample preparation for scRNA-seq of clinical and PDX samples**

927 We used the Seq-Well S³ platform for massively parallel scRNA-seq to capture transcriptomes
928 of single cells on barcoded mRNA capture beads.³¹ Briefly, a single-cell suspension of 15,000
929 cells in 200µL RPMI media supplemented with 10% FBS was loaded onto single arrays

930 containing barcoded mRNA capture beads (ChemGenes). The arrays were sealed with a
931 polycarbonate membrane (pore size of 0.01 μ m), before undergoing cell lysis and transcript
932 hybridization. The barcoded mRNA capture beads were then recovered and pooled for all
933 subsequent steps. Reverse transcription was performed using Maxima H Minus Reverse
934 Transcriptase (Thermo Fisher Scientific EP0753). Exonuclease I treatment (NEB M0293 L) was
935 used to remove excess primers, followed by Second Strand Synthesis using a primer of eight
936 random bases to create complementary cDNA strands with SMART handles for PCR
937 amplification. Whole transcriptome amplification was carried out using KAPA HiFi PCR
938 Mastermix (Kapa Biosystems KK2602) with 2000 beads per 50- μ l reaction volume. Libraries
939 were then pooled in sets of eight (totaling 16,000 beads), purified using Agencourt AMPure XP
940 beads (Beckman Coulter, A63881) by a 0.6 \times solid phase reversible immobilization (SPRI)
941 followed by a 1 \times SPRI, and quantified using Qubit hsDNA Assay (Thermo Fisher Scientific
942 Q32854). The quality of whole transcriptome amplification (WTA) product was assessed using
943 the Agilent High Sensitivity D5000 Screen Tape System (Agilent Genomics) with an expected
944 peak at 800 base pairs tailing off to beyond 3000 base pairs and a small/nonexistent primer
945 peak.

946 Libraries were constructed using the Nextera XT DNA tagmentation method (Illumina FC-
947 131–1096) on a total of 750pg of pooled cDNA library from 16,000 recovered beads using index
948 primers with format as previously described.³¹ Tagmented and amplified sequences were
949 purified at a 0.6 \times SPRI ratio yielding library sizes with an average distribution of 300 to 750bp in
950 length as determined using the Agilent High Sensitivity D5000 Screen Tape System (Agilent
951 Genomics). Two arrays were sequenced per sequencing run with an Illumina 75 Cycle NextSeq
952 500/550 v2 kit (Illumina FC-404–2005) at a final concentration of 2.4pM. The read structure was
953 paired end with Read 1 starting from a custom Read 1 primer containing 20 bases with a 12-bp
954 cell barcode and 8-bp unique molecular identifier (UMI) and Read 2 containing 50 bases of
955 transcript sequence.

956 **Sample preparation for paired SMR mass profiling and SMART-Seq2**

957 For all PDX and healthy bone marrow samples, cells were adjusted to a final
958 concentration of 2.5*10⁵ cells/ml to load single cells into the mass sensor array and record
959 single-cell mass measurements, as previously described.^{41,65} In order to exchange buffer and
960 flush individual cells from the system, the release side of the device was constantly flushed with
961 PBS at a rate of 15 μ L per minute. Upon detection of a single-cell at the final cantilever of the
962 SMR, as indicated by a supra-threshold shift in resonant frequency, a set of three-dimensional
963 motorized stages (ThorLabs) was triggered to move a custom PCR-tube strip mount from a

964 waste collection position to a sample collection position to retrieve the cell. Each cell was
965 dispensed in approximately 5 μ l of PBS into a PCR tube containing 5 μ l of 2 \times TCL lysis buffer
966 (Qiagen) with 2% v/v 2-mercaptoethanol (Sigma) for a total final reaction volume of 10 μ l. After
967 each 8-tube PCR strip was filled with cells, the strip was spun down at 1,000 g for 30 seconds
968 and immediately snap-frozen on dry ice. Following collection, samples were stored at -80 C prior
969 to library preparation and sequencing.

970 Single-cell lysates were compiled from independent collections upon thawing and
971 transferred into wells of a 0.2mL skirted 96-well PCR plate (Thermo Fisher Scientific). scRNA-
972 seq libraries were generated using SMART-Seq2 protocol.⁶⁶ Briefly, cDNA was reversed
973 transcribed from single cells using Maxima RT (Thermo Fisher Scientific) and whole
974 transcriptome amplification (WTA) was performed. WTA products were purified using the
975 Agencourt AMPure XP beads (Beckman Coulter) and used to prepare paired-end libraries with
976 Nextera XT (Illumina). Single cells were pooled and sequenced on a NextSeq 550 sequencer
977 (Illumina) using a 75 cycle High Output Kit (v2.5) with a 30bp paired end read structure.
978

979 QUANTIFICATION AND STATISTICAL ANALYSIS

980 PDX *in vivo* studies: survival analysis on treatment arms and with pretreatment clinical 981 risk stratification metadata

982 Analyses fitting a Cox proportional hazards model for overall survival (OS) and progression-free
983 survival (PFS) outcomes on treatment arms and pretreatment clinical risk stratification
984 categories were performed using the *survival* package in R.⁶⁷ The following pre-clinical features
985 included: *IZKF1* deletion, 9p deletion, hyperdiploid karyotype, gain of chromosome 21,
986 presenting white blood cell count, age, sex (if age <18 years), race, phase of disease, number
987 of prior therapies, and pre-existing *ABL1* mutation(s). Hazard ratios and p-values for PFS within
988 pretreatment clinical risk categories were generated relative to the lowest risk group in each
989 category (**Figure S1D**).

990 WES alignment and variant calling

991 Pooled sequenced WES samples were demultiplexed using Picard tools. Read pairs were
992 aligned to the hg19 reference build using the Burrows-Wheeler Aligner.⁶⁸ Data were sorted and
993 duplicate-marked using Picard tools. Alignments were refined using the Genome Analysis
994 Toolkit (GATK)^{69,70} for localized realignment around small insertion and deletion (indel) sites.
995 Mutation analysis for single nucleotide variants was performed with MuTect v1.1.4⁷¹ and
996 annotated by Variant Effect Predictor.⁷² Indels were called using the SomaticIndelDetector tool

997 of the GATK. Copy number variants (CNVs) were identified using RobustCNV for autosomes.⁷³
998 Detected alterations are reported in **Table S3** and **Figure S2A**.

999 **scRNA-seq sequencing alignment and quality control**

1000 Sequenced Seq-Well BCL files were demultiplexed into individual sample FASTQs for Read 1
1001 and Read 2 using the bcl2fastq pipeline on Terra, as previously described. The resultant paired
1002 read FASTQs were aligned to the hg19 genome using the cumulus/dropseq_tools pipeline on
1003 Terra maintained by the Broad Institute using standard settings, generating a genes by cells
1004 count matrix for each sample.⁷⁴ Low quality cells were filtered using nGene≤200, nUMI≤500,
1005 and percent mitochondrial transcripts≤30% thresholds before merging samples; genes were
1006 filtered if they were not expressed in at least 10 cells.

1007 Sequenced SS2 BCL files were similarly demultiplexed using bcl2fastq and aligned to the
1008 hg19 genome using publicly available scripts on Terra (github.com/broadinstitute/TAG-public).
1009 Total gene counts and transcript per million (TPM) matrices were filtered to remove low quality
1010 cells with <15% transcriptome mapping, 2,000 genes, and 45,000 mapped reads, before
1011 continuing analysis. Genes expressed in fewer than 10 cells, as well as long non-coding RNAs
1012 and unique hg19 reference-build variants were removed before downstream analysis.

1013 **Human healthy bone marrow reference cell type clustering and visualization**

1014 After QC filtering, 13,643 high quality cells from 7 healthy human bone marrow donors were
1015 analyzed in Seurat v2.3.4 to classify hematopoietic cell types.⁷⁵ After normalization, the top
1016 1,500 highly dispersed variable genes were selected using the mean-variance plot method in
1017 Seurat's FindVariableFeatures function. ScRNA-seq data was scaled over highly variable genes
1018 and used as input for PCA analysis. The top significant PCs, as defined by the JackStraw test
1019 (top 25 PCs), were used as input for building a SNN graph to cluster cells by their (k=35) nearest
1020 neighbors and for t-SNE visualization of clusters. Given the shared, continuous hierarchy of
1021 covarying gene expression in hematopoietic development, broad cell types (progenitor, myeloid,
1022 erythroid, B cell lineage, pDCs, T cells, and Plasmablasts) were called based on their
1023 differentially expressed genes (identified using the Wilcox test in Seurat's FindAllMarkers
1024 function), and subset into individual Seurat objects for a second round of clustering to resolve
1025 the final 13 cell types defined in **Figure S4**. Cell type annotations were *post-hoc* validated based
1026 on biased or exclusive expression of known marker genes (**Figure S4D**).

1027 SS2 healthy reference cell types were called by their confident random forest prediction
1028 probabilities (see next section) and examination of marker genes to provide further support of
1029 cell type identification (**Figure S8B**). Cell type clusters were visualized using SPRING, a tool

1030 that generates force-directed layouts from kNN graphs to visually preserve hierarchical
1031 relationships between cell types.⁷⁶

1032 **Unbiased identification of consensus intratumoral gene expression programs with NMF**

1033 We sought to identify common axes of covarying intratumoral gene expression within all Ph+
1034 ALL tumors in our dataset. First, we ran consensus NMF (cNMF) on each tumor in our dataset
1035 (n=52 total samples, defining bone marrow and spleen samples from the same mouse as
1036 individual tumors).⁷⁷ For this analysis, we selected a consensus 1,489 variable genes across all
1037 tumors by first identifying the top 2,500 variable genes within each individual tumor using the
1038 variance standardized transformation method in Seurat v5.0.2 FindVariableFeatures function.
1039 To ensure consensus variable gene selection was not biased by PDX line- or patient-specific
1040 variable genes, as some models or donors had more tumors sampled than others, we initially
1041 selected the top 2,000 median weighted variable genes across tumors within a PDX line or
1042 patient, and then chose the top 2,000 median weighted variable genes across all PDX line and
1043 patient median gene lists. 511 of these top 2,000 variable genes were removed based on non-
1044 zero expression across all 52 tumors.

1045 cNMF (1,000 iterations) was performed on the counts matrices of each tumor utilizing the
1046 consensus variable gene list over a range of k=3-9. All stable solutions of k, defined by a cNMF
1047 solution silhouette score>0.8 across iterations, were evaluated for optimal k selection using the
1048 following heuristics. We first hierarchically clustered the Jaccard Similarity of the top 50 genes
1049 from each factor across all stable k solutions; under-clustered k solutions were nominated based
1050 on factors that contained genes split across clusters that were hierarchically clustered in higher
1051 k factorizations, and over-clustered k solutions were nominated based on the presence of factors
1052 that did not hierarchically cluster with lower k factorizations or split genes across multiple lower
1053 k factors.⁷⁸ To further evaluate these hypothesized over- or under-clustered k solutions, we
1054 scaled the data and ran UMAP projections over the top 50 genes from each factor for each
1055 stable k solutions. We used Seurat's AddModuleScore function over the top 50 genes from each
1056 factor to assess whether under-clustered factors convolved expression across UMAP
1057 subclusters of optimal k solutions, or whether over-clustered factors scored highest in the same
1058 subcluster of cells or mostly strongly defined 1-2 cells ("junk" factor). Finally, we assessed
1059 significant Pearson correlation of the top 50 genes in each optimal k factor over an expression-
1060 binned bootstrapped null distribution as previously described,⁷⁹ removing factors that were not
1061 significantly correlated (typically "activity"-like continuous programs in UMAP projections that,
1062 upon inspection, actually contained sparsely expressed genes of redundant biological
1063 annotations to other factors within that k solution). Factors from the selected optimal k that

1064 contained significantly correlated genes were labeled as “intratumoral gene expression
1065 programs” or GEPs, and collated for downstream intertumoral comparisons across the entire
1066 tumor cohort. Examples of intratumoral GEPs from representative PDX and patient tumors are
1067 shown in **Figure S3B**.

1068 From performing intratumoral cNMF on 52 tumors, we identified 166 intratumoral GEPs.
1069 We excluded outlier GEPs by constructing a kNN graph ($k=15$) and filtered 40 intratumoral GEPs
1070 using an elbow-based filtering criterion over kNN distances of each individual GEP to its nearest
1071 neighbor. The remaining 126 intratumoral GEPs were hierarchically clustered using Ward.D
1072 clustering over their cosine similarity to reveal 7 meta-GEPs or “mGEPs”, which we interpret as
1073 shared intratumoral gene covariation across at least 8 individual tumors (**Figure S3A**). To
1074 interpret shared gene covariation across each identified mGEP, we isolated the top 30 median
1075 gene loadings across intratumoral GEPs within a given mGEP cluster (**Figures 3C & S3A; Table**
1076 **S4**).

1077 **Training and interpreting the random forest classifier**

1078 Random forest is an ensemble machine learning method used for both classification and
1079 regression. Like other ensemble models, random forests combine multiple weak classifiers, in
1080 this case shallow decision trees, to make predictions. In this work, a random forest was used for
1081 classification. Here, we interrogate aberrant developmental hierarchies in ALL by using random
1082 forests to predict the nearest cell type from the normal B-cell lineage for single cells from Ph+
1083 ALL samples. There are inherent advantages to random forests for the Ph+ ALL classification
1084 task. Importantly, ensemble classifiers, like a random forest, provide a distribution of class
1085 probabilities reflecting the similarity of each cell to each cell type the model was trained on. This
1086 is done by calculating the proportion of trees voting for a cell type for each given observation.
1087 To generate a single prediction for a cell, the highest-class probability becomes the prediction.
1088 The higher the probability of the chosen class, the more transcriptionally similar the cell is to that
1089 stage of B cell development. The distribution of class probabilities itself can be used to
1090 understand the certainty – or uncertainty – of a prediction. We leveraged this measure of
1091 uncertainty in predictions to evaluate how well a tumor cell fits a specific stage in B cell lineage
1092 (**Figure 2H**). A tumor cell with a more uniform distribution of probabilities over classes likely
1093 shares transcriptional features with many a wider range of stages of B cell development,
1094 potentially indicating a more aberrant cell from normal development. Second, ensemble
1095 approaches tend to be more robust to overfitting, which is necessary when applying a model
1096 trained on sorted, healthy populations of cells to evaluate aberrant leukemic cells. Finally,
1097 because random forests are nonparametric models, they also are highly flexible to input feature

1098 scale and variance. This makes the approach particularly suited to raw count matrices output by
1099 various scRNA-seq technologies used.

1100 Here, we trained a random forest on sorted cells from the B cell lineage using 15,000
1101 genes with detected expression in more than 10 cells as input features. Random forests were
1102 implemented using R version 3.5.1 using the caret package for training infrastructure.⁸⁰ The
1103 ranger implementation of random forests was used.⁸¹ Hyperparameter search over ranger
1104 parameters (the number of randomly selected features considered for splitting at each tree node
1105 and the rule used for splitting) was done via 10-fold cross-validation (CV). The model achieved
1106 an accuracy of 94±0.006% on 10-fold CV with optimal parameters. The final model used the full
1107 training set of 13,643 cells. Results of 10-fold cross validation are provided in **Figure S5A**. The
1108 model was also evaluated on an external testing set of Seq-Well generated healthy bone marrow
1109 scRNA-seq transcriptomes,¹⁶ and achieved performance of average AUC=0.99 over all 13 cell
1110 types (**Figure S5C**). To interpret features being used to make predictions by the classifier, we
1111 used permutation importance tests. Permutation importance measures the impact of randomly
1112 shuffling feature values on the performance of a model measured as accuracy and decrease in
1113 Gini impurity. Specifically, a computationally accelerated heuristic method was used that
1114 constructs a null distribution from features that have importance values close to zero, limiting the
1115 need for randomly shuffling all features independently to evaluate significance.⁸² The results of
1116 feature importance defining marker genes segregating the 13 cell types can be found in **Figure**
1117 **S5B**.

1118 **Generating Tumor Hybrid Scores and assigning leukemia cells to hybrid populations**

1119 Tumor Hybrid gene signatures were generated as previously described.¹⁶ First, normalized gene
1120 expression values were correlated to RF cell type classification probabilities along B cell
1121 progenitor cell types (HSC, Pre-B, and Immature B). Pro-B RF probability correlations were
1122 excluded; since most leukemic cells were dominantly classified as Pro-B with secondary
1123 classifications along B cell lineage cell types, genes that highly correlated to Pro-B RF
1124 probabilities were not Pro-B-specific. To ensure that genes in each hybrid population signature
1125 were specific and unique to HSC, Pre-B, and Immature B cell types, the second-highest cell type
1126 correlation coefficient was subtracted from the highest correlation coefficient for a given cell type.
1127 Additionally, to ensure that cell type signatures were not obfuscated by cell cycle, positive
1128 correlation values of genes with cell cycle scores were subtracted from the highest correlation
1129 coefficient of a given cell type. After performing these corrections, the top 30 correlated genes
1130 to HSC, Pre-B, and Immature B cell types were included in their respective hybrid gene
1131 signatures; a threshold of 30 genes was selected based on the approximate elbow in corrected

1132 correlation values for each hybrid signature. Likewise, Pro-B gene scores were defined by the
1133 top 30 differentially expressed genes in healthy Pro-B cells (**Figures S6A; Table S5**).

1134 Tumor cells were scored by these HSC, Pro-B, Pre-B, and Immature B gene signatures
1135 using the Seurat v4 AddModuleScore function, and consequently assigned to hybrid populations
1136 similarly to what has been described previously.⁶⁰ Single cells were classified into HSC-like,
1137 PreB-like, and Immature-like hybrid populations based on their highest hybrid cell type signature
1138 score, which we required to be $> 0.5 +$ that cell's Pro-B score. All other cells were classified as
1139 Pro-B like cells, which were characterized by strong Pro-B gene expression and weak or no co-
1140 expression of other cell type hybrid signature scores. The classifications based on these hybrid
1141 score distributions and relative to their B cell lineage RF prediction probabilities is demonstrated
1142 in **Figure S6B**.

1143 **Mutual information of transcription factor activities with tumor hybrids**

1144 We sought to elucidate gene programs whose activity associated with the tumor hybrid
1145 populations defined above. Given the highly entropic co-expression of tumor hybrid signatures
1146 with Pro-B marker genes, we utilized mutual information as a metric for the potentially non-linear
1147 mutual dependence of gene expression with hybrid-defined developmental marker genes. Within
1148 respective hybrid subpopulations of each individual PDX line's pre-treatment and progression
1149 time points, we calculated the average normalized mutual information (NMI) of all highly
1150 expressed genes across the top 30 genes in each hybrid population signature, using raw gene
1151 counts as input. Within each PDX sample and hybrid population, MI values between each gene-
1152 gene pair were generated using R infotheo package mutinformatiion function with the Miller-
1153 Madow asymptotic bias corrected empirical estimator and normalized to scale values between
1154 0 and 1 as a relative, comparable metric between samples.⁸³ We interpret these NMI values as
1155 a metric for genes whose expression relatively scale with hybrid population identity.

1156 To identify cooperatively expressed genes that are collectively mutually informed with
1157 tumor hybrid signatures, we utilized the collectRI transcription factor accessibility database along
1158 with the decoupleR package to *in silico* predict mutually informed transcription factor (TF) activity
1159 with tumor hybrid identity.⁸⁴ Averaged NMI values for each PDX sample hybrid were used as
1160 input with the run_ulf function to estimate the linear relationship between TF-target genes and
1161 their hybrid marker gene expression. Within each PDX samples, significant TFs were ordered
1162 by their variance in mutually informed activity between hybrid populations, and the top 30 of
1163 these TFs were selected for further inspection of scaled predicted activity between hybrid
1164 subsets. NMI values and *in silico* predicted TF activities for each healthy reference population
1165 (HSC for HSC-hyb, Pre-BI and Pre-BII for PreB-hyb, Immature B for ImmB-hyb) were generated

1166 analogously and *post-hoc* compared to their leukemic hybrid counterparts (subset shown in
1167 **Figure S6D**), demonstrating that the majority of leukemic hybrid-defining TF activities were
1168 conserved with their healthy counterparts, with a couple of TFs.

1169 **Defining developmental skews in Smart-seq2 PDX samples**

1170 Given the paucity of RF-classified immature B cells in the SS2 leukemic dataset (**Figure S8A**),
1171 we identified genes that were Pearson correlated with Pre-B RF probabilities and with progenitor
1172 population (HSC, GMP, Pro-Mono, Early-Erythroid) probabilities. We found that genes
1173 correlated with progenitor RF probabilities negatively correlated with Pre-B RF probabilities in
1174 leukemic cells and vice versa, enabling us to define a spectrum of differentiation between
1175 progenitor and later-stage B cell developmental stages (**Figures S8C & S8D**). Progenitor-like
1176 and PreB-like scores were generated by scoring leukemic cells over the top 30 genes
1177 significantly correlated to their respective RF probabilities (**Table S7**). Each cell's location on the
1178 leukemic differentiation spectrum was defined by its (PreB-like score – Progenitor-like score).

1179 **Identifying somatic variants in full-length Smart-seq2 (SS2) scRNA-seq libraries**

1180 Each sample's SS2 FASTQ files were aligned to hg19 using STAR (version 2.6.0c) and then
1181 sorted and indexed with SAMtools (version 1.13).^{85,86} 16 genomic loci, nominated based on
1182 recurrently identified SNVs from bulk RNA-seq in the genes *KRAS*, *NRAS*, *PTPN11*, *GNB1*,
1183 *ABL1*, and *STAT5A* (**Figure S9A; Table S3**), were assessed for wild-type or mutant transcript
1184 detection by a custom script utilizing the Pysam library (version 0.16.0.1).⁸⁷ In particular, for each
1185 locus of interest, each cell was marked as "NC" if there was no coverage at the locus, marked
1186 with 0 if all overlapping reads matched the reference allele, or marked as mutant if there were
1187 overlapping reads that did not match the reference allele.

1188 **Predicting chromosomal number variations (CNVs) in SS2 scRNA-seq libraries with
1189 inferCNV**

1190 To identify SS2 leukemic cells harboring CNVs and *in silico* elucidate subclonal heterogeneity
1191 within tumors, we estimated single-cell CNVs as previously described by computing the average
1192 expression in a sliding window of 100 genes within each chromosome after sorting the detected
1193 genes by their hg19 genome-defined chromosomal coordinates.^{88,89} We used all healthy bone
1194 marrow SS2 cells identified above (**Figure S8B**) as reference normal populations for this
1195 analysis. Complete information on the inferCNV workflow used for this analysis can be found
1196 here: <https://github.com/broadinstitute/inferCNV/wiki>, using baseline input parameters for SS2
1197 data and for the i6 HMM algorithm for confident CNV-positive or negative predictions in single-
1198 cells.

1199

Module scoring single-cell transcriptomes

1200

Module scores of all gene signatures over single-cells were annotated using the Seurat v4 AddModuleScore function, which calculates the average expression levels of genes in a gene list relative to all other genes with comparable normalized gene expression. Quiescent cells were binned based on positive scores for a literature-derived quiescence gene signature derived from human hematopoietic cells.⁹⁰ We utilized previously established signatures for G1/S (n=43 genes) and G2/M (n=55 genes) to place each cell along this dynamic process;⁸⁹ after inspecting the distribution of scores in the complete dataset, we considered any cell > 1.5 SD above the mean for either the G1/S or the G2/M scores to be cycling.¹⁶ Senescence scores were derived from the top 50 genes significantly differentially expressed in the SS2 DFAB-25157 RAS-mutant cells in remission compared to all other RAS-mutant SS2 cells (**Figure 4F; Table S8**).

1210

Defining stress-autophagy, pre-BCR signaling, and inflammation transcriptional programs at remission

1211

To define heterogeneous, correlated transcriptional states defining PDX tumors that emerge in MRD, we first performed differential gene expression analysis between paired pre-treatment and MRD cells within the same PDX line to identify genes that significantly increase expression at remission. A total of 40 MRD state-defining genes were identified based on significant upregulation in at least two PDX-specific MRD differentially expressed gene (DEG) lists. Performing gene-gene Pearson correlation across the expression of these 40 shared MRD-high DEGs in all remission leukemic cells revealed three correlated modules of genes. To expand these three modules, we identified the top 30 genes significantly correlated (>2 standard deviations above median Pearson correlation) with the top differentially expressed gene in each module (**Table S9**). Pathway enrichment of significantly correlated genes was performed over msigDB Reactome gene sets for functional annotation, and to nominate targeted inhibitors of state (**Figures S10C**).

1224 **SUPPLEMENTARY INFORMATION**

1225

1226 **Table S1. Clinical characteristics of patients whose tumors were used to generate PDX**
1227 **models.**

1228 *Related to Figure 1*

1229 **Table S2. Characteristics of PDX models.**

1230 *Related to Figure 1*

1231 **Table S3. Detected Alterations in PDX Leukemias.**

1232 *Related to Figure 1*

1233 **Table S4. cNMF meta-GEP gene lists.**

1234 *Related to Figure 2*

1235 **Table S5. Seq-Well derived Tumor Hybrid signatures.**

1236 *Related to Figure 2*

1237 **Table S6. Patient characteristics and clinical trial outcomes.**

1238 *Related to Figure 3*

1239 **Table S7. SS2-derived Tumor Hybrid signatures.**

1240 *Related to Figure 4*

1241 **Table S8. Senescence-Like signature.**

1242 *Related to Figures 4*

1243 **Table S9. MRD State signatures.**

1244 *Related to Figure 5*

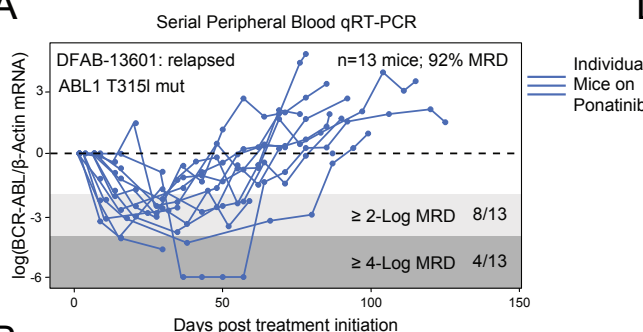
1245 **Table S10. Flow cytometry antibodies.**

1246 *Related to Methods*

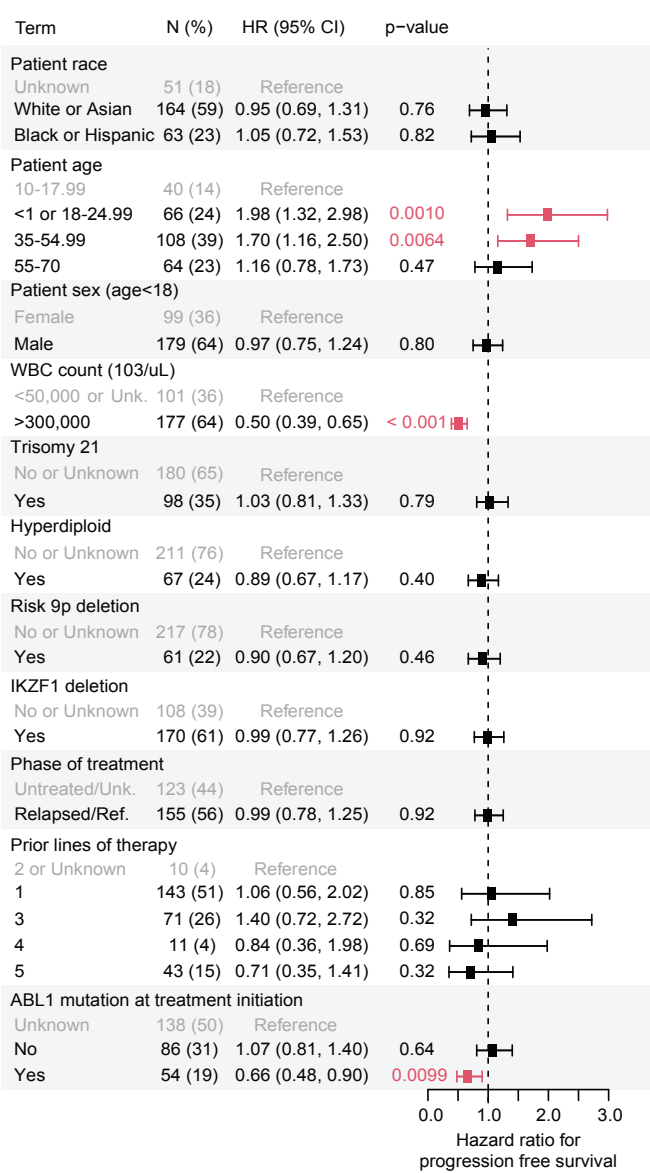
1247 **Figures S1-11.**

Supplemental Figure 1

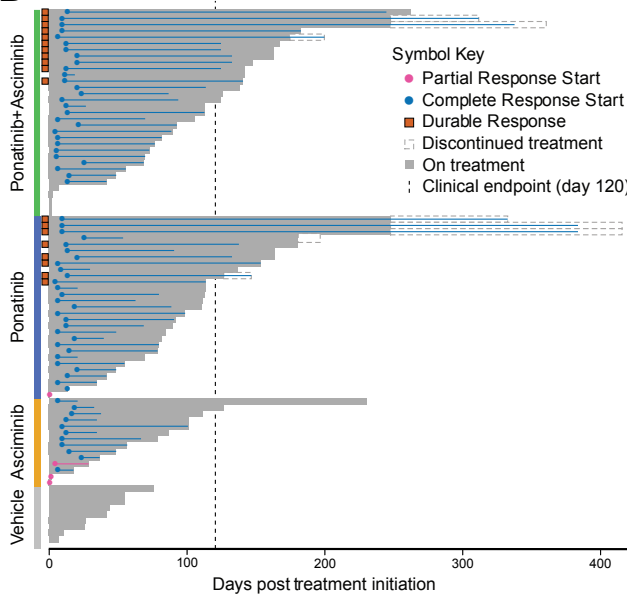
A



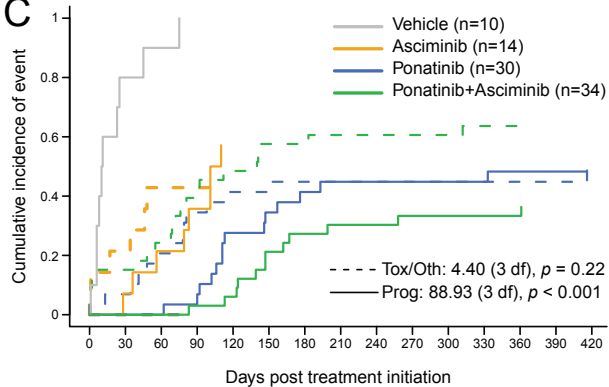
D



B



C



1249 **Figure S1. *In vivo* PDX Phase II-like trial outcomes.**

1250 *Related to Figure 1*

1251 **(A)** Serial peripheral blood *BCR::ABL1* qRT-PCR measurements from PDX model DFAB-13601
1252 treated with Ponatinib daily (40mg/kg/day); each line represents an individual mouse.

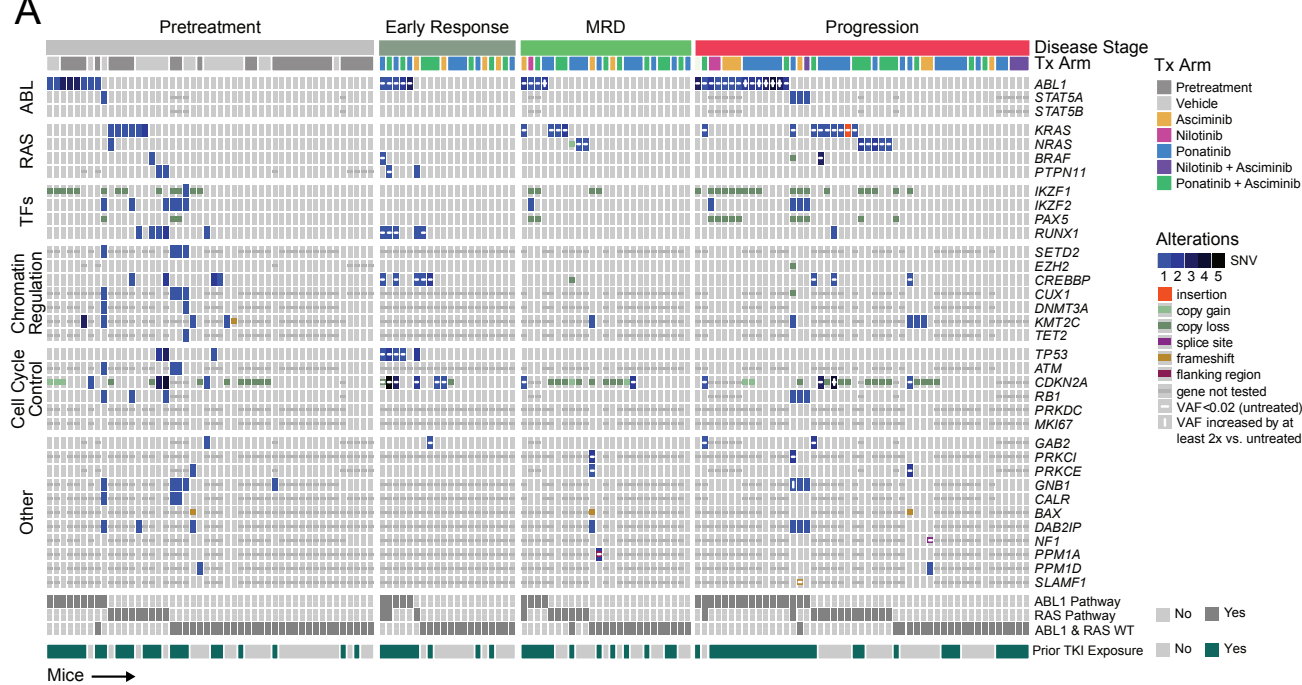
1253 **(B)** Key trial events and outcomes for each mouse on Phase II-like trial, grouped by treatment
1254 arm. Complete response indicates <4% peripheral blood circulating blasts detected via flow
1255 cytometry; partial response indicates reduced peripheral blood blasts compared to
1256 pretreatment but >1% involvement; durable response indicates complete remission past 120
1257 days on therapy.

1258 **(C)** Competing risks model comparing progression and non-progression mortality in mice by
1259 treatment arm; p-values from a Cox regression analysis indicated for differences in
1260 progression and non-progression outcomes between treatment arms.

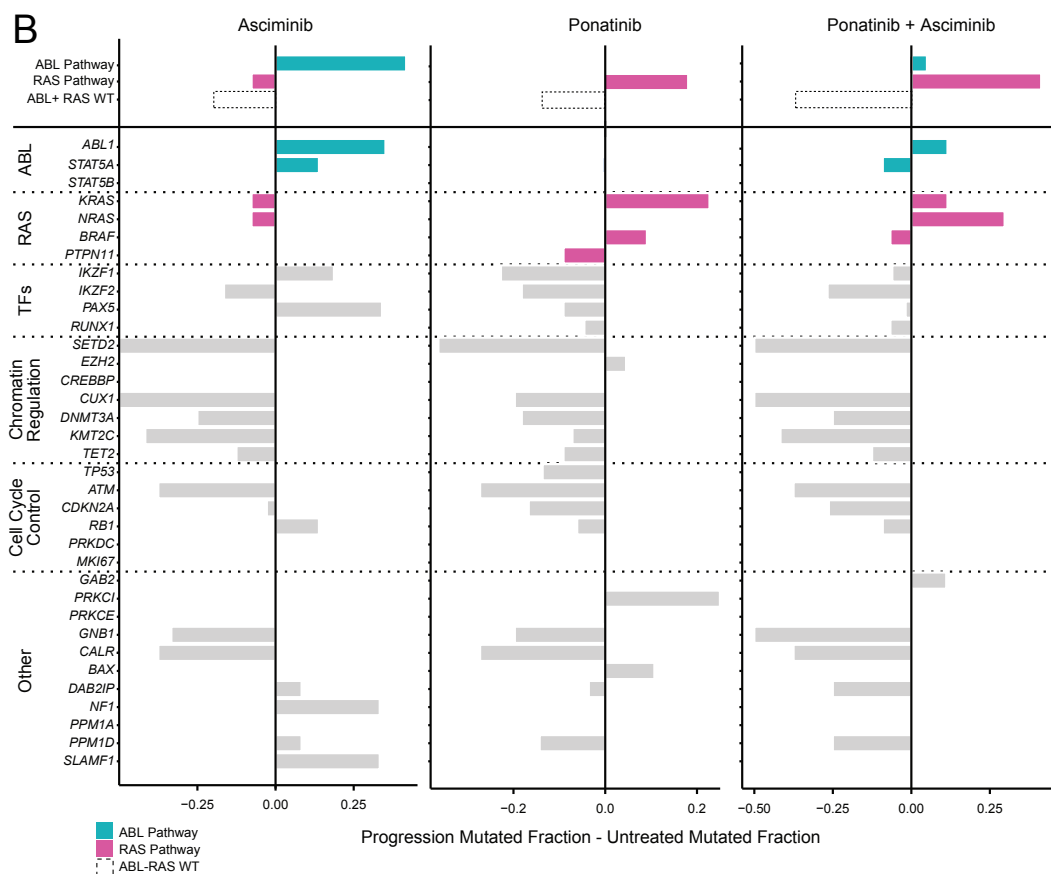
1261 **(D)** Hazard ratios comparing pre-clinical risk factors for progression free survival in PDX mice
1262 (see **Methods**). Significant shifts ($p<0.05$ from Cox regression analysis) annotated in red.
1263 Median hazard ratios plotted with error bars representing ± 1 quartile; “N”=number of mice;
1264 “HR”=hazard ratio; “CI”=confidence interval.

Supplemental Figure 2

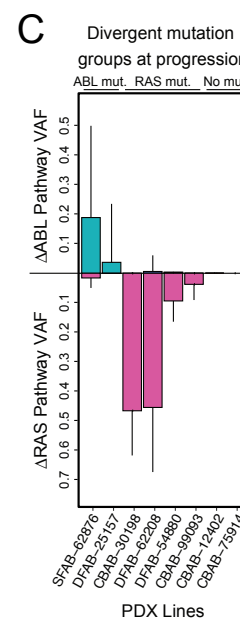
A



B



C



1266 **Figure S2. Emergent patterns in *BCR::ABL1* B-ALL mutation acquisition on TKI.**

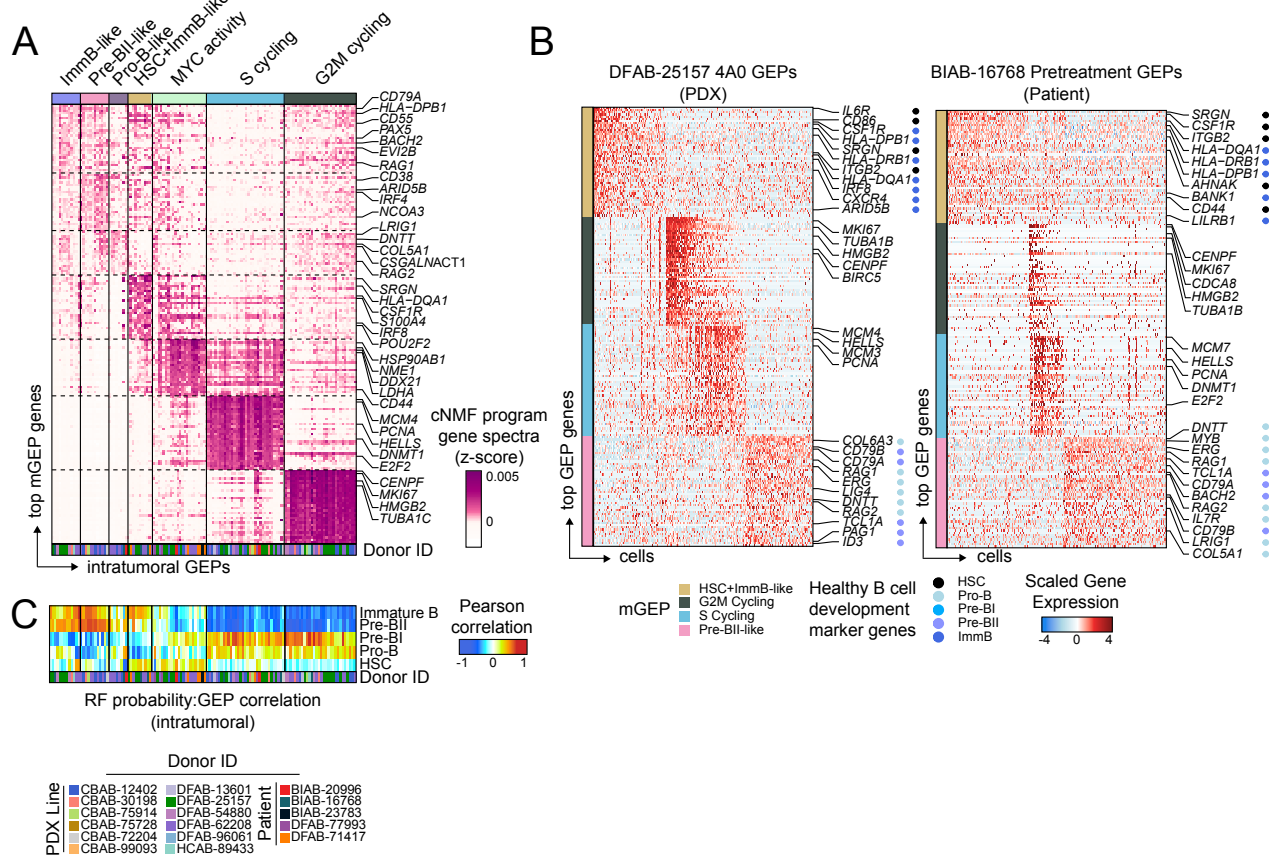
1267 *Related to Figure 1*

1268 **(A)** Mutational alterations of individual PDX mice on TKI therapeutic regimen, grouped by
1269 disease stage and annotated by treatment arm (“Tx Arm”). Treatment emergent mutations
1270 indicated when mice from the same PDX line were profiled at pretreatment. Summary of
1271 grouped RAS or ABL pathway mutations included below. Mice are annotated for prior TKI
1272 exposure. “MRD”=minimal residual disease; “TFs”=transcription factors. Alteration details
1273 additionally reported in **Table S3**.

1274 **(B)** Change in the fraction of mice on each Phase II-like trial treatment arm that harbor mutations
1275 between progression and pretreatment. Genes along the ABL and RAS pathways are
1276 annotated in turquoise and magenta, respectively.

1277 **(C)** Change in average VAF of PDX lines at progression for mutations along the ABL or RAS
1278 pathways compared to paired pretreatment tumors. Error bars indicate +1 standard deviation
1279 from the plotted mean Δ VAF.

Supplemental Figure 3



1281 **Figure S3. Intratumoral cNMF reveals developmentally convolved gene co-expression.**

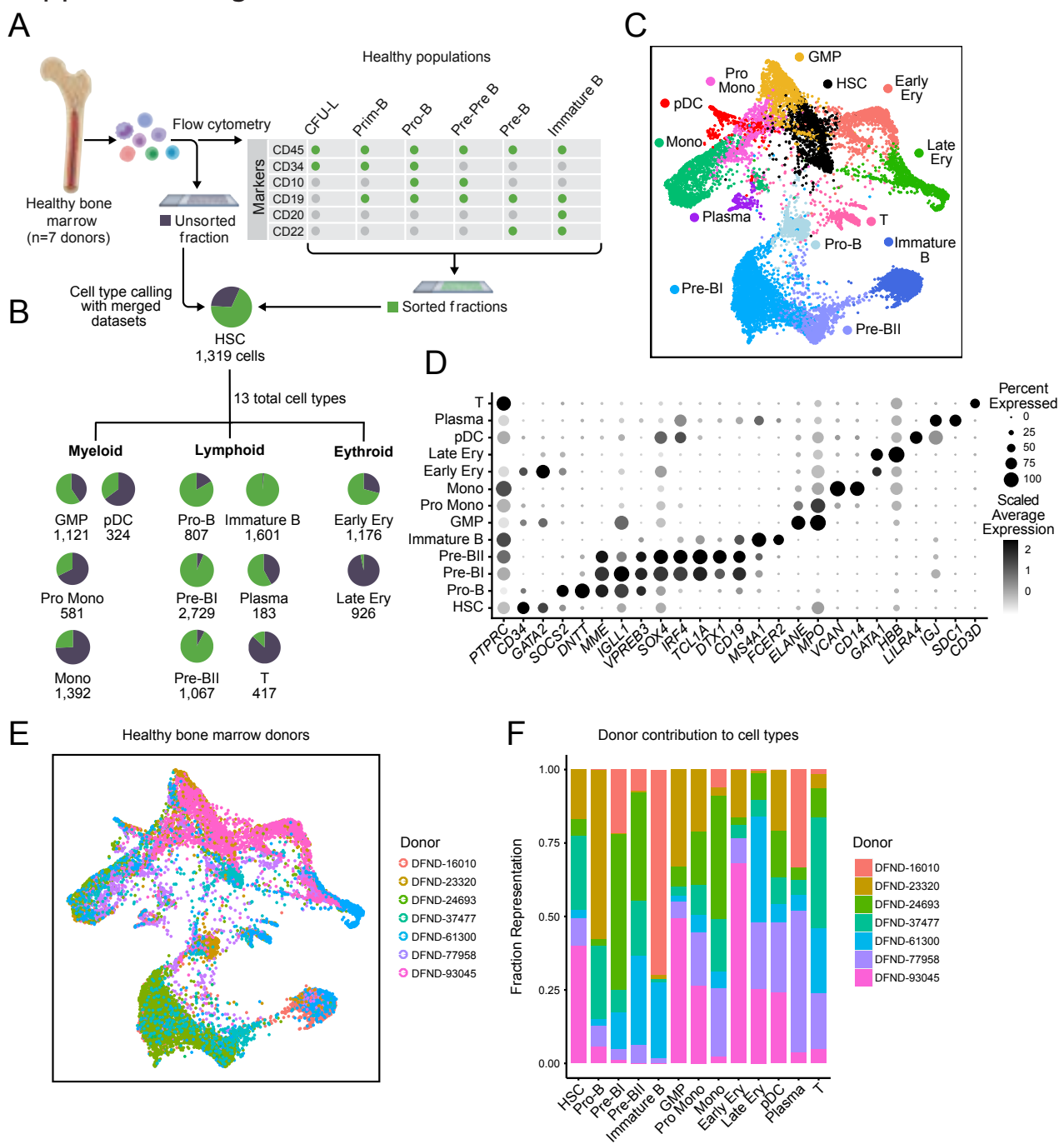
1282 *Related to Figure 2*

1283 **(A)** cNMF program z-scored gene spectra for the top 30 metaprogram (mGEP) genes across all
1284 intratumoral gene expression programs (GEPs; **Table S4**); individual GEPs are annotated
1285 by PDX or Patient ID to show mGEP consensus across multiple donors.

1286 **(B)** Representative heatmaps demonstrating intratumoral GEPs for one PDX tumor (DFAB-
1287 25157 4A0) and one patient tumor (BIAB-16768 Pretreatment). Known, healthy B cell lineage
1288 marker genes are annotated for each GEP.

1289 **(C)** Pearson correlation of GEP module score and random forest (RF) classification probabilities.
1290 Bottom color track indicates the donor where each individual GEP was identified.

Supplemental Figure 4



1292 **Figure S4. Generation of healthy human bone marrow scRNA-seq dataset.**

1293 *Related to Figure 2*

1294 **(A)** Healthy human bone marrow samples (n = 7) were flow sorted into live bulk, CFU-L (colony-
1295 forming unit low; progenitor), Prim-B, Pro-B, Pre-Pre-B, Pre-B, and Immature B populations
1296 for scRNA-seq profiling (see **Methods**).

1297 **(B)** Proportion of each cell type identified from the bulk (gray) or flow sorted-fraction (green).

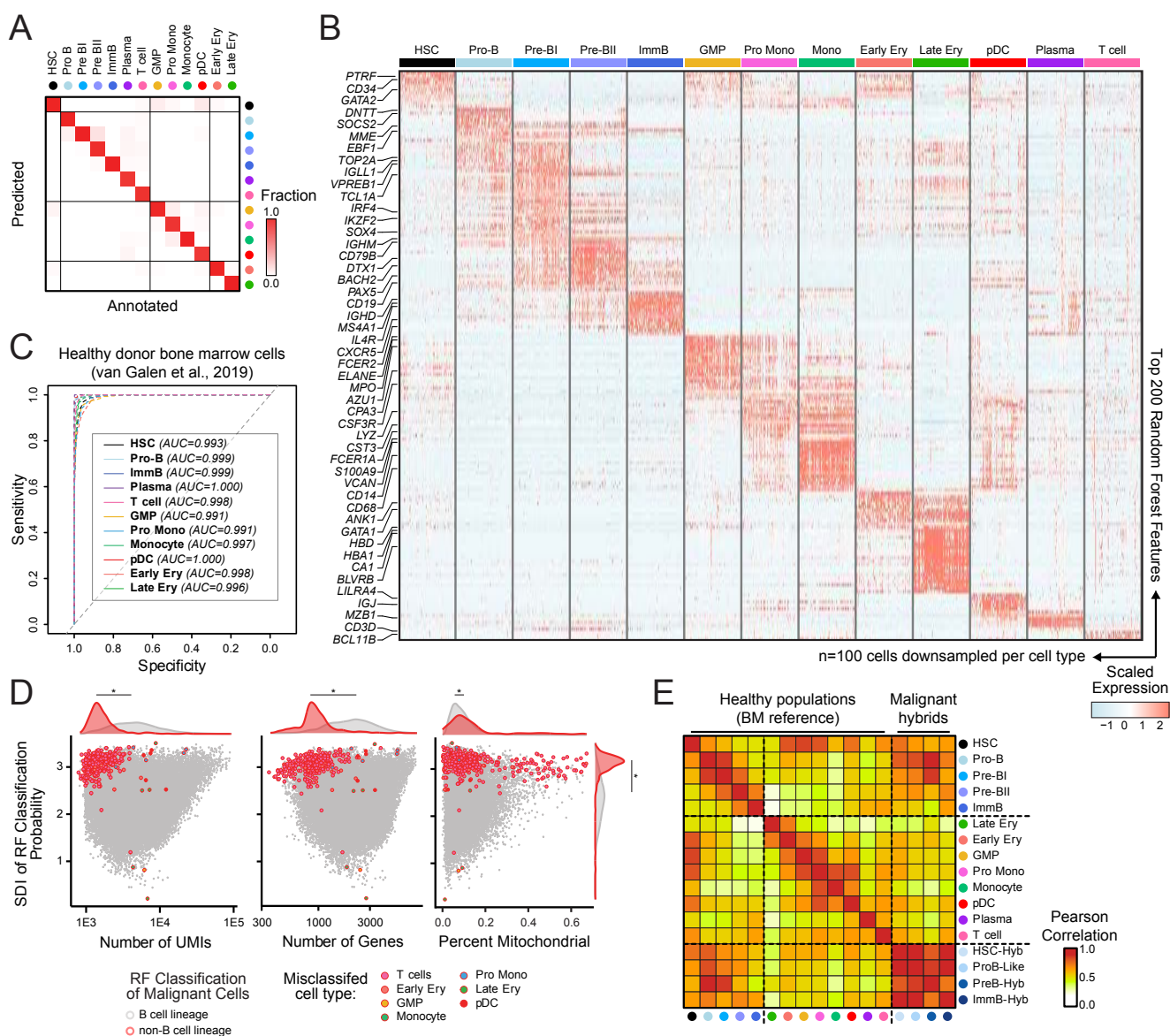
1298 **(C)** Force-directed graph (FDG) projection of healthy human bone marrow annotated by
1299 hematopoietic cell types (n=13,643 cells).

1300 **(D)** Dot plot of hematopoietic cell type marker genes. Color denotes scaled average expression;
1301 size denotes percent expression in each scRNA-seq cell type population.

1302 **(E)** FDG projection of healthy human bone marrow, annotated by donor.

1303 **(F)** Donor fractional contribution to each cell type population.

Supplemental Figure 5



1305 **Figure S5. Random Forest Classifier accurately classifies healthy and Ph+ ALL single-**
1306 **cell transcriptomes.**

1307 *Related to Figure 2*

1308 **(A)** 10-fold cross-validation of each healthy reference cell type during RF training.

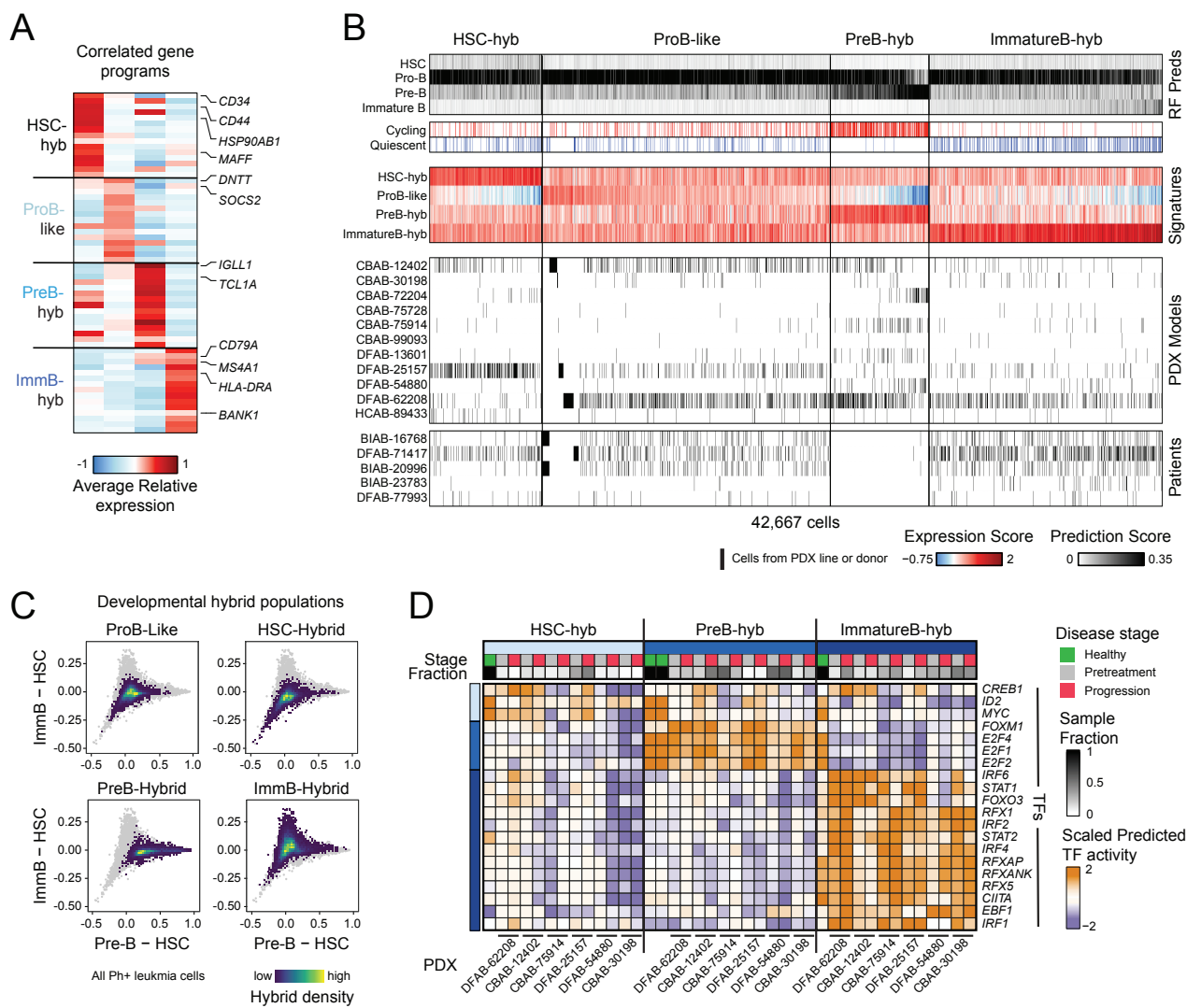
1309 **(B)** Top 200 RF features ranked by permuted feature importance, grouped by healthy reference
1310 cell type (randomly down-sampled n=100 cells).

1311 **(C)** Receiver Operating Characteristics (ROC) curves for RF classification of test scRNA-seq
1312 bone marrow dataset;¹⁶ area under the ROC curve (AUC) values listed in inset for each cell
1313 type.

1314 **(D)** Shannon Diversity Index (SDI) of classification probabilities versus number of unique
1315 molecular identifier (UMI), number of genes, and percent mitochondrial transcripts for all
1316 leukemic cells. Cells removed from analysis due to highest non-B cell lineage classification
1317 are outlined in red and colored by misclassified cell type. Significant shifts in distribution
1318 between non-B lineage and B-lineage single-cells, as defined by a Kolmogorov-Smirnov
1319 (KS) test, reported (* $p<0.001$).

1320 **(E)** Pearson correlation over gene expression of top 2,000 highly-variable genes from healthy
1321 reference dataset across healthy and malignant hybrid cell type subpopulations.

Supplemental Figure 6



1323 **Figure S6. Defining Ph+ ALL developmental tumor hybrid populations.**

1324 *Related to Figure 2*

1325 **(A)** Developmental hybrid signatures defined by the top 30 genes correlated to RF prediction
1326 scores for each normal B-lineage cell type (**Table S5**). Average expression of signature
1327 genes across leukemic hybrid populations.

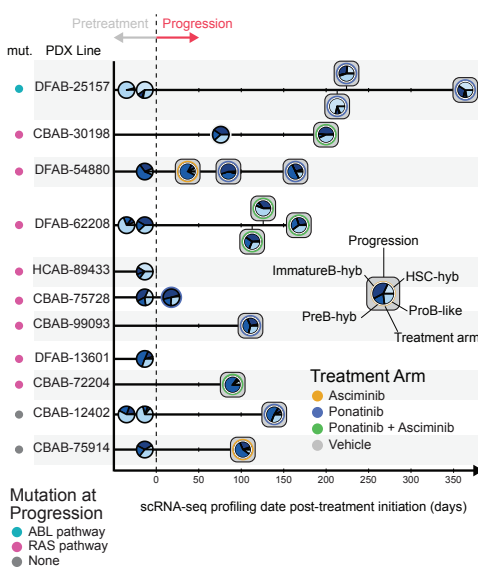
1328 **(B)** Classification of leukemic hybrid populations based on random forest (RF) classification
1329 probabilities and hybrid signatures (see **Methods**). RF prediction probabilities, cycling or
1330 quiescent status, and PDX line or Patient ID annotated for each cell.

1331 **(C)** Leukemic hybrid subpopulations projected onto RF prediction probability axes, as in **Figure**
1332 **2H**. Densities of leukemia cells from each hybrid population projected over the landscape of
1333 all leukemia cells in the scRNA-seq dataset (plotted in grey).

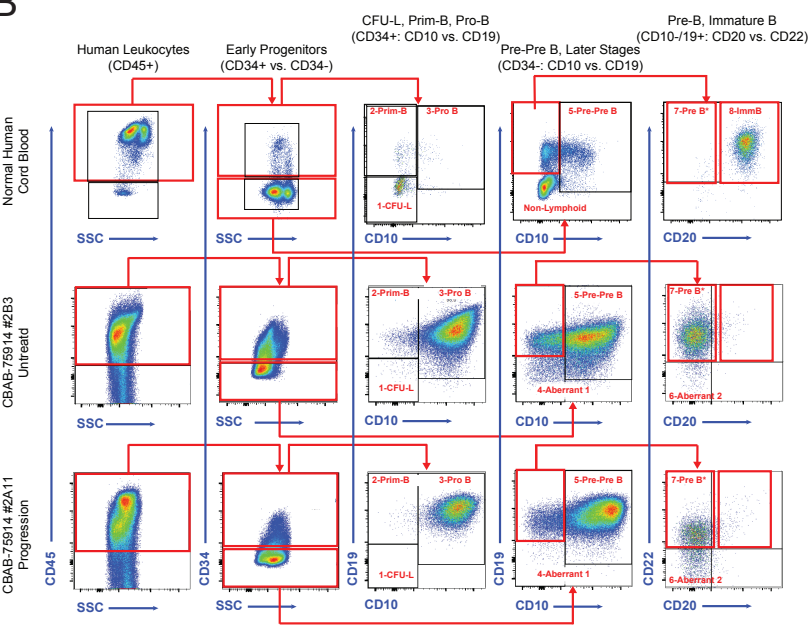
1334 **(D)** Scaled *in silico* predicted transcription factor (TF) activity over genes associated with
1335 developmental hybrid gene signatures (see **Methods**). Scaled TF activity scores shown in
1336 human reference samples (green) and PDX lines at pretreatment (grey) and progression
1337 (red), subset to TFs whose predicted activity scale with HSC, Pre-B, and Immature B RF
1338 classification probabilities in leukemic cells. Healthy reference Pre-BI and Pre-BII
1339 populations plotted independently within Pre-B.

Supplemental Figure 7

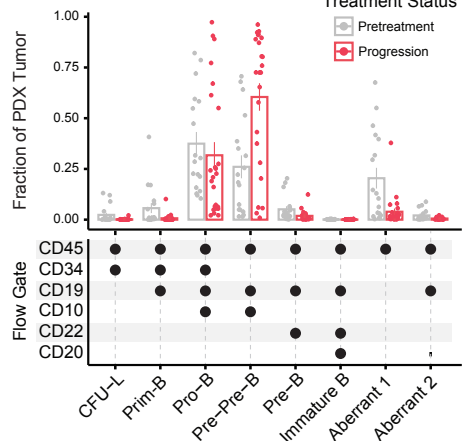
A



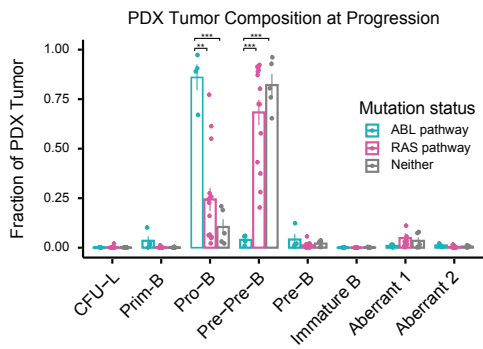
B



C



D



1341 **Figure S7. Transcriptional and immunophenotype shifts on therapy.**

1342 *Related to Figure 3*

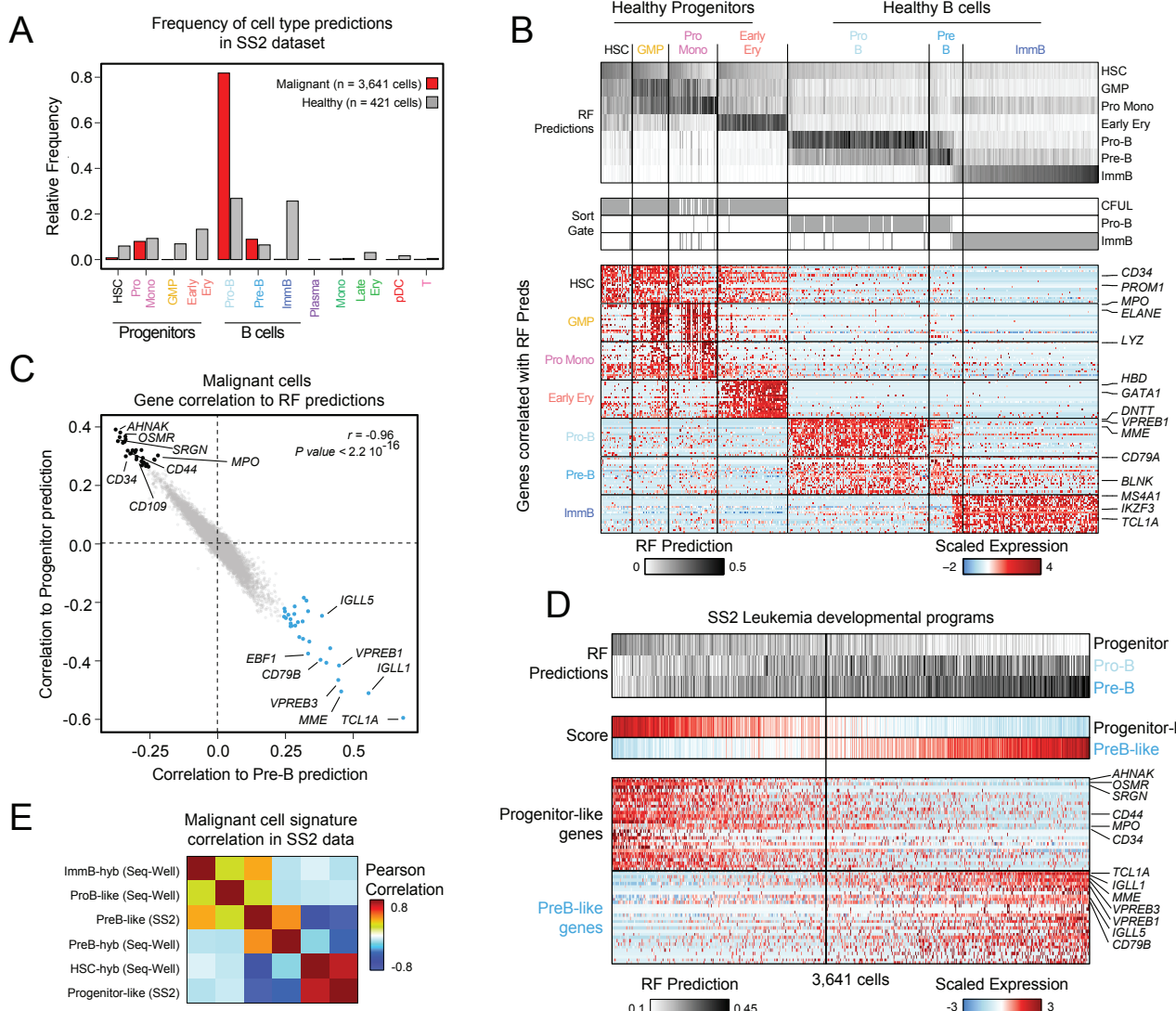
1343 **(A)** Hybrid scRNA-seq population distributions for each profiled pretreatment and progression
1344 PDX mouse, annotated by treatment arm and time on treatment.

1345 **(B)** Flow sorting gating strategy for B cell progenitor populations on a representative healthy
1346 human umbilical cord blood sample, PDX pre-treatment tumor, and PDX progression tumor
1347 (representative PDX=CBAB-75914).

1348 **(C)** Fraction representation of PDX pretreatment and progression tumors across
1349 immunophenotyped B cell progenitor-like populations. Individual tumor immunophenotyped
1350 population fractions plotted as points; bars represent average tumor fraction within each
1351 immunophenotyped population at pretreatment or progression time points, including error
1352 bars for ± 1 standard deviation. Surface markers used for flow gating of each population, as
1353 shown in **(B)**, annotated below.

1354 **(D)** Fraction of PDX tumor at progression of each immunophenotyped B cell progenitor-like
1355 population, grouped by mutation status at progression; bars represent average tumor
1356 fraction, with error bars for ± 1 standard deviation. Significant p-values from Dirichlet
1357 regression noted; ** $p<0.01$ and *** $p<0.001$.

Supplemental Figure 8



1359 **Figure S8. Random Forest (RF) Classifier recovers developmental structure in Smart-**
1360 **Seq2 single-cell transcriptomes.**

1361 *Related to Figure 4*

1362 **(A)** Proportion of RF cell type classifications across all Smart-Seq2 (SS2) healthy and leukemic
1363 cells.

1364 **(B)** Single-cells ordered by RF prediction probabilities from progenitor cell types to differentiated
1365 B cell types, and annotated by flow sort gate (as in **Figure S4A**). Below, scaled expression
1366 of the top 10 RF prediction-correlated genes in developmentally-ordered healthy cells.

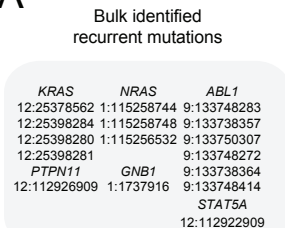
1367 **(C)** Genes correlated to Pre-B RF prediction (x-axis) and genes correlated to Progenitor RF
1368 prediction are negatively correlated with each other; rho and p-value from Pearson
1369 correlation noted. Colored points represent the top 30 progenitor and Pre-B correlated genes
1370 used to define the SS2 developmental spectrum.

1371 **(D)** Leukemic SS2 single-cells ranked by Progenitor-like score, annotated by B cell lineage RF
1372 prediction probabilities. Below, scaled expression of top 30 Progenitor-like and PreB-like
1373 signature genes (**Table S7**).

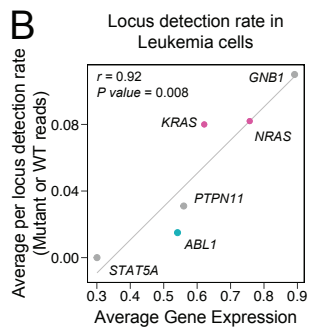
1374 **(E)** Pearson cross-correlation of RF cell type-correlated gene signature scores derived from Seq-
1375 Well and SS2 show cross-modality concordance. For clarity, SS2 signatures are hereafter
1376 referenced as “HSC-hyb” for Progenitor-like scores, and “PreB-hyb” for PreB-like scores.

Supplemental Figure 9

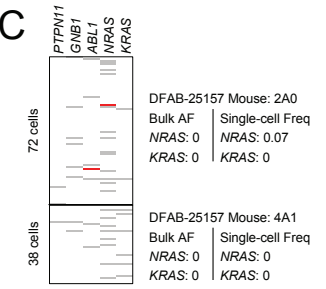
A



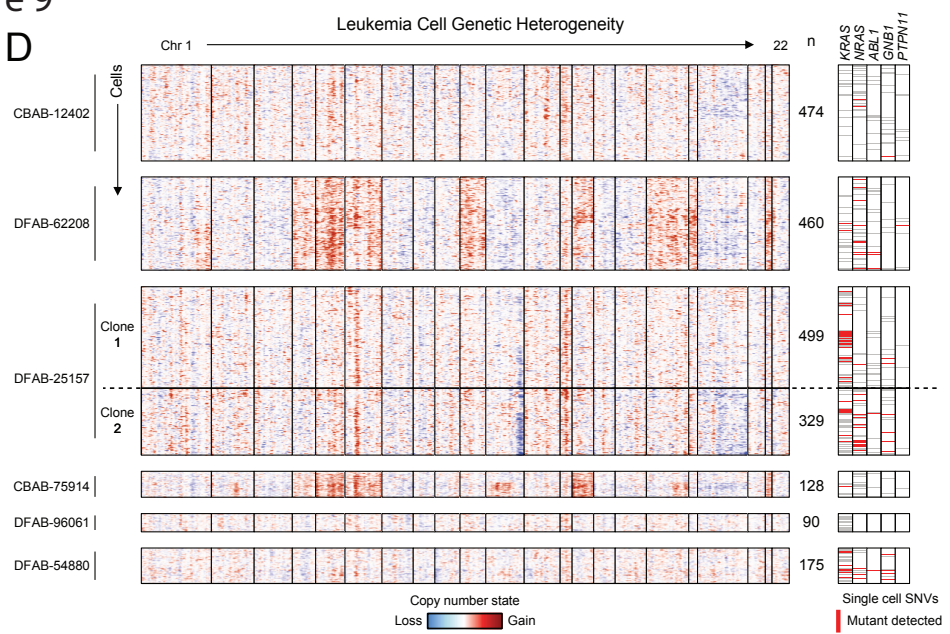
B



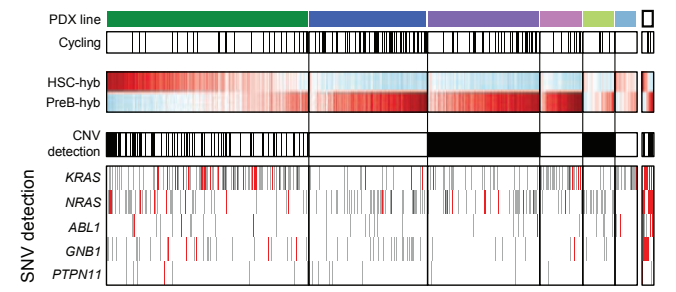
C



D



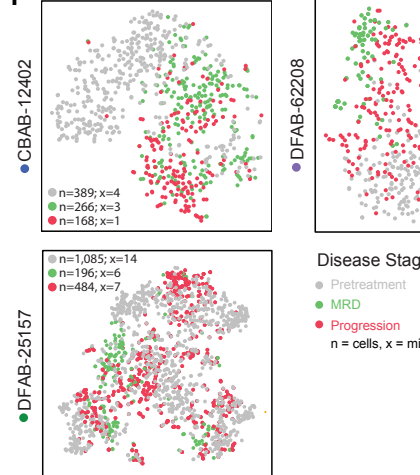
E



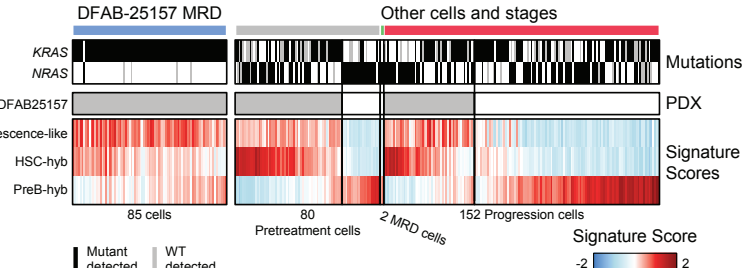
SNV detection

KRAS, NRAS, ABL1, GNB1, PTPN11

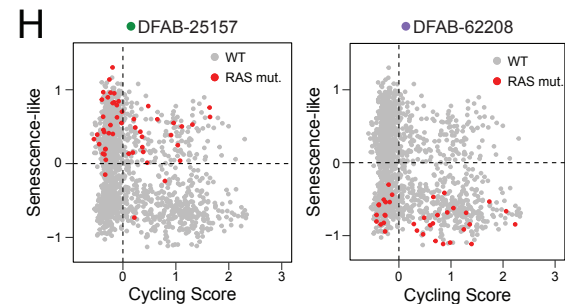
F



G



H



1378 **Figure S9. SS2 enables co-detection of mutations and transcriptome in leukemic single-**
1379 **cells.**

1380 *Related to Figure 4*

1381 **(A)** Summary of recurrently-identified RAS-pathway and ABL-pathway mutation loci from bulk
1382 targeted sequencing across PDX lines that were aligned for mutation detection in SS2
1383 FASTQs (see **Methods**; **Table S3**).

1384 **(B)** For genes with recurrently-identified mutations, Pearson correlation of average gene
1385 expression and normalized mutation-locus detection rate (either mutant or wild-type reads).

1386 **(C)** Mutant and wild-type transcripts detected in SS2 single-cell transcriptomes from three
1387 representative PDX tumors; detected mutant transcript frequency in single-cells matched
1388 bulk VAF.

1389 **(D)** Single-cell CNV profiles across each PDX line, including instances of CNV subclonal
1390 heterogeneity, paired with SS2-detected SNVs.

1391 **(E)** SS2 single-cells within each profiled PDX line ordered by HSC-hyb expression scores, as
1392 defined in **Figure S8D**. Cycling status, CNV detection, and detected mutant and wild-type
1393 transcripts are annotated. Co-mutant indicates single-cells where RAS and ABL pathway
1394 mutations were detected.

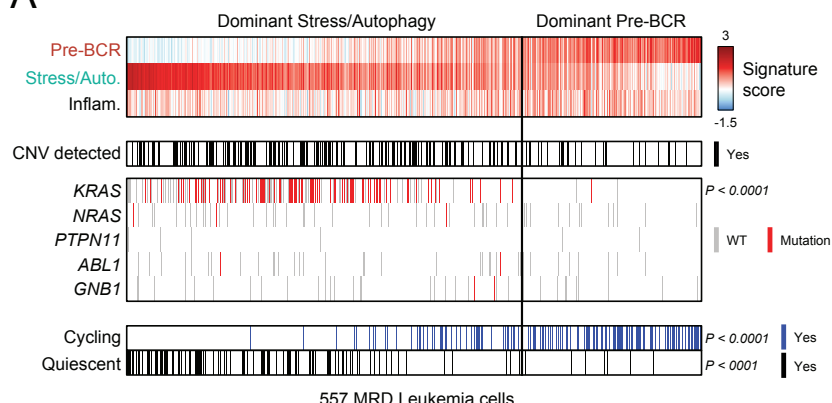
1395 **(F)** t-SNE projection of SS2 single-cells from representative PDX lines CBAB-12402, DFAB-
1396 62208, and DFAB-25157, colored by treatment time point. Number of SS2-profiled cells and
1397 mice at each time point denoted (n=cells, x=mice).

1398 **(G)** All RAS-pathway mutant leukemic single-cells grouped by three treatment timepoints,
1399 annotated by *KRAS* or *NRAS* mutant transcript detection, and ordered by HSC-hyb signature
1400 scores within SS2 single-cells from DFAB-25157 and non-DFAB-25157 PDX lines
1401 demonstrates association between senescence-like and HSC-hyb gene expression scores
1402 across PDX lines and treatment stages.

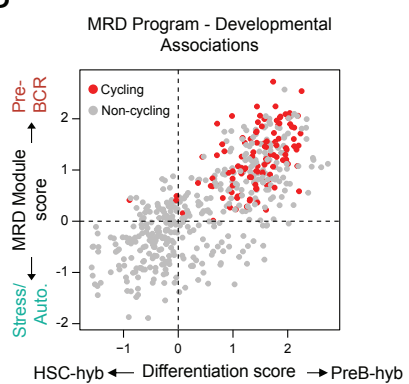
1403 **(H)** Cells from DFAB-25157 and DFAB-62208 at MRD and Progression, plot along fitness
1404 quadrants as defined in **Figure 4H**, with RAS-mutant leukemia cells annotated in red.

Supplemental Figure 10

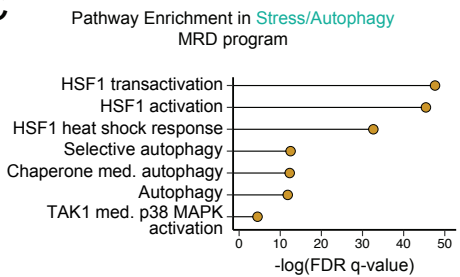
A



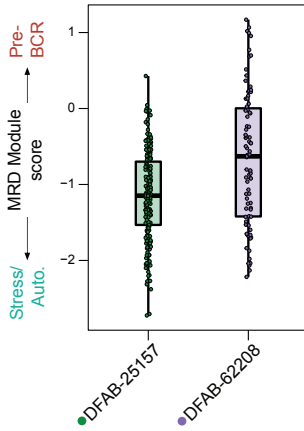
B



C



D



1406 **Figure S10. Targeting integrative cell states enhances remission.**

1407 *Related to Figure 5*

1408 **(A)** All MRD single-cells ordered by Pre-BCR Signaling MRD state scores. CNV and SNV
1409 mutation status annotated for each cell, along with cycling and quiescent status. *P*-values
1410 reported from Fisher exact test comparing abundance of *KRAS*-mutant, quiescent, and/or
1411 cycling MRD cells with dominant Stress/Autophagy (“Stress/Auto.”) expression scores to
1412 those with dominant Pre-BCR Signaling expression scores.

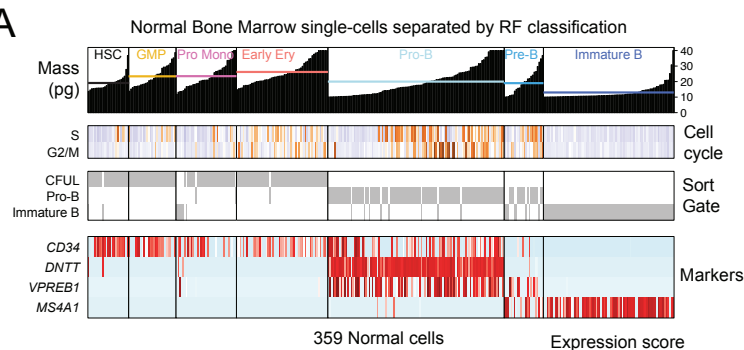
1413 **(B)** Correlation between Stress/Autophagy and HSC-hyb gene expression, versus Pre-BCR
1414 signaling and PreB-hyb gene expression. Cycling cells annotated in red.

1415 **(C)** Pathway enrichment false discovery rate (FDR) q-values for the top 100 genes in the
1416 Stress/Autophagy MRD state.

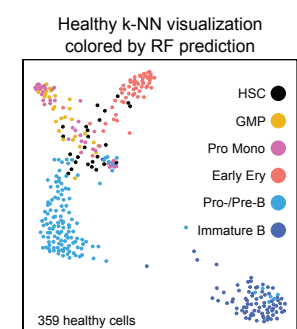
1417 **(D)** Boxplot of relative MRD program (Pre-BCR Signaling – Stress/Autophagy) in MRD cells from
1418 DFAB-25157 and DFAB-62208; single-cell scores from each PDX-line plotted as individual
1419 points.

Supplemental Figure 11

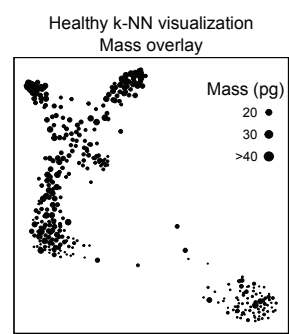
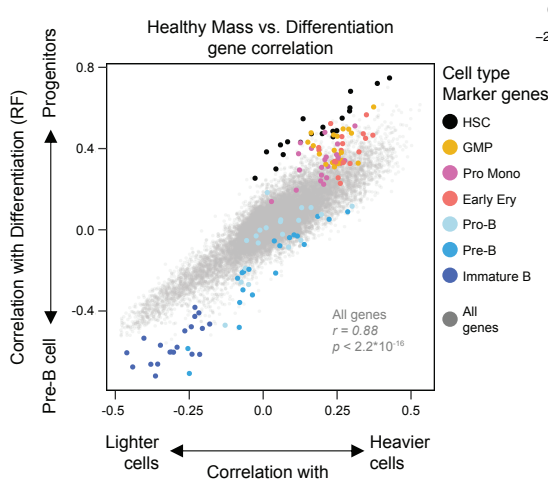
A



B



C



1421 **Figure S11. Mass correlates with developmental states and cell cycle.**

1422 *Related to Figure 6*

1423 **(A)** Mass of healthy reference SS2 cells, binned by random forest-classified cell type and
1424 annotated by cell-type marker gene expression. Mean mass for each cell type plotted as a
1425 line.

1426 **(B)** Force directed graph (FDG) visualization of healthy SS2 cells, annotated by cell type (top)
1427 and by cell mass (bottom); dot size indicates cell mass.

1428 **(C)** Mass-correlated genes in healthy SS2 cells on the x-axis, versus the difference between
1429 genes correlated with RF progenitor and Pre-B cell types in healthy SS2 cells on the y-axis.
1430 Colored points denote marker genes for each cell type. R and p-value denote Pearson
1431 correlation between x- and y-axis indicated gene correlations.

1432

1433 REFERENCES

- 1434 1. Byrgazov, K., Lucini, C.B., Valent, P., Hantschel, O., and Lion, T. (2018). BCR-ABL1
1435 compound mutants display differential and dose-dependent responses to ponatinib.
Haematologica 103, e10–e12. <https://doi.org/10.3324/haematol.2017.176347>.
- 1436 2. Soverini, S., De Benedittis, C., Papayannidis, C., Paolini, S., Venturi, C., Iacobucci, I., Luppi,
1437 M., Bresciani, P., Salvucci, M., Russo, D., et al. (2014). Drug resistance and BCR-ABL kinase
1438 domain mutations in Philadelphia chromosome–positive acute lymphoblastic leukemia from
1439 the imatinib to the second-generation tyrosine kinase inhibitor era: The main changes are in
1440 the type of mutations, but not in the frequency of mutation involvement. *Cancer* 120, 1002–
1441 1009. <https://doi.org/10.1002/cncr.28522>.
- 1442 3. Eide, C.A., Zabriskie, M.S., Savage Stevens, S.L., Antelope, O., Vellore, N.A., Than, H.,
1443 Schultz, A.R., Clair, P., Bowler, A.D., Pomicter, A.D., et al. (2019). Combining the Allosteric
1444 Inhibitor Asciminib with Ponatinib Suppresses Emergence of and Restores Efficacy against
1445 Highly Resistant BCR-ABL1 Mutants. *Cancer Cell* 36, 431–443.e5.
1446 <https://doi.org/10.1016/j.ccr.2019.08.004>.
- 1447 4. Bhang, H.C., Ruddy, D.A., Krishnamurthy Radhakrishna, V., Caushi, J.X., Zhao, R., Hims,
1448 M.M., Singh, A.P., Kao, I., Rakiec, D., Shaw, P., et al. (2015). Studying clonal dynamics in
1449 response to cancer therapy using high-complexity barcoding. *Nat Med* 21, 440–448.
1450 <https://doi.org/10.1038/nm.3841>.
- 1451 5. Hochhaus, A., Kreil, S., Corbin, A.S., La Rosée, P., Müller, M.C., Lahaye, T., Hanfstein, B.,
1452 Schoch, C., Cross, N.C.P., Berger, U., et al. (2002). Molecular and chromosomal mechanisms
1453 of resistance to imatinib (ST1571) therapy. *Leukemia* 16, 2190–2196.
1454 <https://doi.org/10.1038/sj.leu.2402741>.
- 1455 6. Good, Z., Sarno, J., Jager, A., Samusik, N., Aghaeepour, N., Simonds, E.F., White, L.,
1456 Lacayo, N.J., Fantl, W.J., Fazio, G., et al. (2018). Single-cell developmental classification of
1457 B cell precursor acute lymphoblastic leukemia at diagnosis reveals predictors of relapse. *Nat
1458 Med* 24, 474–483. <https://doi.org/10.1038/nm.4505>.
- 1459 7. Huang, X., Li, Y., Zhang, J., Yan, L., Zhao, H., Ding, L., Bhatara, S., Yang, X., Yoshimura, S.,
1460 Yang, W., et al. (2024). Single-cell systems pharmacology identifies development-driven drug
1461 response and combination therapy in B cell acute lymphoblastic leukemia. *Cancer Cell* 42,
1462 552–567.e6. <https://doi.org/10.1016/j.ccr.2024.03.003>.
- 1463 8. Kim, J.C., Chan-Seng-Yue, M., Ge, S., Zeng, A.G.X., Ng, K., Gan, O.I., Garcia-Prat, L., Flores-
1464 Figueroa, E., Woo, T., Zhang, A.X.W., et al. (2023). Transcriptomic classes of BCR-ABL1
1465 lymphoblastic leukemia. *Nat Genet* 55, 1186–1197. [https://doi.org/10.1038/s41588-023-01429-4](https://doi.org/10.1038/s41588-023-
1466 01429-4).
- 1467 9. Bastian, L., Beder, T., Barz, M.J., Bendig, S., Bartsch, L., Walter, W., Wolgast, N., Brändl, B.,
1468 Rohrandt, C., Hansen, B.-T., et al. (2024). Developmental trajectories and cooperating
1469 genomic events define molecular subtypes of BCR::ABL1-positive ALL. *Blood* 143, 1391–
1470 1398. <https://doi.org/10.1182/blood.2023021752>.
- 1471 10. Chan, L.N., Murakami, M.A., Robinson, M.E., Caeser, R., Sadras, T., Lee, J., Cosgun, K.N.,
1472 Kume, K., Khairnar, V., Xiao, G., et al. (2020). Signalling input from divergent pathways
1473 subverts B cell transformation. *Nature* 583, 845–851. [https://doi.org/10.1038/s41586-020-2513-4](https://doi.org/10.1038/s41586-020-
1474 2513-4).

1475 11. Ebinger, S., Özdemir, E.Z., Ziegenhain, C., Tiedt, S., Castro Alves, C., Grunert, M., Dworzak, M., Lutz, C., Turati, V.A., Enver, T., et al. (2016). Characterization of Rare, Dormant, and Therapy-Resistant Cells in Acute Lymphoblastic Leukemia. *Cancer Cell* 30, 849–862. <https://doi.org/10.1016/j.ccr.2016.11.002>.

1476 12. Hurtz, C., Wertheim, G.B., Loftus, J.P., Blumenthal, D., Lehman, A., Li, Y., Bagashev, A., Manning, B., Cummins, K.D., Burkhardt, J.K., et al. (2020). Oncogene-independent BCR-like signaling adaptation confers drug resistance in Ph-like ALL. *Journal of Clinical Investigation* 130, 3637–3653. <https://doi.org/10.1172/JCI134424>.

1477 13. Giustacchini, A., Thongjuea, S., Barkas, N., Woll, P.S., Povinelli, B.J., Booth, C.A.G., Sopp, P., Norfo, R., Rodriguez-Meira, A., Ashley, N., et al. (2017). Single-cell transcriptomics uncovers distinct molecular signatures of stem cells in chronic myeloid leukemia. *Nat Med* 23, 692–702. <https://doi.org/10.1038/nm.4336>.

1478 14. Eadie, L.N., Saunders, V.A., Branford, S., White, D.L., and Hughes, T.P. (2018). The new allosteric inhibitor asciminib is susceptible to resistance mediated by ABCB1 and ABCG2 overexpression in vitro. *Oncotarget* 9, 13423–13437. <https://doi.org/10.18632/oncotarget.24393>.

1483 15. Fennell, K.A., Vassiliadis, D., Lam, E.Y.N., Martelotto, L.G., Balic, J.J., Hollizeck, S., Weber, T.S., Semple, T., Wang, Q., Miles, D.C., et al. (2022). Non-genetic determinants of malignant clonal fitness at single-cell resolution. *Nature* 601, 125–131. <https://doi.org/10.1038/s41586-021-04206-7>.

1484 16. van Galen, P., Hovestadt, V., Wadsworth II, M.H., Hughes, T.K., Griffin, G.K., Battaglia, S., Verga, J.A., Stephansky, J., Pastika, T.J., Lombardi Story, J., et al. (2019). Single-Cell RNA-Seq Reveals AML Hierarchies Relevant to Disease Progression and Immunity. *Cell* 176, 1265–1281.e24. <https://doi.org/10.1016/j.cell.2019.01.031>.

1485 17. Velten, L., Story, B.A., Hernández-Malmierca, P., Raffel, S., Leonce, D.R., Milbank, J., Paulsen, M., Demir, A., Szu-Tu, C., Frömel, R., et al. (2021). Identification of leukemic and pre-leukemic stem cells by clonal tracking from single-cell transcriptomics. *Nat Commun* 12, 1366. <https://doi.org/10.1038/s41467-021-21650-1>.

1486 18. Nam, A.S., Kim, K.-T., Chaligne, R., Izzo, F., Ang, C., Taylor, J., Myers, R.M., Abu-Zeinah, G., Brand, R., Omans, N.D., et al. (2019). Somatic mutations and cell identity linked by Genotyping of Transcriptomes. *Nature* 571, 355–360. <https://doi.org/10.1038/s41586-019-1367-0>.

1487 19. Li, Q., Bohin, N., Wen, T., Ng, V., Magee, J., Chen, S.-C., Shannon, K., and Morrison, S.J. (2013). Oncogenic Nras has bimodal effects on stem cells that sustainably increase competitiveness. *Nature* 504, 143–147. <https://doi.org/10.1038/nature12830>.

1488 20. Robinson, T.M., Bowman, R.L., Persaud, S., Liu, Y., Neigenfind, R., Gao, Q., Zhang, J., Sun, X., Miles, L.A., Cai, S.F., et al. (2023). Single-cell genotypic and phenotypic analysis of measurable residual disease in acute myeloid leukemia. *Sci Adv* 9, eadg0488. <https://doi.org/10.1126/sciadv.adg0488>.

1489 21. Luskin, M.R., Murakami, M.A., Manalis, S.R., and Weinstock, D.M. (2018). Targeting minimal residual disease: a path to cure? *Nat Rev Cancer* 18, 255–263. <https://doi.org/10.1038/nrc.2017.125>.

1517 22. Tettero, J.M., Ngai, L.L., Bachas, C., Breems, D.A., Fischer, T., Gjertsen, B.T., Gradowska,
1518 P., Griskevicius, L., Janssen, J.J.W.M., Juliussen, G., et al. (2023). Measurable residual
1519 disease-guided therapy in intermediate-risk acute myeloid leukemia patients is a valuable
1520 strategy in reducing allogeneic transplantation without negatively affecting survival.
1521 *Haematologica* 108, 2794–2798. <https://doi.org/10.3324/haematol.2022.282639>.

1522 23. Dekker, S.E., Rea, D., Cayuela, J.-M., Arnhardt, I., Leonard, J., and Heuser, M. (2023). Using
1523 Measurable Residual Disease to Optimize Management of AML, ALL, and Chronic Myeloid
1524 Leukemia. *Am Soc Clin Oncol Educ Book* 43, e390010.
1525 https://doi.org/10.1200/EDBK_390010.

1526 24. Wieduwilt, M.J. (2022). Ph+ ALL in 2022: is there an optimal approach? *Hematology Am Soc
1527 Hematol Educ Program* 2022, 206–212. <https://doi.org/10.1182/hematology.2022000338>.

1528 25. Agudo, J., Aguirre-Ghiso, J.A., Bhatia, M., Chodosh, L.A., Correia, A.L., and Klein, C.A.
1529 (2024). Targeting cancer cell dormancy. *Nat Rev Cancer* 24, 97–104.
1530 <https://doi.org/10.1038/s41568-023-00642-x>.

1531 26. Wylie, A.A., Schoepfer, J., Jahnke, W., Cowan-Jacob, S.W., Loo, A., Furet, P., Marzinzik,
1532 A.L., Pelle, X., Donovan, J., Zhu, W., et al. (2017). The allosteric inhibitor ABL001 enables
1533 dual targeting of BCR-ABL1. *Nature* 543, 733–737. <https://doi.org/10.1038/nature21702>.

1534 27. Townsend, E.C., Murakami, M.A., Christodoulou, A., Christie, A.L., Köster, J., DeSouza,
1535 T.A., Morgan, E.A., Kallgren, S.P., Liu, H., Wu, S.-C., et al. (2016). The Public Repository of
1536 Xenografts Enables Discovery and Randomized Phase II-like Trials in Mice. *Cancer Cell* 29,
1537 574–586. <https://doi.org/10.1016/j.ccr.2016.03.008>.

1538 28. Gökbüget, N., Stanze, D., Beck, J., Diedrich, H., Horst, H.-A., Hüttmann, A., Kobbe, G.,
1539 Kreuzer, K.-A., Leimer, L., Reichle, A., et al. (2012). Outcome of relapsed adult lymphoblastic
1540 leukemia depends on response to salvage chemotherapy, prognostic factors, and
1541 performance of stem cell transplantation. *Blood* 120, 2032–2041.
1542 <https://doi.org/10.1182/blood-2011-12-399287>.

1543 29. Martinelli, G., Iacobucci, I., Storlazzi, C.T., Vignetti, M., Paoloni, F., Cilloni, D., Soverini, S.,
1544 Vitale, A., Chiaretti, S., Cimino, G., et al. (2009). IKZF1 (Ikaros) deletions in BCR-ABL1-
1545 positive acute lymphoblastic leukemia are associated with short disease-free survival and high
1546 rate of cumulative incidence of relapse: a GIMEMA AL WP report. *J Clin Oncol* 27, 5202–
1547 5207. <https://doi.org/10.1200/JCO.2008.21.6408>.

1548 30. Pfeifer, H., Wassmann, B., Pavlova, A., Wunderle, L., Oldenburg, J., Binckebanck, A.,
1549 Lange, T., Hochhaus, A., Wystub, S., Brück, P., et al. (2007). Kinase domain mutations of
1550 BCR-ABL frequently precede imatinib-based therapy and give rise to relapse in patients with
1551 de novo Philadelphia-positive acute lymphoblastic leukemia (Ph+ ALL). *Blood* 110, 727–734.
1552 <https://doi.org/10.1182/blood-2006-11-052373>.

1553 31. Hughes, T.K., Wadsworth, M.H., Gierahn, T.M., Do, T., Weiss, D., Andrade, P.R., Ma, F., de
1554 Andrade Silva, B.J., Shao, S., Tsoi, L.C., et al. (2020). Second-Strand Synthesis-Based
1555 Massively Parallel scRNA-Seq Reveals Cellular States and Molecular Features of Human
1556 Inflammatory Skin Pathologies. *Immunity* 53, 878–894.e7.
1557 <https://doi.org/10.1016/j.jimmuni.2020.09.015>.

1558 32. Baccin, C., Al-Sabah, J., Velten, L., Helbling, P.M., Grünschläger, F., Hernández-Malmierca,
1559 P., Nombela-Arrieta, C., Steinmetz, L.M., Trumpp, A., and Haas, S. (2020). Combined single-

1560 cell and spatial transcriptomics reveal the molecular, cellular and spatial bone marrow niche
1561 organization. *Nat Cell Biol* 22, 38–48. <https://doi.org/10.1038/s41556-019-0439-6>.

1562 33. Slobodnyuk, K., Radic, N., Ivanova, S., Llado, A., Tremolec, N., Zorzano, A., and Nebreda,
1563 A.R. (2019). Autophagy-induced senescence is regulated by p38 α signaling. *Cell Death Dis*
1564 10, 376. <https://doi.org/10.1038/s41419-019-1607-0>.

1565 34. Naka, K., Jomen, Y., Ishihara, K., Kim, J., Ishimoto, T., Bae, E.-J., Mohney, R.P., Stirdvant,
1566 S.M., Oshima, H., Oshima, M., et al. (2015). Dipeptide species regulate p38MAPK-Smad3
1567 signalling to maintain chronic myelogenous leukaemia stem cells. *Nat Commun* 6, 8039.
1568 <https://doi.org/10.1038/ncomms9039>.

1569 35. Sui, X., Kong, N., Ye, L., Han, W., Zhou, J., Zhang, Q., He, C., and Pan, H. (2014). p38 and
1570 JNK MAPK pathways control the balance of apoptosis and autophagy in response to
1571 chemotherapeutic agents. *Cancer Lett* 344, 174–179.
1572 <https://doi.org/10.1016/j.canlet.2013.11.019>.

1573 36. Naeim, F., Song, S.X., Rao, P.N., and Phan, R.T. (2018). *Atlas of Hematopathology: Morphology, Immunophenotype, Cytogenetics, and Molecular Approaches* 2nd ed. (Elsevier, Inc.).

1574 37. Burg, T.P., Godin, M., Knudsen, S.M., Shen, W., Carlson, G., Foster, J.S., Babcock, K., and
1575 Manalis, S.R. (2007). Weighing of biomolecules, single cells and single nanoparticles in fluid. *Nature* 446, 1066–1069. <https://doi.org/10.1038/nature05741>.

1576 38. Feijó Delgado, F., Cermak, N., Hecht, V.C., Son, S., Li, Y., Knudsen, S.M., Olcum, S.,
1577 Higgins, J.M., Chen, J., Grover, W.H., et al. (2013). Intracellular water exchange for measuring
1578 the dry mass, water mass and changes in chemical composition of living cells. *PLoS One* 8, e67590. <https://doi.org/10.1371/journal.pone.0067590>.

1579 39. Hecht, V.C., Sullivan, L.B., Kimmerling, R.J., Kim, D.-H., Hosios, A.M., Stockslager, M.A.,
1580 Stevens, M.M., Kang, J.H., Wirtz, D., Vander Heiden, M.G., et al. (2016). Biophysical changes
1581 reduce energetic demand in growth factor-deprived lymphocytes. *J Cell Biol* 212, 439–447.
1582 <https://doi.org/10.1083/jcb.201506118>.

1583 40. Cermak, N., Olcum, S., Delgado, F.F., Wasserman, S.C., Payer, K.R., A Murakami, M.,
1584 Knudsen, S.M., Kimmerling, R.J., Stevens, M.M., Kikuchi, Y., et al. (2016). High-throughput
1585 measurement of single-cell growth rates using serial microfluidic mass sensor arrays. *Nat Biotechnol* 34, 1052–1059. <https://doi.org/10.1038/nbt.3666>.

1586 41. Kimmerling, R.J., Prakadan, S.M., Gupta, A.J., Calistri, N.L., Stevens, M.M., Olcum, S.,
1587 Cermak, N., Drake, R.S., Pelton, K., De Smet, F., et al. (2018). Linking single-cell
1588 measurements of mass, growth rate, and gene expression. *Genome Biology* 19, 207.
1589 <https://doi.org/10.1186/s13059-018-1576-0>.

1590 42. Neurohr, G.E., Terry, R.L., Lengefeld, J., Bonney, M., Brittingham, G.P., Moretto, F.,
1591 Miettinen, T.P., Vaites, L.P., Soares, L.M., Paulo, J.A., et al. (2019). Excessive Cell Growth
1592 Causes Cytoplasm Dilution And Contributes to Senescence. *Cell* 176, 1083-1097.e18.
1593 <https://doi.org/10.1016/j.cell.2019.01.018>.

1594 43. Son, S., Tzur, A., Weng, Y., Jorgensen, P., Kim, J., Kirschner, M.W., and Manalis, S.R.
1595 (2012). Direct observation of mammalian cell growth and size regulation. *Nat Methods* 9, 910–
1596 912. <https://doi.org/10.1038/nmeth.2133>.

1597 1598 1599 1600 1601

1602 44. Miettinen, T.P., Kang, J.H., Yang, L.F., and Manalis, S.R. (2019). Mammalian cell growth
1603 dynamics in mitosis. *Elife* 8, e44700. <https://doi.org/10.7554/elife.44700>.

1604 45. Marquart, J., Chen, E.Y., and Prasad, V. (2018). Estimation of the Percentage of US Patients
1605 With Cancer Who Benefit From Genome-Driven Oncology. *JAMA Oncol* 4, 1093–1098.
1606 <https://doi.org/10.1001/jamaoncol.2018.1660>.

1607 46. Letai, A. (2017). Functional precision cancer medicine—moving beyond pure genomics. *Nat
1608 Med* 23, 1028–1035. <https://doi.org/10.1038/nm.4389>.

1609 47. Letai, A., Bhola, P., and Welm, A.L. (2022). Functional precision oncology: Testing tumors
1610 with drugs to identify vulnerabilities and novel combinations. *Cancer Cell* 40, 26–35.
1611 <https://doi.org/10.1016/j.ccr.2021.12.004>.

1612 48. Braun, T.P., Eide, C.A., and Druker, B.J. (2020). Response and Resistance to BCR-ABL1-
1613 Targeted Therapies. *Cancer Cell* 37, 530–542. <https://doi.org/10.1016/j.ccr.2020.03.006>.

1614 49. Boumahdi, S., and de Sauvage, F.J. (2020). The great escape: tumour cell plasticity in
1615 resistance to targeted therapy. *Nat Rev Drug Discov* 19, 39–56.
1616 <https://doi.org/10.1038/s41573-019-0044-1>.

1617 50. Duy, C., Li, M., Teater, M., Meydan, C., Garrett-Bakelman, F.E., Lee, T.C., Chin, C.R.,
1618 Durmaz, C., Kawabata, K.C., Dhimolea, E., et al. (2021). Chemotherapy Induces
1619 Senescence-Like Resilient Cells Capable of Initiating AML Recurrence. *Cancer Discov* 11,
1620 1542–1561. <https://doi.org/10.1158/2159-8290.CD-20-1375>.

1621 51. Aggarwal, R., Huang, J., Alumkal, J.J., Zhang, L., Feng, F.Y., Thomas, G.V., Weinstein, A.S.,
1622 Friedl, V., Zhang, C., Witte, O.N., et al. (2018). Clinical and Genomic Characterization of
1623 Treatment-Emergent Small-Cell Neuroendocrine Prostate Cancer: A Multi-institutional
1624 Prospective Study. *JCO* 36, 2492–2503. <https://doi.org/10.1200/JCO.2017.77.6880>.

1625 52. Uruga, H., Fujii, T., Nakamura, N., Moriguchi, S., Kishi, K., and Takaya, H. (2020). Squamous
1626 cell transformation as a mechanism of acquired resistance to tyrosine kinase inhibitor in
1627 EGFR-mutated lung adenocarcinoma: a report of two cases. *Respirology Case Reports* 8,
1628 e00521. <https://doi.org/10.1002/rcr2.521>.

1629 53. Sequist, L.V., Waltman, B.A., Dias-Santagata, D., Digumarthy, S., Turke, A.B., Fidias, P.,
1630 Bergethon, K., Shaw, A.T., Gettinger, S., Cosper, A.K., et al. (2011). Genotypic and
1631 Histological Evolution of Lung Cancers Acquiring Resistance to EGFR Inhibitors. *Science
1632 Translational Medicine* 3, 75ra26-75ra26. <https://doi.org/10.1126/scitranslmed.3002003>.

1633 54. Wang, Y.-C., Morrison, G., Gillihan, R., Guo, J., Ward, R.M., Fu, X., Botero, M.F., Healy,
1634 N.A., Hilsenbeck, S.G., Phillips, G.L., et al. (2011). Different mechanisms for resistance to
1635 trastuzumab versus lapatinib in HER2-positive breast cancers--role of estrogen receptor and
1636 HER2 reactivation. *Breast Cancer Res* 13, R121. <https://doi.org/10.1186/bcr3067>.

1637 55. Luskin, M.R., Murakami, M.A., Keating, J., Winer, E.S., Garcia, J.S., Stahl, M., Wadleigh,
1638 M., Flamand, Y., Neuberg, D.S., Galinsky, I., et al. (2023). A Phase I Study of Asciminib
1639 (ABL001) in Combination with Dasatinib and Prednisone for BCR-ABL1-Positive ALL and
1640 Blast Phase CML in Adults. *Blood* 142, 965. <https://doi.org/10.1182/blood-2023-174246>.

1641 56. Keating, A.K., Gossai, N., Phillips, C.L., Maloney, K., Campbell, K., Doan, A., Bhojwani, D.,
1642 Burke, M.J., and Verneris, M.R. (2019). Reducing minimal residual disease with

1643 blinatumomab prior to HCT for pediatric patients with acute lymphoblastic leukemia. *Blood*
1644 *Advances* 3, 1926–1929. <https://doi.org/10.1182/bloodadvances.2018025726>.

1645 57. Gökbuget, N., Zugmaier, G., Dombret, H., Stein, A., Bonifacio, M., Graux, C., Faul, C.,
1646 Brüggemann, M., Taylor, K., Mergen, N., et al. (2020). Curative outcomes following
1647 blinatumomab in adults with minimal residual disease B-cell precursor acute lymphoblastic
1648 leukemia. *Leukemia & Lymphoma* 61, 2665–2673.
1649 <https://doi.org/10.1080/10428194.2020.1780583>.

1650 58. Salek, M., Li, N., Chou, H.-P., Saini, K., Jovic, A., Jacobs, K.B., Johnson, C., Lu, V., Lee,
1651 E.J., Chang, C., et al. (2023). COSMOS: a platform for real-time morphology-based, label-
1652 free cell sorting using deep learning. *Commun Biol* 6, 971. <https://doi.org/10.1038/s42003-023-05325-9>.

1653 59. Chan, J.M., Zaidi, S., Love, J.R., Zhao, J.L., Setty, M., Wadosky, K.M., Gopalan, A., Choo,
1654 Z.-N., Persad, S., Choi, J., et al. (2022). Lineage plasticity in prostate cancer depends on
1655 JAK/STAT inflammatory signaling. *Science* 377, 1180–1191.
1656 <https://doi.org/10.1126/science.abn0478>.

1657 60. Raghavan, S., Winter, P.S., Navia, A.W., Williams, H.L., DenAdel, A., Lowder, K.E., Galvez-
1658 Reyes, J., Kalekar, R.L., Mulugeta, N., Kapner, K.S., et al. (2021). Microenvironment drives
1659 cell state, plasticity, and drug response in pancreatic cancer. *Cell* 184, 6119–6137.e26.
1660 <https://doi.org/10.1016/j.cell.2021.11.017>.

1661 61. Rambow, F., Rogiers, A., Marin-Bejar, O., Aibar, S., Femel, J., Dewaele, M., Karras, P.,
1662 Brown, D., Chang, Y.H., Debiec-Rychter, M., et al. (2018). Toward Minimal Residual Disease-
1663 Directed Therapy in Melanoma. *Cell* 174, 843–855.e19.
1664 <https://doi.org/10.1016/j.cell.2018.06.025>.

1665 62. Hahn, W.C., Bader, J.S., Braun, T.P., Califano, A., Clemons, P.A., Druker, B.J., Ewald, A.J.,
1666 Fu, H., Jagu, S., Kemp, C.J., et al. (2021). An expanded universe of cancer targets. *Cell* 184,
1667 1142–1155. <https://doi.org/10.1016/j.cell.2021.02.020>.

1668 63. Odejide, O., Weigert, O., Lane, A.A., Toscano, D., Lunning, M.A., Kopp, N., Kim, S., van
1669 Bodegom, D., Bolla, S., Schatz, J.H., et al. (2014). A targeted mutational landscape of
1670 angioimmunoblastic T-cell lymphoma. *Blood* 123, 1293–1296. <https://doi.org/10.1182/blood-2013-10-531509>.

1671 64. Kluk, M.J., Lindsley, R.C., Aster, J.C., Lindeman, N.I., Szeto, D., Hall, D., and Kuo, F.C.
1672 (2016). Validation and Implementation of a Custom Next-Generation Sequencing Clinical
1673 Assay for Hematologic Malignancies. *The Journal of Molecular Diagnostics* 18, 507–515.
1674 <https://doi.org/10.1016/j.jmoldx.2016.02.003>.

1675 65. Stockslager, M.A., Malinowski, S., Touat, M., Yoon, J.C., Geduldig, J., Mirza, M., Kim, A.S.,
1676 Wen, P.Y., Chow, K.-H., Ligon, K.L., et al. (2021). Functional drug susceptibility testing using
1677 single-cell mass predicts treatment outcome in patient-derived cancer neurosphere models.
1678 *Cell Reports* 37, 109788. <https://doi.org/10.1016/j.celrep.2021.109788>.

1679 66. Trombetta, J.J., Gennert, D., Lu, D., Satija, R., Shalek, A.K., and Regev, A. (2014).
1680 Preparation of Single-Cell RNA-Seq Libraries for Next Generation Sequencing. *Current
1681 Protocols in Molecular Biology* 107, 4.22.1–4.22.17.
1682 <https://doi.org/10.1002/0471142727.mb0422s107>.

1683 67. Therneau, T. (2024). A Package for Survival Analysis in R.

1684

1686 68. Li, H., and Durbin, R. (2009). Fast and accurate short read alignment with Burrows–Wheeler
1687 transform. *Bioinformatics* 25, 1754–1760. <https://doi.org/10.1093/bioinformatics/btp324>.

1688 69. McKenna, A., Hanna, M., Banks, E., Sivachenko, A., Cibulskis, K., Kernytsky, A., Garimella,
1689 K., Altshuler, D., Gabriel, S., Daly, M., et al. (2010). The Genome Analysis Toolkit: A
1690 MapReduce framework for analyzing next-generation DNA sequencing data. *Genome Res.*
1691 20, 1297–1303. <https://doi.org/10.1101/gr.107524.110>.

1692 70. DePristo, M.A., Banks, E., Poplin, R., Garimella, K.V., Maguire, J.R., Hartl, C., Philippakis,
1693 A.A., del Angel, G., Rivas, M.A., Hanna, M., et al. (2011). A framework for variation discovery
1694 and genotyping using next-generation DNA sequencing data. *Nat Genet* 43, 491–498.
1695 <https://doi.org/10.1038/ng.806>.

1696 71. Cibulskis, K., Lawrence, M.S., Carter, S.L., Sivachenko, A., Jaffe, D., Sougnez, C., Gabriel,
1697 S., Meyerson, M., Lander, E.S., and Getz, G. (2013). Sensitive detection of somatic point
1698 mutations in impure and heterogeneous cancer samples. *Nat Biotechnol* 31, 213–219.
1699 <https://doi.org/10.1038/nbt.2514>.

1700 72. McLaren, W., Pritchard, B., Rios, D., Chen, Y., Flieck, P., and Cunningham, F. (2010).
1701 Deriving the consequences of genomic variants with the Ensembl API and SNP Effect
1702 Predictor. *Bioinformatics* 26, 2069–2070. <https://doi.org/10.1093/bioinformatics/btq330>.

1703 73. Bi, W.L., Greenwald, N.F., Ramkissoon, S.H., Abedalthagafi, M., Coy, S.M., Ligon, K.L., Mei,
1704 Y., MacConaill, L., Ducar, M., Min, L., et al. (2017). Clinical Identification of Oncogenic Drivers
1705 and Copy-Number Alterations in Pituitary Tumors. *Endocrinology* 158, 2284–2291.
1706 <https://doi.org/10.1210/en.2016-1967>.

1707 74. Li, B., Gould, J., Yang, Y., Sarkizova, S., Tabaka, M., Ashenberg, O., Rosen, Y., Slyper, M.,
1708 Kowalczyk, M.S., Villani, A.-C., et al. (2020). Cumulus provides cloud-based data analysis for
1709 large-scale single-cell and single-nucleus RNA-seq. *Nat Methods* 17, 793–798.
1710 <https://doi.org/10.1038/s41592-020-0905-x>.

1711 75. Butler, A., Hoffman, P., Smibert, P., Papalexi, E., and Satija, R. (2018). Integrating single-
1712 cell transcriptomic data across different conditions, technologies, and species. *Nat Biotechnol*
1713 36, 411–420. <https://doi.org/10.1038/nbt.4096>.

1714 76. Weinreb, C., Wolock, S., and Klein, A.M. (2018). SPRING: a kinetic interface for visualizing
1715 high dimensional single-cell expression data. *Bioinformatics* 34, 1246–1248.
1716 <https://doi.org/10.1093/bioinformatics/btx792>.

1717 77. Kotliar, D., Veres, A., Nagy, M.A., Tabrizi, S., Hodis, E., Melton, D.A., and Sabeti, P.C.
1718 (2019). Identifying gene expression programs of cell-type identity and cellular activity with
1719 single-cell RNA-Seq. *eLife* 8, e43803. <https://doi.org/10.7554/eLife.43803>.

1720 78. Gavish, A., Tyler, M., Greenwald, A.C., Hoefflin, R., Simkin, D., Tschernichovsky, R., Galili
1721 Darnell, N., Somech, E., Barbolin, C., Antman, T., et al. (2023). Hallmarks of transcriptional
1722 intratumour heterogeneity across a thousand tumours. *Nature* 618, 598–606.
1723 <https://doi.org/10.1038/s41586-023-06130-4>.

1724 79. Kazer, S.W., Aicher, T.P., Muema, D.M., Carroll, S.L., Ordovas-Montanes, J., Miao, V.N.,
1725 Tu, A.A., Ziegler, C.G.K., Nyquist, S.K., Wong, E.B., et al. (2020). Integrated single-cell
1726 analysis of multicellular immune dynamics during hyperacute HIV-1 infection. *Nat Med* 26,
1727 511–518. <https://doi.org/10.1038/s41591-020-0799-2>.

1728 80. Kuhn, M. (2008). Building Predictive Models in R Using the caret Package. *Journal of*
1729 *Statistical Software* 28, 1–26. <https://doi.org/10.18637/jss.v028.i05>.

1730 81. Wright, M.N., and Ziegler, A. (2017). ranger: A Fast Implementation of Random Forests for
1731 High Dimensional Data in C++ and R. *Journal of Statistical Software* 77, 1–17.
1732 <https://doi.org/10.18637/jss.v077.i01>.

1733 82. Janitza, S., Celik, E., and Boulesteix, A.-L. (2018). A computationally fast variable
1734 importance test for random forests for high-dimensional data. *Advances in Data Analysis and*
1735 *Classification* 12, 885–915.

1736 83. Meyer, P.E. (2008). Information-Theoretic Variable Selection and Network Inference from
1737 Microarray Data. In.

1738 84. Badia-i-Mompel, P., Vélez Santiago, J., Braunger, J., Geiss, C., Dimitrov, D., Müller-Dott, S.,
1739 Taus, P., Dugourd, A., Holland, C.H., Ramirez Flores, R.O., et al. (2022). decoupleR:
1740 ensemble of computational methods to infer biological activities from omics data.
1741 *Bioinformatics Advances* 2, vbac016. <https://doi.org/10.1093/bioadv/vbac016>.

1742 85. Dobin, A., Davis, C.A., Schlesinger, F., Drenkow, J., Zaleski, C., Jha, S., Batut, P., Chaisson,
1743 M., and Gingeras, T.R. (2013). STAR: ultrafast universal RNA-seq aligner. *Bioinformatics* 29,
1744 15–21. <https://doi.org/10.1093/bioinformatics/bts635>.

1745 86. Danecek, P., Bonfield, J.K., Liddle, J., Marshall, J., Ohan, V., Pollard, M.O., Whitwam, A.,
1746 Keane, T., McCarthy, S.A., Davies, R.M., et al. (2021). Twelve years of SAMtools and
1747 BCFtools. *GigaScience* 10, giab008. <https://doi.org/10.1093/gigascience/giab008>.

1748 87. Li, H., Handsaker, B., Wysoker, A., Fennell, T., Ruan, J., Homer, N., Marth, G., Abecasis,
1749 G., Durbin, R., and 1000 Genome Project Data Processing Subgroup (2009). The Sequence
1750 Alignment/Map format and SAMtools. *Bioinformatics* 25, 2078–2079.
1751 <https://doi.org/10.1093/bioinformatics/btp352>.

1752 88. Patel, A.P., Tirosh, I., Trombetta, J.J., Shalek, A.K., Gillespie, S.M., Wakimoto, H., Cahill,
1753 D.P., Nahed, B.V., Curry, W.T., Martuza, R.L., et al. (2014). Single-cell RNA-seq highlights
1754 intratumoral heterogeneity in primary glioblastoma. *Science* 344, 1396–1401.
1755 <https://doi.org/10.1126/science.1254257>.

1756 89. Tirosh, I., Izar, B., Prakadan, S.M., Wadsworth, M.H., Treacy, D., Trombetta, J.J., Rotem,
1757 A., Rodman, C., Lian, C., Murphy, G., et al. (2016). Dissecting the multicellular ecosystem of
1758 metastatic melanoma by single-cell RNA-seq. *Science* 352, 189–196.
1759 <https://doi.org/10.1126/science.aad0501>.

1760 90. Graham, S.M., Vass, J.K., Holyoake, T.L., and Graham, G.J. (2007). Transcriptional Analysis
1761 of Quiescent and Proliferating CD34+ Human Hemopoietic Cells from Normal and Chronic
1762 Myeloid Leukemia Sources. *Stem Cells* 25, 3111–3120.
1763 <https://doi.org/10.1634/stemcells.2007-0250>.